The University of Oklahoma
Graduate College

Quantum Hall Ferromagnetism in InSb Quantum Wells

A Dissertation

Submitted to the Graduate Faculty

in partial fullfillment of the requirements for the

degree of

Doctor of Philosophy

By

Jean Claude Chokomakoua

Norman, Oklahoma

2005

Downloaded from SHAREOK. Persistent Handle URL: https://hdl.handle.net/11244/877

UMI Number: 3164567

UMI

UMI Microform 3164567

Copyright 2005 by ProQuest Information and Learning Company.
All rights reserved. This microform edition is protected against
unauthorized copying under Title 17, United States Code.

ProQuest Information and Learning Company
300 North Zeeb Road
P.O. Box 1346
Ann Arbor, MI 48106-1346

Quantum Hall Ferromagnetism in InSb Quantum Wells

A Dissertation Approved for the

Department of Physics and Astronomy

by

Sheena Murphy (Chair)

Michael B. Santos

Matthew B. Johnson

Kieran Mullen

Zhisheng Shi

© Copyright Jean Claude Chokomakoua, 2005
All Rights Reserved.

To my parents, my wife, and our children

ACKNOWLEDGEMENTS

I would like to reiterate my sincere gratitude to my thesis supervisor, Dr. Sheena Q. Murphy for her guidance and total support during this research. Her scientific breadth and depth, as well as her unique social skills have been a sure resource for me throughout my stay at the University of Oklahoma.

I am grateful to all my doctoral committee members Dr. M.B. Johnson, Dr. Z. Shi, Dr. K. Mullen, and Dr. M.B. Santos for valuable advices and insights in completing this work. Special thanks to Dr. M.B. Johnson for initiating me to the art of thin films technology, and to Dr. M.B. Santos for providing us with the best InSb quantum wells ever grown. I thank Dr. K. Mullen for being there every time we needed guidance in understanding our experimental data.

I would like to acknowledge Dr. R. Abolfath and Dr. T. Jungwirth for helpful discussions about the theory of quantum Hall ferromagnetism.

Thanks to all the faculty members and staff of the department of Physics and Astronomy for their kindness and support throughout my graduate years. Special thanks to Charles Kelley for help with the maintenance of the equipments and more importantly for all the wisdom I received from him through daily interactions.

I would like to thank S.J. Chung and N. Goel for providing the samples, as well as technical details about the sample structure. I thank Giti Khodaparast for her help with energy level calculations and g-factor determination. My gratitude goes to my laboratory mates Jim Hicks, Ruwan Dedigama, and David Deen for useful discussions and help with various aspects of the day to day life in the low temperature laboratory. I thank J.C. Keay, T. Mishima, Preston Larson, Mike Ball, Kevin Hobbs for their

help in various experiments. Special thanks to REU students and other undergraduate students who worked in the low temperature laboratory during this thesis work. All other graduate students who took classes with me or who interacted with me should find here the expression of my gratitude.

I am infinitely thankful to my parents, Mougoue Ferdinand and Enga Delphine for their care and love. They provided me with the sense of discipline, commitment, and determination that guided me throughout my research. I would like to thank my brothers and my sister Mongoue Filomene for their constant love.

Special thanks to my wife Hortence Maffeu and our daughters M.J. Moshe and G.J. Enga for their endless love and care. The smile on your faces and your understanding even when I had to work late at nights have been a continuous motivation to me.

Contents

ACKNOWLEDGEMENTS **v**

ABSTRACT **xxi**

INTRODUCTION **xxii**

1 Prediction of Ferromagnetic Interactions in Electron Gasses **1**

2 Quantum Hall Effect **4**

2.1 Introduction 4

2.2 The quantum Hall effect explained 6

3 Quantum Hall Ferromagnetism **15**

3.1 Introduction 15

3.2 From ferromagnetism to quantum Hall ferromagnetism 16

3.3 Creation of quantum Hall ferromagnets 19

3.3.1 Use of pressure 19

3.3.2 Use of gate voltage 20

3.3.3 Use of tilted magnetic fields 20

3.4 Characteristic features of quantum Hall ferromagnets 21

4 Material System: InSb and Quantum Well Structures **23**

4.1 Introduction 23

4.2 InSb 23

4.3 InSb quantum well structure 26

5 Quantum Hall Ferromagnetism in InSb Quantum Wells: Experiments and Results 34

5.1 Introduction 34
5.2 Experimental procedure 35
5.3 Illustration of the experimental procedure 36
5.4 Experimental setup 37
5.5 Experimental protocol 39
5.5.1 Bench test 39
5.5.2 Low temperature hunt for best contact configurations 39
5.5.3 Tilter calibration 40
5.5.4 Magnetoresistance measurements 43
5.6 Experimental results 43
5.6.1 Single particle behavior 43
5.6.2 Quantum Hall ferromagnetism 46
5.7 Lessons learned 78
5.7.1 g-factor determination 78
5.7.2 Scattering mechanism 79
5.7.3 Consequence of disorder on quantum Hall ferromagnetism . . 80
5.8 Conclusions 80

6 Gating InSb Quantum Wells 82

6.1 Introduction 82
6.2 Anodization 84
6.2.1 Introduction 84
6.2.2 Experimental setup and procedure 84
6.2.3 Results 85
6.2.4 Chemical analysis of anodic oxide by XPS 91

6.2.5 Anodic oxide growth mechanism 101
6.3 Sputtering deposition of insulators 102
6.3.1 Introduction 102
6.3.2 System used 103
6.3.3 Details of deposition procedure for SiO_2 and SiN_xO_y 105
6.4 Metal evaporation 114
6.4.1 Introduction 114
6.4.2 System used 116
6.4.3 Details of the evaporation 116
6.5 Full gating procedure and test structures 118
6.6 Optimization and CV results 121
6.6.1 Effect of the pH of the electrolyte 121
6.6.2 Anodic voltage effect 122
6.6.3 Annealing effect 123
6.6.4 Fluorine effect 127
6.7 Conclusion 132

7 Conclusions **133**

Bibliography **140**

A Anodization Procedure **141**

B SiN_xO_y Sputtering Deposition Procedure **143**

C Full Processing Sequence For InSb Quantum Wells **145**

D Resistance Peak Simulation **147**

List of Figures

2.1 Magnetoresistance data showing the quantum Hall effects in InSb quantum well (sample M0409a) at 1.5 K. The inset shows the low magnetic field region. The dips in the longitudinal resistance (indicated with thick arrows) are weak signs of FQHE at ν= 2/3 and 1/3. 5

2.2 Schematic of the setup used to measure the magnetoresistance of a 2DES. The electrons confined in the x-y plane are pushed towards one edge of the sample in an applied B-field. The arrows indicate the flow of the probing current. V_H is the Hall voltage and V_L, the longitudinal voltage. 6

2.3 Schematic of energy ladder in the lowest electric subband for a 2DES in strong magnetic field. The dashed line represents the position of the Fermi level at $\nu = 4$(see text). 10

2.4 Density of states of a 2DES in strong magnetic fields.(a) Ideal 2DES has δ function-like DOS at the LL center. (b) Real 2DES has broad energy levels with a band of extended states at the LL center and localized states between extended states. 14

3.1 Various types of QH ferromagnets expected in a narrow single layer 2DES [13]. n represents the LL index, and S the orientation of the real electron spin. 19

4.1 Schematics (not to scale) of typical sample structures used in this study. a) symmetric sample and b) asymmetric sample. 28

4.2 Sample geometries used for this study: (a) square sample; typical side of 5 mm. (b) Hall bar; typical width of 50 μm and voltage probe length L (c) spider mesa; typical inner square size 2x2 mm^2. 29
4.3 Typical behavior of gate voltage effect on carrier density in InSb QW at low temperatures ($\sim$ 4 K). For this sample (Sample S517), the threshold voltage is $\sim$ -0.5 V. 30
4.4 Hall mobility versus density for sample S697 at 4.2 K. The density was tuned using a front gate voltage. The change of Hall mobility with carrier density indicates that interface roughness does not contribute significantly to carrier scattering. 32

5.1 Schematic of the evolution of the LLs in a non interacting system when the $\nu = 2$ QHE state is under tilt. 37
5.2 Schematic of energy level configuration for the first three coincidence indices. 38
5.3 Typical tilter calibration graphs: (a) Hall slope versus tilter displacement. The lines are the best fits to the experimental data (symbols). (b) Angle versus tilter displacement deduced from (a) as described in the text. 42
5.4 Low density sample (S391; $n_s = 0.6\text{x}10^{11}\ cm^{-2}$) under tilted fields at 0.5 K. Note the disappearance and reappearance of all the QHE states at filling factors greater than 1. 44
5.5 High density sample (S702) under tilted fields at 0.03 K. Note the disappearance and reappearance of all the QHE states at filling factors greater than 4, while QHE states at lower fillings seem unaffected. . . 45
5.6 Temperature effect on the $\nu = 2$ QHF in S702. The vertical dotted line indicates the location of filling factor 2. 48

5.7 Temperature effect on the $\nu = 3$ QHF in S702. The resistance peak grows with increasing temperatures. Note however that unlike the $\nu = 2$ case, the resistance peak is large even at the base temperature of 30 mK. 49

5.8 Temperature effect on the $\nu = 2$ QHF in S702 over a broader temperature range. Note the change in line shape of the magnetoresistance with increasing temperatures. 50

5.9 Simulation of the temperature effect on the $\nu = 2$ QHF in S702. The model captures the line shape change of the magnetoresistance with increasing temperatures seen in figure 5.8 51

5.10 Activation energy data for $\nu = 2$ QHF in S702. The lines are linear fit to experimental data. The inset shows the longitudinal resistance as a function of applied fields. The arrows indicate magnetic fields at which data were taken. 52

5.11 Angular evolution of the resistance peak in $\nu = 2$ QHF upon increasing tilt angle. The dotted lines are guides for the eyes. 54

5.12 Angular evolution of the resistance peak in $\nu = 3$ QHF upon increasing tilt angle. The dotted lines are guides for the eyes. 55

5.13 Resistance peaks motion in B_{perp}-B_{total} plane for various samples, mostly from wafers S702 and S372. In the legend, after the symbol, the name of the sample is given, followed by the sample density in units of 10^{11} cm^{-2}, then the QHF state and finally, the temperature at which the data were taken. The lines are fits to the experimental data and represent the so-called coincidence lines. 56

5.14 Hysteresis in the $\nu = 2$ QHF in sample M0315b at ~ 1.0 K. full line is the up sweep trace and dotted line is the down sweep trace. The inset shows the variation of the temperature during field sweeps. 58

5.15 Hysteresis in the $\nu = 2$ QHF in sample S715 at $\sim$ 200 mK. full line is the up sweep trace and dotted line is the down sweep trace. The inset shows the variation of the temperature during field sweeps. 59

5.16 Temperature effect on hysteresis loops in the $\nu = 2$ QHF in sample S702. Full lines represent up sweep traces and dotted lines, down sweep traces. The sets of data are shifted vertically for clarity. 60

5.17 Hysteresis in the $\nu = 3$ QHF in sample S702 at 2 different tilt angles and temperatures. Full lines represent up sweep traces, and dotted lines, down sweep traces. Because the exchange energy is much smaller for the $\nu = 3$ QHF compared to the $\nu = 2$ QHF, 100 mK is in the high temperature regime, hence the smaller hysteresis loops. The 2 sets of data are shifted vertically for clarity. 61

5.18 Hysteresis study in $\nu = 2$ QHF in sample M0322c ($n_s = 1.65\text{x}10^{11}$ cm^{-2}, $\theta = 64.2^o$) at T $\sim$ 0.7K. The upper left panel shows the probe temperature during the run, the upper right panel the magnetoresistance data, and the bottom left panel, the ^{3}He temperature. Note the good probe temperature regulation and the huge hysteresis loop within the QHF. 62

5.19 Repeat of the run with data shown in figure 5.18. No hysteresis found in the magnetoresistance data shown in the upper left panel. The upper right panel shows the probe temperature while the bottom left panel shows the ^{3}He temperature during the run. Note however, the probe temperature was higher and the temperature regulation was not as good. 63

5.20 No hysteresis found in M0322c (n_s = 1.65x10^{11} cm^{-2}, $\theta = 64.0^o$) at T $\sim$ 0.5K. The magnetoresistance data is shown in the upper left panel. The upper right panel shows the probe temperature while the bottom left panel shows the 3He temperature during the run. Note however, the tilt angle difference and the relatively good temperature regulation. 64

5.21 No hysteresis found in M0322c (n_s = 1.65x10^{11} cm^{-2}, $\theta = 64.5^o$) at T $\sim$ 0.7K.The magnetoresistance data is shown in the upper left panel. The upper right panel shows the probe temperature while the bottom left panel shows the ^{3}He temperature during the run. Note the tilt angle difference and the not so good temperature regulation. 65

5.22 Raw data on anisotropy study in the $\nu = 2$ QHF in S702. Without scaling nothing could be said about differences observed in the QHF. 67

5.23 Same data from figure 5.22 after scaling the resistances. The longitudinal resistance was normalized with respect to the resistance value corresponding to filling factor 2.5 (dotted horizontal line). The scaling helped visualize that the system is less resistive when the current runs perpendicular to the in-plane field. 68

5.24 Anisotropy in $\nu = 2$ QHF in S715. The system is less resistive when the current runs perpendicular to the in-plane magnetic field. No scaling was used for these data. 69

5.25 Schematic of possible pseudospin domains orientation in InSb-based QHFs. The domains are stripes perpendicular to the in-plane magnetic field. 70

5.26 Low magnetic fields data for anisotropy studies in sample S702 (n_s=2.1x10^{11} cm^{-2}) at 1.7 K. Data from Ipara B_{ip} configuration was multiplied by $\sim$ 4.4 in an attempt to force the two curves to collapse onto a single curve. Note that the two traces cross at $\sim$ 1.7 T making any attempt to have the two traces collapsing onto a single curve impossible. . . . 71

5.27 Density effect on the persistent resistance minimum in the $\nu = 2$ QHE state. The sample (S702) was held at a constant temperature of 0.3 K and the density changed using gate bias. 73
5.28 Density effect on the first coincidence angle ($\nu = 2$) for all the samples investigated. The dotted vertical line corresponds to the threshold density for the emergence of QHF. In the legend, the number in parentheses corresponds to the QW width; no indication means the well width was 30 nm. 74
5.29 Density effect on the characteristic temperature T_0. The data point in the box is questionable because the resistance change was less than a decade in the activation data. There is undoubtedly a monotonic increase of T_0 with increasing densities. 75
5.30 Angular evolution of the ν=3 QHF in S697 at a fixed density of 2.2x10^{11} cm^{-2} and a temperature of $\sim$1 K. The resistance peak barely moves while the high field valley deepens with increasing tilt. 77
5.31 Temperature evolution of the $\nu = 3$ QHF at a fixed density of 2.5x10^{11} cm^{-2} and tilt angle of 75°. Note the two peaks moving to opposite directions. The arrows are guiding lines for the eyes. 78

6.1 Schematic of the electrochemical cell used for anodization 85
6.2 Dependence of oxide thickness on anodization voltage for bulk InSb anodized for 1 minute in AGW-like electrolyte (2% citric acid: propylene glycol, 1:2 volume mixing ratio). The dotted line represents the linear fit to low voltage data. 89
6.3 Time dependence of oxide thickness and index of refraction of AO on InSb (S849) at a constant voltage of 5.0 V in FBGW electrolyte (BGW + 1.33% vol. 40% NH_4F). Open circles represent the oxide thickness and the stars, the index of refraction on the right vertical axis. 91

6.4 Room temperature XPS spectra for the Sb 3d photolines on samples mentioned in the text. Note the disappearance of the Sb/InSb peak in anodic oxides. The shoulder indicated by the arrow is O 1s peak at ∼ 532.5 eV in Au_2O_3. It is coming from the Au coated sample holder. The spectra are shifted vertically for clarity. 95
6.5 Room temperature XPS spectra for the In 3d photolines on samples mentioned in the text. Note the asymmetry and the shift to lower binding energies of the peaks in the bare sample. The spectra are shifted vertically for clarity. 96
6.6 Room temperature XPS spectra for the F 1s photoline on samples mentioned in the text. Note the peak at ∼ 684.8 eV only in the oxide from the fluorinated electrolyte. The peak signals the incorporation of a detectable amount of fluorine in the AO. The spectra are shifted vertically for clarity. 97
6.7 XPS spectra for the Sb 3d photolines on bare InSb after various high temperature anneals. Note the reduction in intensity of the SbOx photolines with respect to InSb photolines upon increasing anneal temperatures. The shoulder indicated by the arrow is O 1s peak at ∼ 532.5 eV in Au_2O_3. It is coming from the Au coated sample holder. The spectra are shifted vertically for clarity. 99
6.8 XPS spectra for the Sb 3d photolines on AO from fluorinated electrolyte (FAGW) after various high temperature anneal. Note that within the resolution limit of our system, the spectra are not affected by the anneal. The shoulder indicated by the arrow is O 1s peak at ∼ 532.5 eV in Au_2O_3. It is coming from the Au coated sample holder. The spectra are shifted vertically for clarity. 100
6.9 RF power effect on deposition rate of SiO_2 in 10/90 O_2/Ar plasma at 1.0 mtorr. The deposition rate increases with RF power. 108

6.10 RF power effect on substrate self-bias during deposition of SiO_2 in 10/90 O_2/Ar plasma at 1.0 mtorr. The absolute value of the self-bias voltage increases with increasing RF power. 109
6.11 Effect of oxygen on deposition rate of SiN_xO_y. The total pressure was kept constant at 1.0 mTorr and the RF power at 100 W. Note the rise in deposition rate with addition of only 10% oxygen in the processing gas. 111
6.12 Effect of total pressure on deposition rate and self bias for SiN_xO_y in a 10/90 O_2 / Ar plasma at a constant power of 200 W. 113
6.13 Schematic of the deposition geometry during evaporation. 115
6.14 Top view optical microscope image of a typical test sample. The dots are Cr/Au metal gates evaporated through a shadow mask, and the lump on the left, is an indium contact to the semiconductor. 119
6.15 Cross sectional scanning electron microscopy image of a typical test sample showing the interface regions between InSb and AO, and AO and SiN_xO_y. 120
6.16 High frequency (1 MHz) capacitance-voltage graphs for 3 samples from same wafer processed under similar conditions (5V anodization for 1 minutes, and $\sim$ 120 nm SiN_xO_y) except their electrolytes (AGW) have different pH values. Data taken at 77 K. 122
6.17 High frequency (100 kHz) CV data of samples from same wafer (S692) processed under similar conditions except for an additional annealing step inserted at different stage during processing. The samples were annealed in forming gas at 250°C for 5 minutes. The oxynitride layer ($\sim$800 $\mathring{A}$) was deposited at once on all samples in 10/90 O_2/Ar plasma at a total pressure of 3.0 mtorr and an RF power of 200 W. Data taken at 4.2 K. 125

6.18 Density profile from the down sweep trace of data shown in figure 6.17. The arrow indicates the location of charge accumulation following annealing after anodization. 126
6.19 Time evolution of anodic current in various electrolytes. For better comparison, the current was normalized to the initial current so to remove any sample specific effect on the current. Note the faster decay of the current when 1.33% fluorine (from 40% NH_4F) is added to the electrolyte. The samples were anodized at 5 V for 5 seconds. 128
6.20 High frequency (1 MHz) CV data showing the improvement of the gate insulator by addition of a few percent (1.33% vol) of NH_4F in the electrolyte. The samples are from the same wafer (S693) and were processed under same conditions (5V anodization for 1 minute with a subsequent deposition of about 80 nm of SiN_xO_y). Data taken at 77 K. 129
6.21 High frequency (1 MHz) capacitance-voltage graphs for 3 samples from same wafer processed under same conditions (5V anodization for 1 minutes, and about 85 nm of SiN_xO_y) except their electrolytes are different. The fluorinated electrolytes contained 0.33% vol. NH_4F. Data taken at 77 K. 130
6.22 High frequency (1 MHz) capacitance-voltage data showing the effect of fluoride addition on the quality of the gate insulator. The samples are from same wafer (S855) and were processed under similar conditions (5V anodization for 1 minutes and about 80 nm of SiN_xOy). The inset shows the evolution of the hysteresis loop as a function of volume percentage of NH_4F in the electrolyte. Data taken at 77 K. 131

List of Tables

3.1 Models of standard ferromagnets in two dimensions. 16

4.1 Room temperature data comparing relevant parameters of InSb to other III-V semiconductors. [23] [a]Reference [24]. 26

4.2 Relevant parameters of all the samples investigated. The mobilities values are data from the as-grown samples.* The uppermost Si-delta layer was not introduced in these samples.** GaSb buffer and GaSb/AlSb SLS used instead.n_0=10^{11} cm^{-2} 33

5.1 First coincidence (r = 1) angle for most common semiconductors assuming non-interacting electrons. m^* and g^* in the table are the 4 K values. 36

6.1 Useful data for samples used in the XPS characterization. The samples were from wafer S849 with typical size of 5x5 mm^2. Oxide thickness and index of refraction were measured with L111 Gaetner Ellipsometer using a He-Ne laser. 93

6.2 Summary of the binding energies and modified Auger parameters of In and Sb in various compounds. Our data are in italics. AP_{mod} values for InSb are with respect to In $3d_{5/2}$. [a] C.D. Wagner and A. Joshi, J. Elect. Spect. Rel. Phen.,47, 283 (1988). [b] D. Briggs and M.P.Seah, Practical Surface Analysis by Auger and X-ray Photoelectron Spectroscopy, John Wiley & Sons (1983). 98

6.3 Input parameters used to monitor film thickness during sputtering deposition of gate insulators.* Default value for Si_3N_4. We could not find the value of Z-ratio for Si_3N_4 in the literature. 105

6.4 Effect of oxygen content on deposition conditions for SiN_xO_y in an O_2 / Ar plasma at a constant total pressure of 1.0 mtorr and RF power of 100 W. 110

6.5 Effect of total pressure (P_T) on deposition conditions and film quality for SiN_xO_y in a 10/90 O_2 / Ar plasma at a constant power of 200 W. ** indicates that the pressure was very difficult to control and * means pressure needed to be adjusted occasionally.The yield when known, is given in the comments. 112

6.6 Summary of anodization voltage effect on gate insulator performance. All the samples were processed under similar conditions (same electrolyte (AGW); same anodization time (1 minute), and same oxynitride thickness ($\sim$1150 $\mathring{A}$). 123

6.7 Summary of the effect of addition of few volume percent of NH_4F in electrolyte on the overall quality of the gate insulator. The hysteresis loops are measured around flat band voltage. 132

ABSTRACT

Antimony-based III-V semiconductors are getting increasing attention for device applications and fundamental research thanks to advances made in their growth and understanding of their properties. InSb with its extremely small effective mass ($0.015m_e$), large Lande g-factor (-51), and strong spin-orbit effects is poised to be a top contender amongst materials of choice for the exciting field of spintronics. To fully harvest the potentials of this material, the nature of dominant interactions and their dependence on various parameters should be understood, and the processing technology of InSb brought to maturity. We made steady steps towards meeting these goals by investigating level crossings in InSb-based quantum wells under tilted magnetic fields, and developing a reliable gating procedure for these heterostructures.

Experimental observation of quantum Hall ferromagnetic states are reported and the influence of applied magnetic fields, sample tilt angle, temperature, carrier density as well as other experimental conditions on these states are presented.

INTRODUCTION

InSb combines properties that make it attractive for many fundamental and technological applications: its high electron mobility at room temperature can be used to fabricate high speed devices; its large Lande g-factor used to make low field spin related devices; its extremely small band gap to fabricate infra-red (IR) devices; its large spin-orbit effect exploited in the emerging field of spintronics or more fundamental physics as the intrinsic spin-Hall effect. But the potentials of this material have not been fully tapped into, due to formidable challenges in growing high quality epitaxial layers and a processing technology that is still in a "work-in-progress" status.

Recent progress in growth of high quality InSb-based two-dimensional electronic systems (2DESs) by the research group led by Prof. Michael Santos at the University of Oklahoma has facilitated a better understanding of the electronic and optical properties of this interesting material and allowed the exploration of novel devices which exploit the unique properties of InSb. The work presented in this thesis is a contribution to the goal of better understanding the properties of InSb and developing its processing technology. Specifically, we studied the nature of interactions in InSb quantum wells by looking into what happens when a filled spin-split Landau level (LL) is forced into degeneracy with an empty LL with opposite spin, and developed a gate insulator deposition scheme for InSb that is compatible with semiconductor device manufacturing. Our study led to the first observation of quantum Hall ferromagnetism in InSb quantum wells and the development of a reliable gating procedure to tune carrier density over a wide density range in these nanostructures.

This thesis is organized as follows:

- **Chapter 1: Prediction of Ferromagnetic Interactions in Electron Gasses**

  The theoretical basis for ferromagnetic interactions in a sea of electrons is presented by reviewing the Hartree-Fock calculations that led Bloch to predict the possibility of ferromagnetism in electron gasses.

- **Chapter 2: Quantum Hall Effect**

  Starting from the classical Hall effect, we give a concise description of the integer quantum Hall effect, and point out some limits of the current understanding of this phenomenon.

- **Chapter 3: Quantum Hall Ferromagnetism**

  Quantum Hall ferromagnetism is at the core of this thesis, and in this chapter, we provide the necessary background that will help understand this exotic phenomenon.

- **Chapter 4: Material System: InSb and our Quantum Well Structures**

  Though the quantum Hall effect and quantum Hall ferromagnetism are universal, the nature of the material determines the energy and/or temperature scales at which these phenomena occur as well as details of the interactions involved. This chapter is devoted to reviewing the properties of InSb and providing a thorough description of the quantum well structures used to create our two-dimensional electronic systems.

- **Chapter 5: Quantum Hall Ferromagnetism in InSb: Experiments and Results**

  In this chapter we provide details of our experimental investigation. The results are presented and discussed in the light of theory of quantum Hall ferromagnetism. In addition, the summary of what we have learned and what requires further investigation is given.

- **Chapter 6: Gating InSb Quantum Wells**

  A full detail of the gating procedure (process and characterization) that we developed for InSb heterostructures is presented. The procedure could find applications in other hard-to-gate semiconductors.

- **Chapter 7: Conclusions**

Chapter 1

Prediction of Ferromagnetic Interactions in Electron Gasses

As early as 1929, Bloch pointed out that, within the Hartree-Fock (HF) approximation, ferromagnetism naturally emerges in a gas of electrons interacting only through their mutual Coulomb interactions. In fact, for a system of N free electrons where $N_\uparrow$ electrons with wave number $k_\uparrow$ have their spin pointing up and $N_\downarrow$ with wave number $k_\downarrow$ with spin pointing down, the total energy and the total number of electrons per unit volume are given by [1]:

$$E = E_\uparrow + E_\downarrow \tag{1.1}$$

$$\frac{N}{V} = \frac{N_\uparrow}{V} + \frac{N_\downarrow}{V} = \frac{{k_\uparrow}^3}{6\pi^2} + \frac{{k_\downarrow}^3}{6\pi^2} = \frac{{k_F}^3}{3\pi^2} \tag{1.2}$$

with

$$E_{\uparrow(\downarrow)} = N_{\uparrow(\downarrow)}[\frac{3}{5}(k_{\uparrow(\downarrow)}a_0)^2 - \frac{3}{2\pi}(k_{\uparrow(\downarrow)}a_0)]R_y \tag{1.3}$$

And

$$R_y = \frac{e^2}{2a_0} \tag{1.4}$$

Where a_0 is the Bohr radius, and k_F the Fermi wavenumber.

In the expression of the energy (equation 1.3), the first term represents the kinetic energy, and the second term the exchange interaction, between electrons of the same

spin. The net magnetization density is given by:

$$M = -g\mu_B \frac{(N_\uparrow - N_\downarrow)}{V} \tag{1.5}$$

For a paramagnetic ground state; $N_\uparrow = N_\downarrow = \frac{N}{2}$, and $k_\uparrow = k_\downarrow = k_F$ so that:

$$E_{Para} = \frac{N}{2}[\frac{3}{5}[(k_\uparrow a_0)^2 + (k_\downarrow a_0)^2] - \frac{3}{2\pi}[(k_\uparrow a_0) + (k_\downarrow a_0)]]R_y = N[\frac{3}{5}(k_F a_0)^2 - \frac{3}{2\pi}(k_F a_0)]R_y \tag{1.6}$$

For a fully polarized ground state say: $N_\uparrow$ = N, $N_\downarrow$= 0, and $k_\uparrow = 2^{\frac{1}{3}} k_F$ (using equation 1.2), $k_\downarrow$= 0 so that:

$$E_{ferro} = N[\frac{3}{5}2^{\frac{2}{3}}(k_F a_0)^2 - \frac{3}{2\pi}2^{\frac{1}{3}}(k_F a_0)]R_y \tag{1.7}$$

Comparing the two energies:

$$E_{ferro} - E_{para} = N[\frac{3}{5}(2^{\frac{2}{3}} - 1)(k_F a_0)^2 - \frac{3}{2\pi}(2^{\frac{1}{3}} - 1)(k_F a_0)]R_y \tag{1.8}$$

From the equation above (equation 1.8) one can see that the fully magnetized state is lower in energy when the exchange interaction dominates the kinetic energy. This happens at smaller densities *i.e.*,at:

$$k_F a_0 < \frac{5(2^{\frac{1}{3}} - 1)}{2\pi(2^{\frac{2}{3}} - 1)} \simeq 0.35 \tag{1.9}$$

A more realistic HF approximation that includes screening of the exchange interaction drastically alters the results above and predicts ferromagnetism at high densities instead and a non-magnetic state at low densities for systems with a very short range exchange interaction. Unfortunately, any further attempt to improve HF theory keeps altering its predictions and no consensus has been reached on the magnetic nature of the free electron gas. The merit of the HF calculation though, is to hint to the possibility of magnetic order in electronic systems based solely on the competition between the kinetic energy and the Coulombic exchange interaction. Already, there is growing experimental evidence [2, 3] in support of density functional calculations [4, 5, 6] predicting ferromagnetism in non-magnetic materials due to the presence of low concentration of point defects, namely cation vacancies.

One promising medium to explore magnetic ordering in an electron gas with a controllable kinetic energy and exchange interaction is a two dimensional electron system (2DES) subjected to a strong magnetic field *i.e.*, in the quantum Hall regime. The next section introduces the Quantum Hall effect with an emphasis on its salient features.

Chapter 2

Quantum Hall Effect

2.1 Introduction

In 1980, Klaus von Klitzing [7] discovered that two-dimensional electronic systems (2DES) in a strong magnetic field exhibited a step-wise dependence of the Hall resistance rather than the classical linear relationship ($R_H = \frac{B}{n_s e}$), and that; each Hall plateau was associated with a minimum in the longitudinal resistance. Longitudinal and Hall resistances are respectively the resistances of the sample along and transverse to the direction of the probing current. More surprisingly, the value of the resistance at the Hall plateau was quantized as $R_H = \frac{h}{\nu e^2}$, where ν is an integer; h is the Planck constant, and e the charge of electron. The resistance quantum defined as $\frac{h}{e^2}$=25.812...$k\Omega$ is now used as the resistance standard. The discovery of the integer quantum Hall effect (IQHE) sparked intense research on the effects of strong magnetic fields on two-dimensional electronic systems (2DES) that led two years later to the discovery of the fractional quantum Hall effect (FQHE) by D.C. Tsui and H.L. Stormer [8] in high quality samples. Like the integer quantum Hall effect (IQHE) discovered by von Klitzing, the FQHE is characterized by the quantization of the Hall resistance ($R_H = \frac{h}{\nu e^2}$, where $\nu = \frac{p}{2mp \pm 1}$, p, m=1, 2, 3) and is accompanied by longitudinal resistance minima.

Figure 2.1 shows the quantum Hall effect in one of our samples.

In the following, we provide, the necessary information that will help one understands the quantum Hall effect.

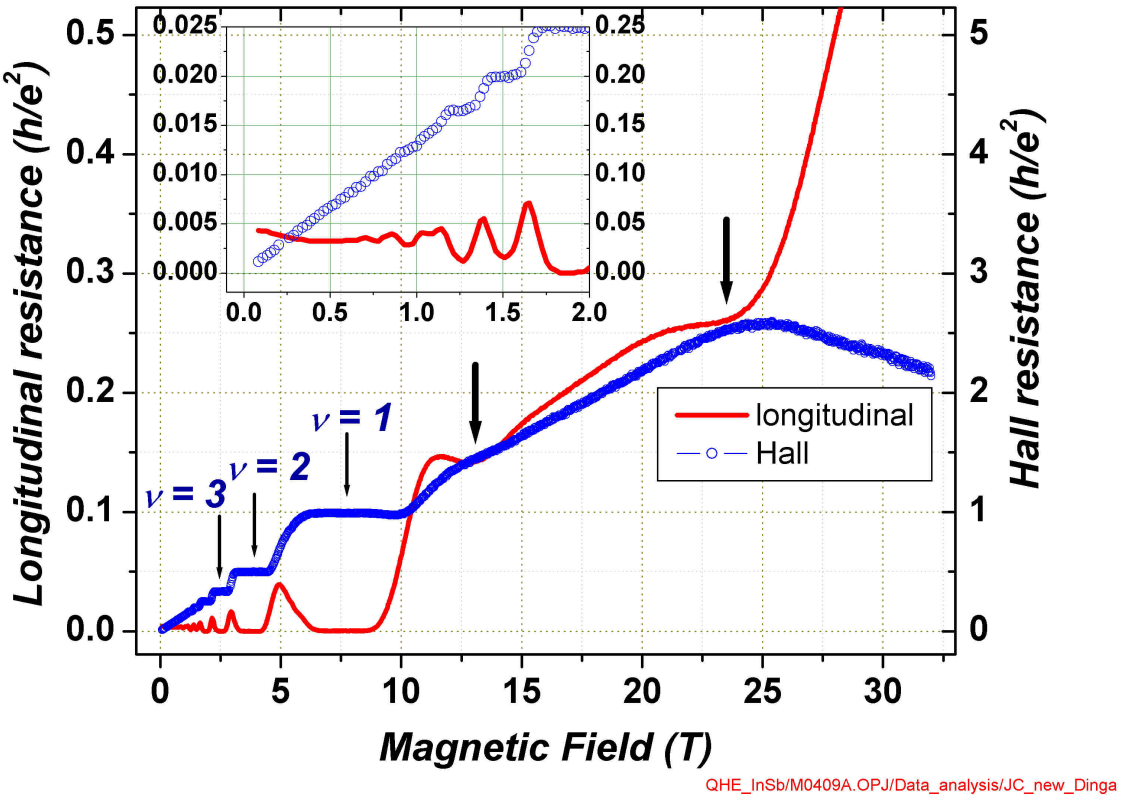

Figure 2.1: Magnetoresistance data showing the quantum Hall effects in InSb quantum well (sample M0409a) at 1.5 K. The inset shows the low magnetic field region. The dips in the longitudinal resistance (indicated with thick arrows) are weak signs of FQHE at ν= 2/3 and 1/3.

2.2 The quantum Hall effect explained

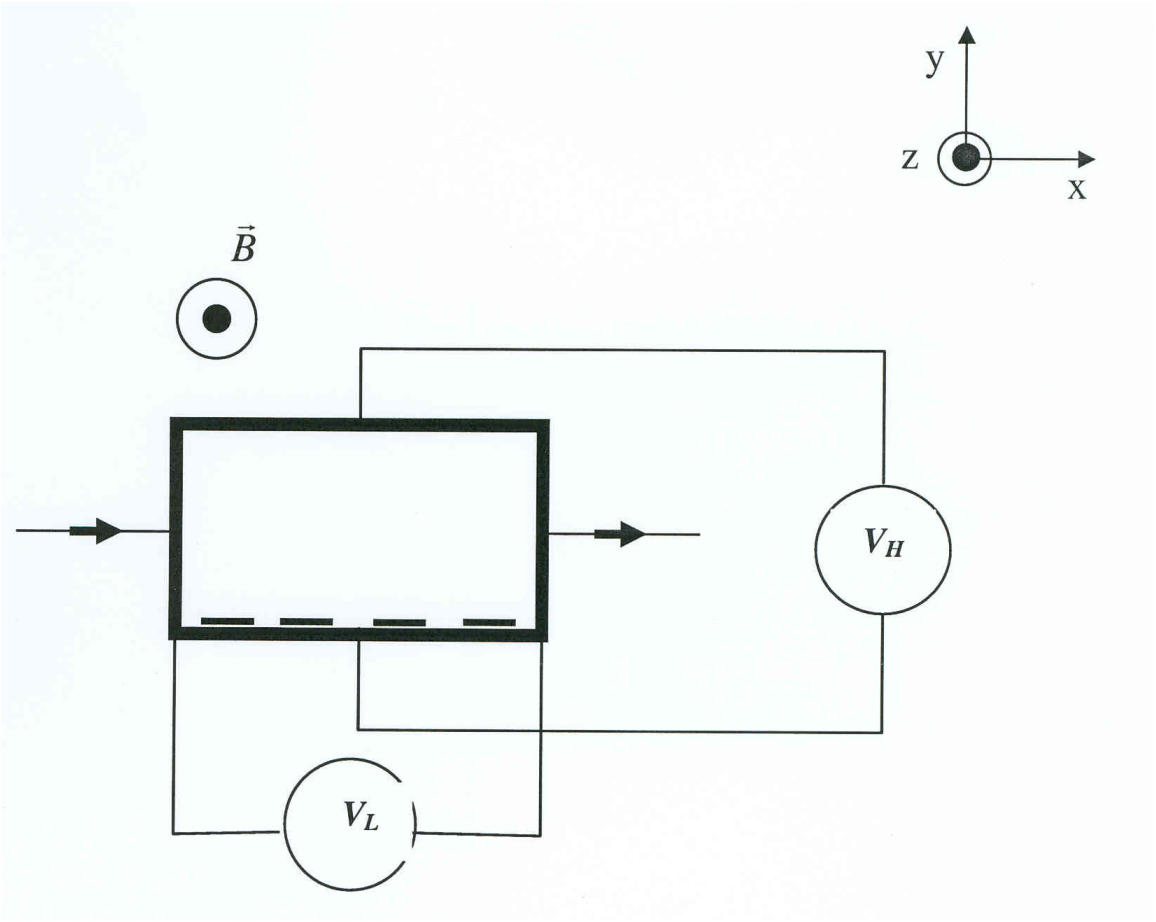

Figure 2.2: Schematic of the setup used to measure the magnetoresistance of a 2DES. The electrons confined in the x-y plane are pushed towards one edge of the sample in an applied B-field. The arrows indicate the flow of the probing current. V_H is the Hall voltage and V_L, the longitudinal voltage.

Consider electrons in a thin film in the x-y plane (see figure 2.2). Without an applied magnetic field,the current flows without a potential drop in the direction perpendicular to the current flow (V_H) whereas there is a potential drop in the longitudinal direction. For B_z=0:

$$R_L = \frac{V_L}{I} \neq 0 \tag{2.1}$$

and

$$R_H = \frac{V_H}{I} = 0 \tag{2.2}$$

When the magnetic field is applied along the z-direction, a non-zero voltage V_H will be generated. V_H is the Hall voltage which when divided by the current I, becomes the Hall resistance R_H. For $B_z \neq 0$:

$$R_L = \frac{V_L}{I} \neq 0 \tag{2.3}$$

and

$$R_H = \frac{V_H}{I} \neq 0 \tag{2.4}$$

The description of the magneto-transport properties of two dimensional electron systems is commonly carried out using the resistivity (ρ) or conductivity tensor (σ). In 2D, resistivity (conductivity), an intrinsic property of the system has the same units as the resistance (conductance), a measure that depends on the material and its geometry. Resistivity and conductivity are related as shown below.

$$\rho_{xx}(or \rho_{yy}) = \frac{\sigma_{xx}(or \sigma_{yy})}{{\sigma_{xx}}^2 + {\sigma_{xy}}^2} \tag{2.5}$$

and

$$\rho_{xy}(or \rho_{yx}) = \frac{\sigma_{xy}(or \sigma_{yx})}{{\sigma_{xx}}^2 + {\sigma_{xy}}^2} \tag{2.6}$$

In these notations, the first index refers to the direction of the current and the second index to the direction of the voltage. The origin of the Hall voltage is found in classical electrodynamics. The magnetic field exerts Lorentz force $\vec{F}$=q$\vec{V}$x$\vec{B}$, ($\vec{V}$ and q are the speed and charge of the carriers respectively) onto the electrons, pushing them towards one side of the film (see figure 2.2). The charge accumulation ultimately results in the potential drop V_H. It is shown that $R_H = \frac{B}{n_s e}$ where n_s is the electron density in the film. At lower densities, the electrons will have to move faster in order to maintain the same current, but faster moving carriers lead to stronger Lorentz forces. The independence of the Hall resistance from all intrinsic (except the carrier

density) and extrinsic parameters of the host material has made Hall measurement, a standard technique for the determination of the density of free electrons in materials.

A repeat of the experiment above in strong magnetic fields (B > 1 T) at low temperature, and in clean samples, will lead to step wise dependence of the Hall resistance on magnetic field, rather than the linear relationship given above. The explanation of this unexpected behavior, called quantum Hall effect (QHE) is obviously beyond classical electrodynamics. Though a full quantum mechanical treatment is necessary to fully understand the quantum Hall effect, simple semi-classical models capture most of the details of the integer QHE. The semi-classical model aim is to relate the band structure of the system to its transport properties. In the model, the externally applied fields are treated classically but the periodic field of the ions forming the background in which carriers move, is treated quantum mechanically in an effective mass approximation i.e., the interaction between the electrons and the crystal lattice is assumed to have a net effect of making the electrons move as if they were in a free space with an effective mass m^*. The model also assumes that the fields cause no interband transitions. That is to say the energy bands have fixed degeneracy. It is shown that in the semi-classical model, conduction is due only to those electrons that are found in partially filled bands. In (or near) equilibrium, filled bands are those with energy below the Fermi level (E_F) while empty bands are those above E_F. For the system described above, the Schrodinger equation describing the motion of the electron is: Hψ=Eψ,H is the single electron Hamiltonian,ψ the electron wavefunction, and E the energy. H is given by:

$$H = \frac{1}{2m^*}(\vec{p} - e\vec{A})^2 + \frac{1}{2}g^*\mu_B\vec{\sigma}.\vec{B} + V(z) \tag{2.7}$$

Where $\vec{A}$ is the vector potential related to the applied magnetic field by:

$$\vec{B} = \vec{\nabla}x\vec{A} \tag{2.8}$$

g^* is the Lande g-factor, μ_B is the electron Bohr magnetron, V(z) is the confining potential along the growth direction (z-direction), and $\vec{\boldsymbol{\sigma}}$ is the Pauli spin matrix. In

the Landau gauge, we take the vector potential as $\vec{A}$(0,xB,0). After some algebraic manipulations, we arrive at the following expression for the Hamiltonian:

$$H = [\frac{1}{2m^*}p_x^2 + \frac{1}{2}m^*\omega_c^2(x - x_0)^2] + \frac{1}{2}g^*\mu_B B\sigma_z + [\frac{1}{2m^*}p_z^2 + V(z)] \quad (2.9)$$

where ω_c=$\frac{eB}{m^*}$ is the cyclotron frequency, and x_0=$\frac{\hbar k_y}{eB}$. The first term is the Hamiltonian of a 1D harmonic oscillator centered at x_0, the second term represents the interaction of the spins of the electrons with the applied magnetic field, and the last term, is the Hamiltonian of a simple 1D potential well. The energy band for such a system is the sum of eigen-energies of the contributing terms:

$$E = (n + \frac{1}{2})\hbar\omega_c \pm \frac{1}{2}g^*\mu_B B + E_\xi \quad (2.10)$$

Where n=0,1,2, is the Landau level index, ξ the electric subband index. Schematically (see figure 2.3), the energy band is an energy ladder of Landau levels (LLs) with successive LLs separated by $\hbar\omega_c$ (the cyclotron gap), and spin split levels with the same LL index separated by $g^*\mu_B B$ (the Zeeman gap).

Electrons now reside on discrete energy levels, which can accommodate N_L states per spin-split level. N_L represents the degeneracy of the level and is given by:

$$N_L = \frac{eB}{h} \quad (2.11)$$

The radius r of cyclotron motion of an electron on the level with LL index n is:

$$r = \sqrt{2n + 1}l_B \quad (2.12)$$

Where l_B, the magnetic length is defined as:

$$l_B = \sqrt{\frac{\hbar}{eB}} \quad (2.13)$$

The existence of the gaps between energy levels is crucial to the occurrence of the quantum Hall effect. For a sample with fixed 2D electron density n_s, at low temperature, all the electrons fall into the lowest available state. In very weak magnetic

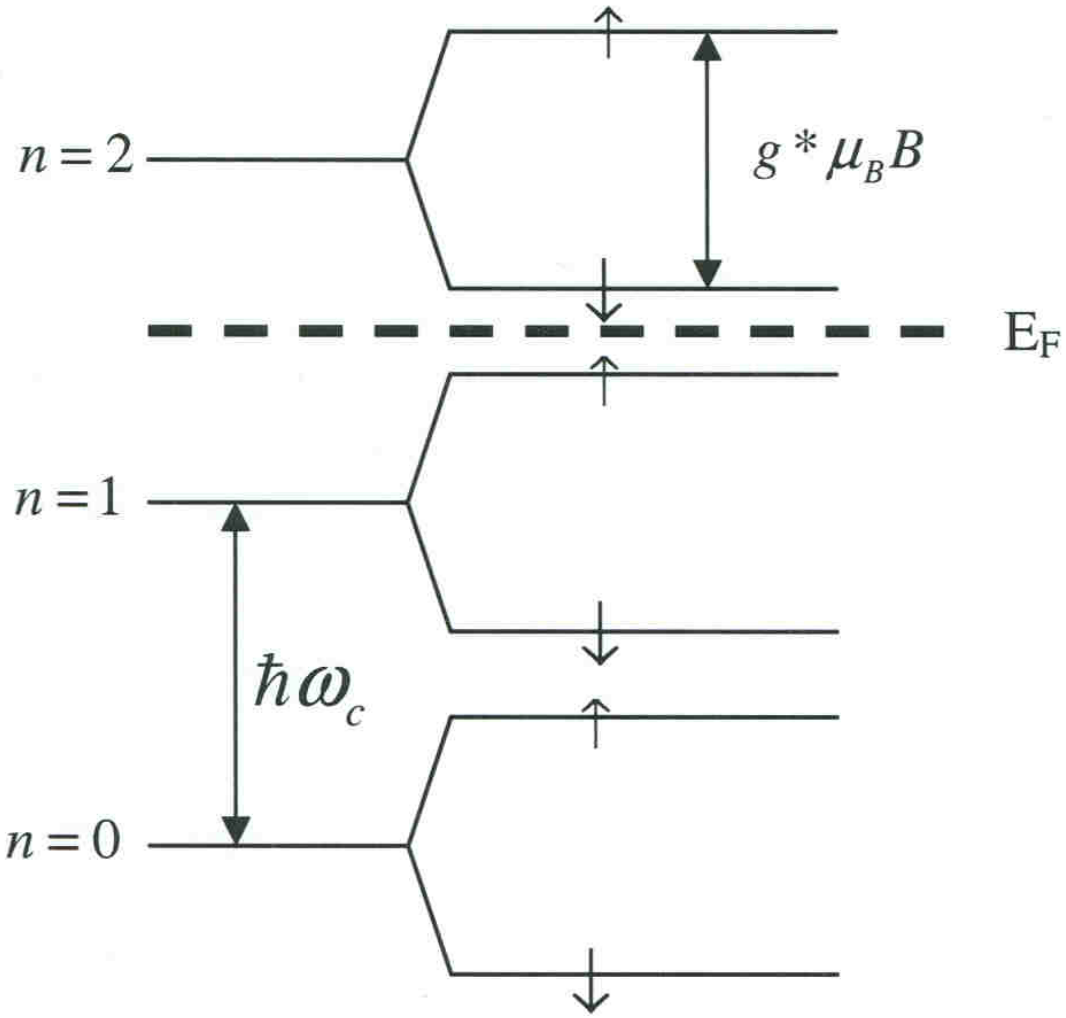

Figure 2.3: Schematic of energy ladder in the lowest electric subband for a 2DES in strong magnetic field. The dashed line represents the position of the Fermi level at $\boldsymbol{\nu = 4}$(see text).

fields, the energy gaps are very small and the energy spectrum of the electron gas is nearly a continuum, just as in a bulk material. As a result, the classical Hall effect is observed. As the magnetic field increases, so do the gaps and the number of available states per energy level. Let $\boldsymbol{B_{n1}}$ be the field at which the energy gaps start to be resolved and $\boldsymbol{n_1}$ be the number of energy levels that are fully occupied at B=$\boldsymbol{B_{n1}}$. We have:

$$\boldsymbol{n_s = n_1 N_L} \tag{2.14}$$

so that we can write:

$$\boldsymbol{n_1 = \frac{n_s h}{e B_{n1}}} \tag{2.15}$$

In general, the filling factor *i.e.*, the number of occupied energy levels at a given magnetic field B is:

$$\boldsymbol{\nu = \frac{n_s h}{eB}} \tag{2.16}$$

Any further increase in the magnetic field creates empty states in all the energy levels, forcing electrons in upper levels to jump into newly available states in lower levels. At the magnetic field $\boldsymbol{B_{n1-1}}$ given by:

$$\boldsymbol{B_{n1-1} = \frac{n_1 B_{n1}}{n_1 - 1}} \tag{2.17}$$

one spin split LL is depleted, leaving the system with only $\boldsymbol{\nu_2}$=$\boldsymbol{n_1 - 1}$ filled Landau levels. With further increase of the magnetic field, electrons have to jump to still lower levels, and at:

$$\boldsymbol{B_{n1-2} = \frac{n_1 B_{n1}}{n_1 - 2}} \tag{2.18}$$

only $\boldsymbol{n_1 - 2}$ Landau levels are filled. This process continues with additional increase of the magnetic field yielding a sequence of fields

$$\boldsymbol{B_i = \frac{n_1 B_{n1}}{i}, i = n_1, n_1 - 1, n_1 - 2, ...} \tag{2.19}$$

at which electrons fill up exactly i number of LLs. At these fields, the Hall resistance assumes the value

$$\boldsymbol{R_H = \frac{B_i}{n_s e} = \frac{n_1 B_{n1}}{i n_s e} = \frac{1}{i}(\frac{h}{e^2}) i = n_1, n_1 - 1, n_1 - 2, ...} \tag{2.20}$$

While this shows the quantization in $\frac{h}{e^2}$, it does not account for the true fingerprint of the QHE, *i.e.*, wide plateaus in R_H and broad resistance minima in R_L around B_i as shown in figure 2.1. The plateau formation and broad longitudinal resistance minima are understood within the semi-classical model as follows. The energy levels are not perfectly thin as sketched in figure 2.3. They are broadened by residual defects and / or impurities inherent in any real 2DES. The density of states (DOS) for an ideal and a real 2DES are shown in figure 2.4. The energy states at the LL center are delocalized or extended over the entire 2DES while those at the energy tails are localized in small regions in the sample. Electrons in extended states can participate in conduction through out the sample while those in localized states cannot, being bound to either impurities or defects in the crystal. Upon increasing the magnetic field, the energy levels move past the Fermi level as various states (localized and extended) are being emptied or filled. As long as electrons filling or emptying a Landau level, fill or empty only the localized states while keeping the extended states at the Landau level center full to capacity, the samples Hall resistance R_H and longitudinal resistance R_L remain constant. Because conduction is dictated by carriers in states few kT around the Fermi level, the measured resistance correlates with the location of the Fermi level. When the Fermi level is in a gap (*i.e.*, an integer number of levels are completely full) there are no states capable of scattering conduction electrons. The longitudinal resistance is infinitesimally small and the Hall resistance is the contribution of all the filled levels with each spin split level contributing equally to the total resistance. When the Fermi level overlaps an extended state, conduction electrons suffer more scattering as occupied and unoccupied states are very close in energy. As a result, the longitudinal and the Hall resistances abruptly increase. As the field is increased, the longitudinal resistance reaches a peak value when the Fermi level is right in the middle of the extended state and then decreases as the Fermi level sweeps through the high field end of the extended state. The Hall resistance on the other hand keeps increasing and reaches the next resistance plateau when the band of extended states

is emptied. From this point, the Hall resistance stays quantized and the longitudinal resistance stays vanishingly small as the Fermi level penetrates into another energy gap. This stepwise trend continues till all the electrons are forced into the lowest spin split level. Further increase in the magnetic field past this point leads to the extreme quantum limit where the fractional quantum Hall effect was discovered. Just like the IQHE, FQHE is characterized by the quantization of the Hall resistance and associated longitudinal resistance minima but at non-integral filling factors. The observation of these states in the magnetic field range where all magnetic field induced gaps are exhausted, suggested that the FQHE is of many-body origin. In fact, in the extreme quantum limit, the electrons, strongly squeezed in the lowest LL, minimize their mutual Coulomb repulsion by rearranging themselves in the most energetically favorable manner; they form a strongly correlated system held together by electron-electron interactions [10]. A description of the physics of the FQHE is not relevant to the core of this thesis and has not been included here, however interested readers are referred to [10] for an excellent introduction. The quantum Hall effect seems well understood yet, 2DESs in strong magnetic fields continue to be full of surprises. The surprises arise from a lack of proper understanding of the microscopic nature of the states (extended and localized) defining the QHE. Among the surprises are even denominator states; increasing experimental evidence casting doubts on the validity of the single particle description of the IQHE and which suggest that the non-interacting picture is valid only in the limit of strong disorder [9]; and the emergence of the so called quantum Hall ferromagnetism (QHF) both in the integer and the fractional quantum Hall regime.

In the following chapter, we will give the background necessary to comprehend QHF in single quantum wells, deep in the integer quantum Hall regime ($\boldsymbol{\nu} > 1$) that constitutes the essence of this thesis.

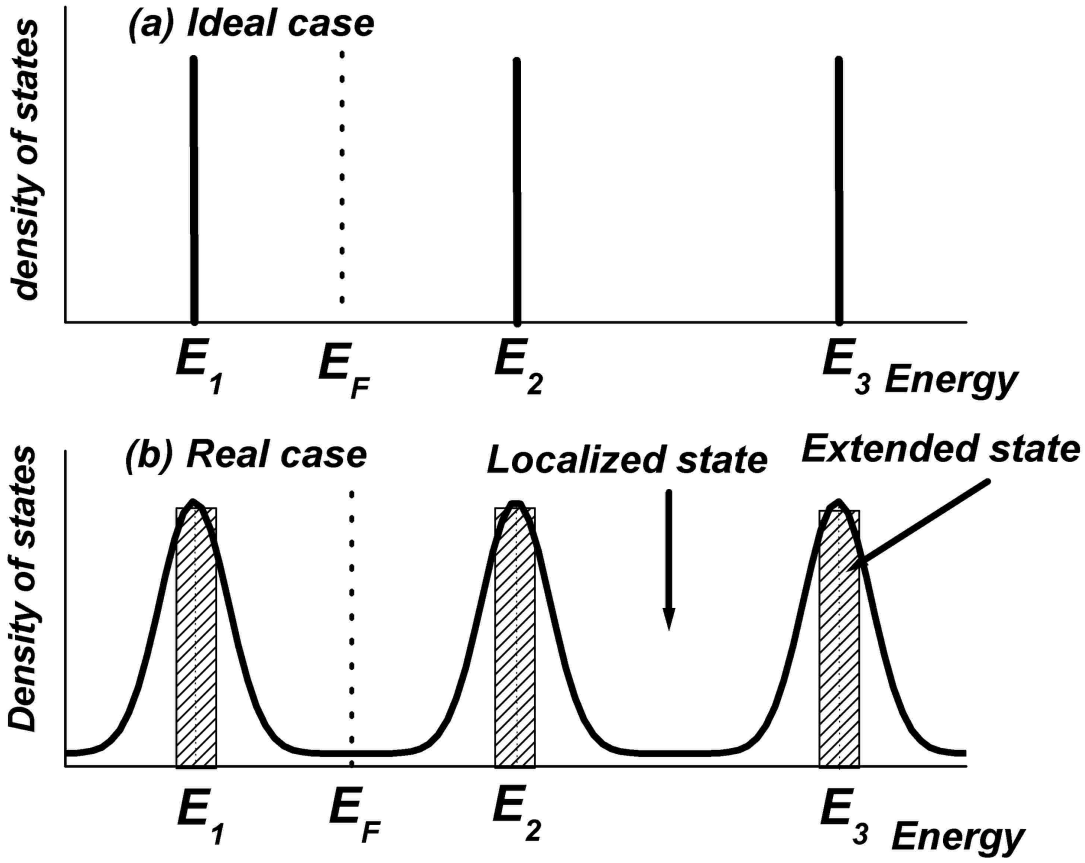

Figure 2.4: Density of states of a 2DES in strong magnetic fields.(a) Ideal 2DES has $\boldsymbol{\delta}$ function-like DOS at the LL center. (b) Real 2DES has broad energy levels with a band of extended states at the LL center and localized states between extended states.

Chapter 3

Quantum Hall Ferromagnetism

3.1 Introduction

The quantum Hall effect (QHE) continues to fascinate solid state physicists due to unanticipated phenomena that continuously emerge as a result of the complex interplay between orbital quantization, disorder, and electron-electron interactions in 2DESs in high magnetic fields at low temperatures [10]. Unusual transport behavior uncovered both in the integer and fractional QH regimes [11] under conditions where spin phase transitions would occur are now being discussed in terms of QH ferromagnetism [12]. In this chapter, we provide answers to the following questions: what is quantum Hall ferromagnetism? How is a quantum Hall ferromagnet formed? And what are its main features? Without loss of generality, we will concentrate mostly on quantum Hall ferromagnets in single layer systems and in the integer QH regime. What is said here can be easily extended to bilayers, and to fractional QH states.

3.2 From ferromagnetism to quantum Hall ferromagnetism

Ferromagnetism as observed in transition metals (Fe, Ni, Co) or rare earths (Gd, Sm, etc) occurs as a result of a net spin polarization in the system i.e., the integrated density of one spin state is not equal to that of the opposite spin state. Standard ferromagnets have a spontaneous symmetry breaking ground state, undergo a ferromagnetic to paramagnetic state phase transition as the temperature is increased, and may or may not have a memory effect due to the competition between anisotropic energy and exchange energy. In 2D, several models are used to describe ferromagnets, based on the nature of the coupling between the magnetic moments (spin). The model Hamiltonian for these ferromagnets in general is given by:

$$\boldsymbol{H} = -\sum_{\boldsymbol{i}} \boldsymbol{g\mu_B \vec{S}_i \cdot \vec{B}} - \sum_{\boldsymbol{i,j(i\neq j)}} \boldsymbol{J_{ij} \vec{S}_i \cdot \vec{S}_j} \tag{3.1}$$

Where $\vec{\boldsymbol{S}}$ is the spin operator, $\vec{\boldsymbol{B}}$ is the applied magnetic field, and $\boldsymbol{J_{ij}}$ is the exchange interaction coefficient($\boldsymbol{J_{ij}} > 0$). The first term in equation 3.1 represents the interaction of the magnetic moments with the external magnetic field while the second term, represents the interactions between the magnetic moments. Table 3.1 summarizes the various models of ferromagnets in two dimensions.

Models	Heisenberg(Isotropic)	X-Y	Ising
Description	$\boldsymbol{J_{ij}}$=constant	$\boldsymbol{J_{xx}}$ and $\boldsymbol{J_{yy}} \neq 0$;$\boldsymbol{J_{zz}}$=0	$\boldsymbol{J_{zz}} \neq 0$; $\boldsymbol{J_{xx}}$=$\boldsymbol{J_{yy}}$=0
	No preferred orientation	Planar orientation	Uniaxial orientation
	No hysteresis	No hysteresis	Hysteresis

Table 3.1: Models of standard ferromagnets in two dimensions.

Heisenberg or isotropic ferromagnets represent systems in which the total spin can point in any direction with equal probability while X-Y ferromagnets represent those

in which the total spin lies in a plane. X-Y ferromagnets are believed to undergo a finite temperature Kosterlitz-Thoules phase transition. Lastly, Ising ferromagnets are systems in which the total spin can assume only two possible orientations (up or down); they are the richest, displaying memory effects manifested by hysteresis loops.

From the quantization of the energy levels of 2DES into spin split levels, with the subsequent filling of these levels according to the strength of the applied magnetic field, a system in the QH regime can have a non zero net spin polarization or a zero spin polarization, depending on the filling factor and the strength of the Zeeman energy. Non -zero spin polarization occurs at odd filling factors (with full spin polarization at $\boldsymbol{\nu}$=1) because of an unequal number of filled spin up and spin down states, while zero spin polarization occurs at even filling factors due to an equal number of filled spin up and spin down states. Spin polarized states in the QH regime are not necessarily quantum Hall ferromagnetic states, rather they are more like Pauli paramagnetic states where spin polarization is solely due to the application of the magnetic field. The term quantum Hall ferromagnet is reserved for QH states that can mimic the behavior of standard ferromagnets i.e. those with a spontaneously broken symmetry. The use of quantum Hall in the designation of the magnetic nature is to emphasize that these magnetic states occur due to the energy quantization in the QH regime. Both odd and even filling factors are potential QH ferromagnets. They develop into QH ferromagnets whenever there is a competition between the Coulomb exchange energy and the Zeeman energy. The concept of quantum Hall ferromagnetism has been generalized [13] to include any symmetry breaking ground state that forms when two or more energy levels simultaneously approach the Fermi level. By analogy to standard ferromagnets where the state of the system is described by its spin orientation, the state of a QH ferromagnet is described by its pseudo-spin (or isospin). In the case of two levels approaching the Fermi level, one of the energy levels is considered pseudospin up and the other pseudospin down. In single layer systems, the pseudospin quantum number actually subsumes real spin (S=$\pm\frac{\mathbf{1}}{\mathbf{2}}$), subband index

($\boldsymbol{\xi}$), and Landau level index (n) degrees of freedom.

The analogy between quantum Hall ferromagnets and standard ferromagnets was made manifest by T. Jungwirth *et al.* [13] using a Hartree-Fock (HF) calculation as follows.

For the case of two levels approaching the Fermi level simultaneously, defining the two levels as pseudospin up $|\uparrow\rangle$ and pseudospin down $|\downarrow\rangle$, a state with the pseudospin oriented along a general unit vector $\vec{\boldsymbol{m}}(\sin(\boldsymbol{\theta})\cos(\boldsymbol{\phi}),\sin(\boldsymbol{\theta})\sin(\boldsymbol{\phi}),\cos(\boldsymbol{\theta}))$ can be presented as:

$$\mid \vec{\boldsymbol{m}}\rangle = \boldsymbol{cos}(\frac{\boldsymbol{\theta}}{\boldsymbol{2}})\ |\uparrow\rangle + \boldsymbol{e^{i\phi}sin}(\frac{\boldsymbol{\theta}}{\boldsymbol{2}})\ |\downarrow\rangle \tag{3.2}$$

The pseudospin orientation of the ground state is determined by minimizing the HF ground state energy [13]:

$$\boldsymbol{E_{HF}(m)} = \frac{\langle \vec{\boldsymbol{m}} \mid \boldsymbol{H} \mid \vec{\boldsymbol{m}}\rangle}{\boldsymbol{N}} = -\sum_{\boldsymbol{i=x,y,z}} \boldsymbol{b_i m_i} - \sum_{\boldsymbol{i,j=x,y,z}} \boldsymbol{U_{ij} m_i m_j} \tag{3.3}$$

Where N is the total number of particles in the system, $\vec{\boldsymbol{b}}$ is the effective magnetic field acting on pseudospins with magnetic moment $\vec{\boldsymbol{m}}$, and $\boldsymbol{U_{ij}}$ is the interaction coefficient between pseudospin magnetic moments. The effective magnetic field $\boldsymbol{b_i}$ includes external and internal potentials (cyclotron energy, Zeeman coupling, interactions with remote LLs, etc.), and the electron-electron interaction coefficients $\boldsymbol{U_{ij}}$ depend on the nature of the crossing LLs [13]. Note the striking resemblance between equation 3.3 and the Hamiltonian describing standard ferromagnets (equation 3.1).

When two LL are degenerate, the effective magnetic field vanishes (*i.e.* there is no preference for either pseudospin state) and the type of QHF depends on the sign of $\boldsymbol{U_{ij}}$, which in turn depends on the nature of the degenerate LLs. It is shown that when the levels are from the same electric subband, if the two levels have the same LL indices (case of odd filling factors in the limit of vanishing Zeeman energy), $\boldsymbol{U_{ij}} = 0$ for all is and js, i.e., an isotropic (Heisenberg) quantum Hall ferromagnet develops, but if they have different LL indices, Ising-like QH ferromagnets develop as $\boldsymbol{U_{zz}} > 0$ and $\boldsymbol{U_{ij}} = 0$ for i, j = x, y. For levels from different electric subbands, the in-plane

degree of freedom leads to a 2D X-Y QH ferromagnet irrespective of the real spin orientation if the LLs have the same LL index. When the LL indices are different, Ising ferromagnets will occur if the spins of the crossing levels are opposite while X-Y quantum Hall ferromagnets will occur otherwise. Figure 3.1 gives a schematic summary of the various types of QH ferromagnets expected in a narrow single layer 2DES.

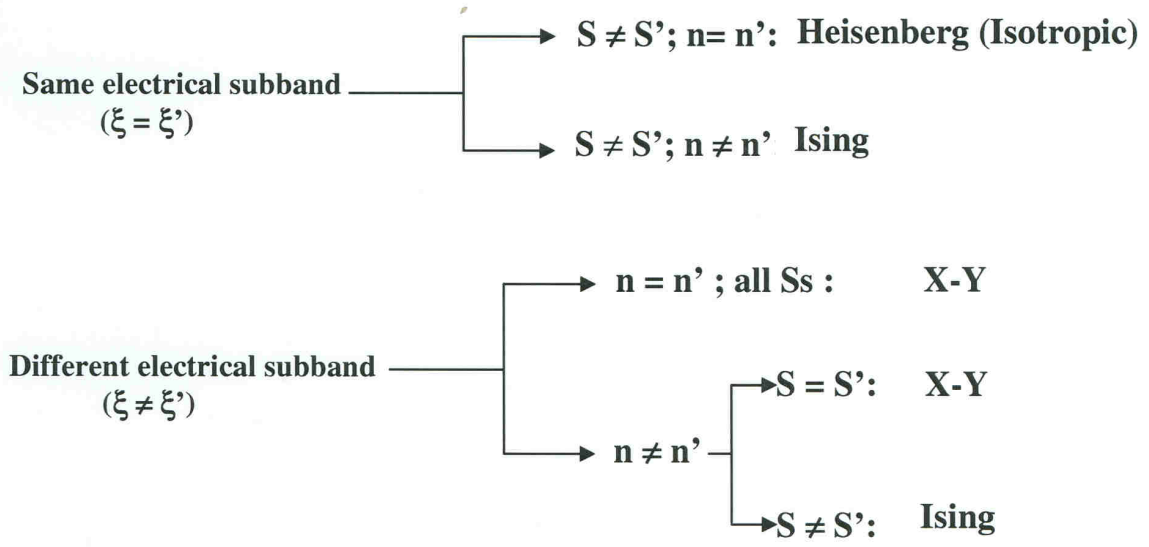

Figure 3.1: Various types of QH ferromagnets expected in a narrow single layer 2DES [13]. n represents the LL index, and S the orientation of the real electron spin.

3.3 Creation of quantum Hall ferromagnets

There are three ways to create QHF states in systems that do not have a vanishingly small Zeeman energy:

3.3.1 Use of pressure

By applying pressure on a 2DES sample held in a pressure cell, one can force different LLs into degeneracy [14]. This occurs because the pressure has a net effect of

reducing the Lande g-factor hence the Zeeman energy. Pressure induced QHFs are expected to be effective for odd filling factors (degeneracy between LLs of electrons) and fractional QH states. With this technique, the usual scenario is for levels from same LL index and opposite real spin orientation will become degenerate, forming Heisenberg ferromagnets.

3.3.2 Use of gate voltage

This approach exploits the dependence of the energy separation between the 2 lowest electric energy subbands ($\boldsymbol{\Delta_{SAS}}$=$\boldsymbol{E_{\xi_1}}$-$\boldsymbol{E_{\xi_2}}$) on the structure of the 2DES and the carrier density. With applied gate bias, the electric subbands can be brought closer to each other thus making possible crossings between LLs from different subbands [15]. SAS decreases with increasing carrier density. Crossing between LLs from different subbands, offers many interesting possibilities such as degeneracy between levels with the same or opposite real spin orientations regardless of their LL indices, or between levels with same or different LL indices regardless of their real spin orientation. To be effective, the carrier density needs to be tuned over a broad range without substantial distortion of the confinement potential. This method can produce both X-Y and Ising like ferromagnets.

3.3.3 Use of tilted magnetic fields

The two energy gaps (cyclotron and Zeeman gaps), key to the occurrence of the QHE, have different dependence on specific component of the applied magnetic field. While the cyclotron gap depends on the perpendicular component of the magnetic field, the Zeeman gap depends on the total field. This allows independent control of the energy gaps and can be effectively used to force different LLs into degeneracy [16]. In tilted field experiments as in this thesis, level crossings within same electric subband occur mostly between LLs of opposite real spins and different LL indices, resulting in mostly Ising like ferromagnets. Assuming the single particle energy (equation 2.9)

applies, level crossing between levels with LL index n, spin up and LL index n' spin down occurs when the two energies are equal:

$$(n' + \frac{1}{2})\hbar\omega_c - \frac{1}{2}g^*\mu_B B + E_\xi = (n + \frac{1}{2})\hbar\omega_c + \frac{1}{2}g^*\mu_B B + E_\xi \tag{3.4}$$

after simplification we get

$$\Delta n cos(\theta) = \frac{1}{2}\frac{m^*}{m_e}g^* \tag{3.5}$$

where we have used

$$\hbar\omega_c = \hbar\frac{eBcos(\theta)}{m^*} \tag{3.6}$$

$$\mu_B = \frac{\hbar e}{2m_e} \tag{3.7}$$

$$\Delta n = n' - n \tag{3.8}$$

and θ is the angle between the applied magnetic field and the sample normal.

Δn is often referred to as the coincidence index, r.

From the coincidence condition above (equation 3.5), level crossing occurs at relatively smaller tilt angles in materials with a larger product m*g*.

3.4 Characteristic features of quantum Hall ferromagnets

The main features of QHF include broken symmetry ground states arising from spontaneous magnetic ordering; the existence of Goldstone modes in the ordered state, and topological objects as low energy excitations [10]. The spontaneous symmetry breaking ground state prevents the energy gap responsible for the QH state from collapsing. In magneto-transport, this is observed by a persistent QH state which otherwise would have disappeared. The Goldstone modes are typically collective motion of quasi-particles with same pseudospin (analogous to spin density waves) around the effective magnetic field while topological objects (e.g., skyrmions, merons), are

geometrical ordering of the spins of quasi-particles with a winding number q, that costs a finite amount of energy to break.

Though quantum Hall ferromagnetism is a very general concept and can be generated in any material system, some materials are more appropriate for experimental studies on this exotic phenomenon than others, based on the access to level crossings under readily available experimental settings. In the following chapter, we provide details on the material system and sample structures used for this work, and point out the key parameters likely to affect our results.

Chapter 4

Material System: InSb and Quantum Well Structures

4.1 Introduction

The high room temperature electron mobility of materials from the III-V family of semiconductors has made them very attractive for device applications and fundamental research aimed at understanding the behavior of carriers under special conditions. Though arsenic-based compound such as GaAs and InAs are by far the most studied binary materials in this family, antimony-based compounds, particularly InSb and GaSb are getting increasing attention thanks to advances made in their growth and understanding of their properties.

In this chapter, we review the major properties of InSb-the material used in this study, and provide a detailed description of the quantum well structures used to create our 2DES.

4.2 InSb

InSb combines properties that make it unique in terms of potential applications but also present formidable challenges in terms of epitaxial growth and structure isolation.

Among binary III-V semiconductors, InSb has the highest intrinsic electron mobility and the largest electron Lande g-factor, making this material suitable for very sensitive magneto-sensors [17] and high speed switching devices [18]. It has the narrowest energy gap, which places it among materials of choice for mid-infrared device applications. In addition, InSb has the smallest electron effective mass, the property that justified the leading role played by this material in the early development of the cyclotron resonance technique [19]. Finally, InSb crystallizes in the zincblende structure (like all the other III-V semiconductors) with large spin-orbit split off energy. As a result, InSb is particularly interesting for studying novel physics phenomena associated with structure inversion asymmetry (SIA) or the Rashba effect and with bulk inversion asymmetry (BIA) or the Dresselhaus effect.

Many properties of InSb however conspire to make heterostructure formation and room temperature device operation difficult with this material. Because of its narrow band gap, large room temperature intrinsic carrier concentration, and the Fermi level pinning at the surface [20], InSb behaves like a metal at room temperature. The high conductivity of at room temperature causes unwanted carrier flow in substrates made of InSb and makes them inappropriate for device applications. Because the lattice constant of InSb is large, this leaves us without a lattice-matched substrate.

Despites these obstacles, the University of Oklahoma MBE group has made substantial progress in the growth of InSb quantum wells. The group run by Prof. Michael Santos holds the world record for room temperature mobility in a quantum well for any semiconductor material. This progress has enabled observation of interesting properties such as large zero field spin splitting [21] and high temperature ballistic transport [22], which can be exploited in novel electronic devices. Table 6.1 lists for comparison room temperature values of relevant parameters for GaAs, GaSb, InAs, and InSb. The combination of a small effective mass and a large dielectric constant contributes in making $\boldsymbol{r_s}$, a measure of the strength of many-body interactions,

ratio between interelectronic separation and the effective Bohr radius a_B^* small.

$$a_B^* = \frac{\hbar^2 \epsilon}{m^* e_2} \tag{4.1}$$

In fact,

$$E_F = \frac{\pi \hbar^2 n_s}{m^*} \tag{4.2}$$

$$E_c = \frac{e^2}{\epsilon} \sqrt{\pi n_s} \tag{4.3}$$

so now,

$$r_s = \frac{E_c}{E_F} = \frac{m^* e^2}{\hbar^2 \epsilon \sqrt{\pi n_s}} = \frac{r_e}{a_B^*} \tag{4.4}$$

where

$$r_e = \frac{1}{\sqrt{\pi n_s}} \tag{4.5}$$

Using m^*=0.014 m_e, ϵ=16.8ϵ_0, and n_s=n_0x10^{11} cm^{-2} for InSb, we arrive at the result:

$$r_s = \frac{0.3}{\sqrt{n_0}} \tag{4.6}$$

Extremely small r_s values predispose InSb to weak electron-electron interactions. However, the shallow dips seen at magnetic fields for filling fractions 2/3 and 1/3 (see figure 2.1), together with their behavior at various temperatures (not shown), are similar to those observed in modest quality (by today's standard) GaAs samples where FQHE was first reported [8] and hint to potential strong enough electron-electron interactions in InSb QWs. There is hope that, just like for GaAs, progress in material growth and design of QW structure will allow observation of stronger FQHE states in InSb-based 2DES.

Being a narrow band gap semiconductor, InSb suffers from strong non-parabolic energy bands; hence the effective mass and the Lande g-factor depend on the energy. This adds another level of complication in the description of the spectrum of InSb under tilted magnetic fields. What makes InSb attractive for the studies in this thesis is, the large m^*g^* value making it an ideal candidate for quantum Hall ferromagnetism studies by ways of tilted magnetic fields. Large m^*g^* as shown in the previous

chapter, leads to level crossings at relatively small tilt angles and readily accessible magnetic fields. Furthermore small effective mass and large Lande g-factor lead to large cyclotron and Zeeman gaps, making it easier to resolve orbital and spin related effects despite the considerable spin-orbit interaction.

	GaAs	InAs	GaSb	InSb
Effective mass($\frac{m^*}{m_e}$)	0.063	0.023	0.041	0.014
Intrinsic mobility (cm^2/V.s)	9000	39000	3000	77000
Intrinsic carrier concentration (cm^{-3})	2.1x10^6	1.0x10^{15}	1.5x10^{12}	2.0x10^{16}
Lattice constant ($\mathring{A}$)	5.653	6.058	6.096	6.479
Energy band gap (eV)	1.424	0.350	0.726	0.17
Spin-orbit split off energy(eV)	0.34	0.41	0.8	0.8
Electron Lande g-factor	-0.44	-17.5	-7.8a	-50.6
Dielectric constant (ϵ/ϵ_0)	12.9	15.1	15.7	16.8
Melting point (^{o}C)	1240	942	712	527
$(m^*/m_e)g^*$	0.028	0.402	0.320	0.708

Table 4.1: Room temperature data comparing relevant parameters of InSb to other III-V semiconductors. [23] [a]Reference [24].

4.3 InSb quantum well structure

The typical layer structure describing the samples used in this study is shown in Figure 4.1. They were all single quantum wells (QWs) grown on a semi-insulating GaAs(001) substrate by Prof. Santos's group. Because of the large lattice mismatch ($\sim$ **14.6%**) between GaAs and InSb, a buffer layer made of fully relaxed AlSb, $Al_xIn_{1-x}Sb$, and a dislocation filtering strained layer superlattice (SLS) made of InSb/ $Al_xIn_{1-x}Sb$ (or GaSb/AlSb for few samples) is grown on top of the substrate to even out the dramatic effect of the mismatch prior to the growth of the QW

structure. The QW consists of InSb sandwiched between $\boldsymbol{Al_xIn_{1-x}Sb}$ barriers with typical x values ranging from 5 to **15%**. An InSb cap that prevents the oxidation of $\boldsymbol{Al_xIn_{1-x}Sb}$ surface often terminates the structure. The InSb wells are thin (20-30 nm), with width (w) below or close to the critical thickness ($\boldsymbol{\sim 30nm}$) for strain relaxation in InSb/ $\boldsymbol{Al_xIn_{1-x}Sb}$ system. Carriers in the strained QW are provided by silicon delta-doped layers placed either in the two adjacent $\boldsymbol{Al_xIn_{1-x}Sb}$ barriers for symmetric structures or in the upper barrier for asymmetric structures. An additional silicon $\boldsymbol{\delta}$-doped layer close to the cap layer provides electrons for the surface states. The distance separating the doping layers and the QW is referred to as the spacer thickness d. For further details on the growth conditions of our samples see references [25] and [26].

Table 6.2 gives the most relevant parameters of all the samples used in this study. The geometry of the samples (see figure 4.2) ranges from simple van der Pauw square ($\boldsymbol{\sim}$ 5x5 $\boldsymbol{mm^2}$) with 8 indium contacts at the corners and mid-section of each side, to spider mesas and standard Hall bars, etched down to the GaAs substrate. Details on sample processing can be found in appendix 3. The samples were all operated in the regime where only the lowest electrical subband was populated. For some samples, the density was tuned using a front gate deposited using the technique detailed in chapter 6.

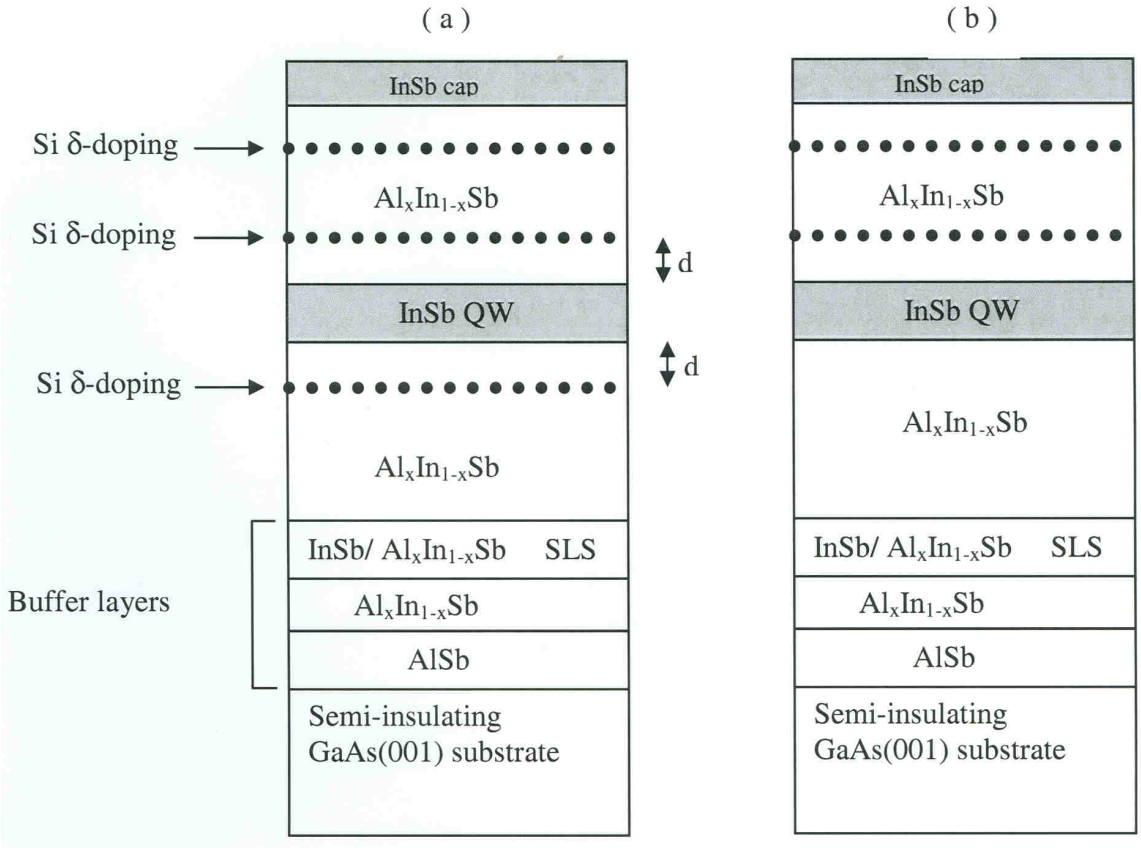

Figure 4.1: Schematics (not to scale) of typical sample structures used in this study. a) symmetric sample and b) asymmetric sample.

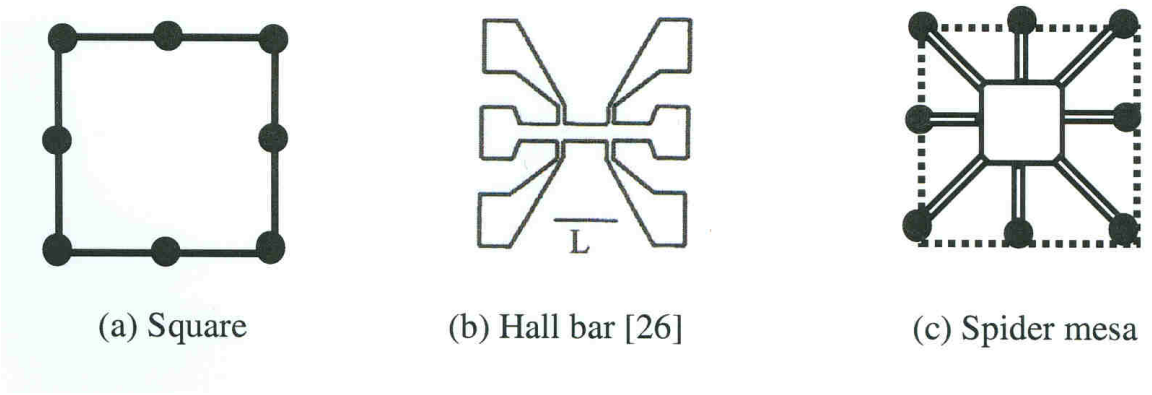

Figure 4.2: Sample geometries used for this study: (a) square sample; typical side of 5 mm. (b) Hall bar; typical width of 50 μm and voltage probe length L (c) spider mesa; typical inner square size 2x2 mm^2.

The carrier density dependence on gate bias in gated samples (see figure 4.3) shows a behavior typical for remotely doped structures: the carrier density (n_s) increases linearly with the gate voltage (V_G) up to a threshold voltage (V_{th}) and then approaches saturation of n_s at voltages higher than V_{th}. Such a transition from linear dependence to saturation for n_s has been observed and explained by Hirakawa *et al.* [27] as follows. When V_G is smaller than V_{th}, the quasi Fermi level in the doped barrier is well below the donor level, the Si donors are fully ionized and the gated structure acts like a parallel plate capacitor, resulting in the linear dependence of carrier concentration on V_G. At the threshold voltage V_{th}, the donor level is just few kT above the quasi Fermi level so that some electrons can be thermally activated to the donor level where ionized donors capture them. With larger values of V_G, the quasi Fermi level may cross the donor level, and a neutral region forms in the doped barrier. Consequently, any change of the gate voltage will be shielded by the neutral region, leading to the saturation of n_s.

Structural and transport characterization on structures similar to our samples showed that they contained many defects, namely threading microtwins and dislocations which originated at the GaAs/AlSb interface and propagate all the way through

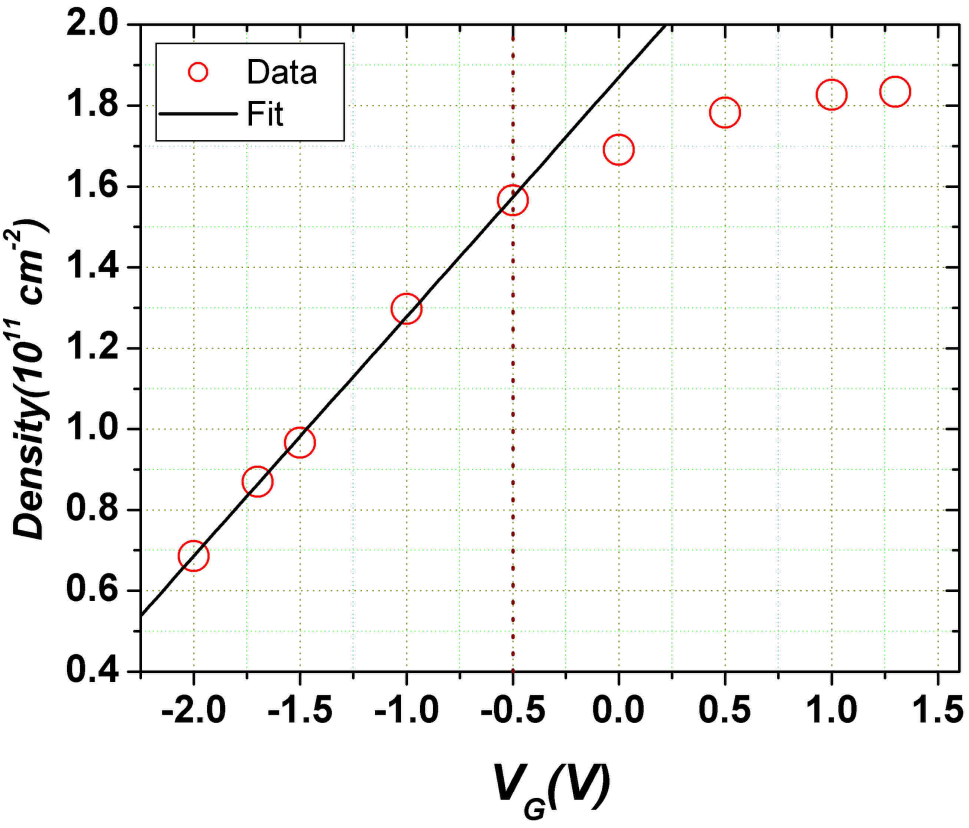

Figure 4.3: Typical behavior of gate voltage effect on carrier density in InSb QW at low temperatures ($\sim$ 4 K). For this sample (Sample S517), the threshold voltage is $\sim$ -0.5 V.

the QW region. Transmission electron microscopy (TEM) analysis by Mishima [28] revealed that when the microtwins cut through the QW region, they introduce spatial offset between the two parts of the QW that they separate, creating significant large angle scattering. The dislocations have an asymmetric distribution (larger density along $[1\bar{1}0]$ direction), which correlates with anisotropic electron mobility. Additional scattering mechanisms that may limit carrier mobility in our samples include, interface roughness between the well and the barriers, long range scattering from remote ionized impurities in the delta-doped layers, and short range scattering from the ionized background impurities in the well. The long range potential arises from the fact that a fluctuation of wave vector k in the density of the ionized impurities in the delta-doped layer, sets up an electrostatic potential proportional to $\frac{exp(-kd)}{k}$ in the quantum well [29]. The ionized background impurities in the QW originate from unintentional doping which in the growth system at the University of Oklahoma was found to result in p-InSb with a hole density $\leq$ 1x $\mathbf{10^{15}}$ $\boldsymbol{cm^{-3}}$ at 77 K [30]. Studies by our group and others [31] revealed a strong dependence of the carrier mobility on the well density, when tuned using a front gate bias (see figure 4.4). This indicates that interface roughness does not play a significant role in our samples. If it did, the Hall mobility would be independent of the 2DES density. Interface roughness tends in general to be strong in very thin wells (w $<$ 4 nm). Because the unintentional background doping in the well is very low, for our study it is fair to say that structural defects and remote ionized impurities from the delta-doped layers are the major contributors to carrier scattering in our samples.

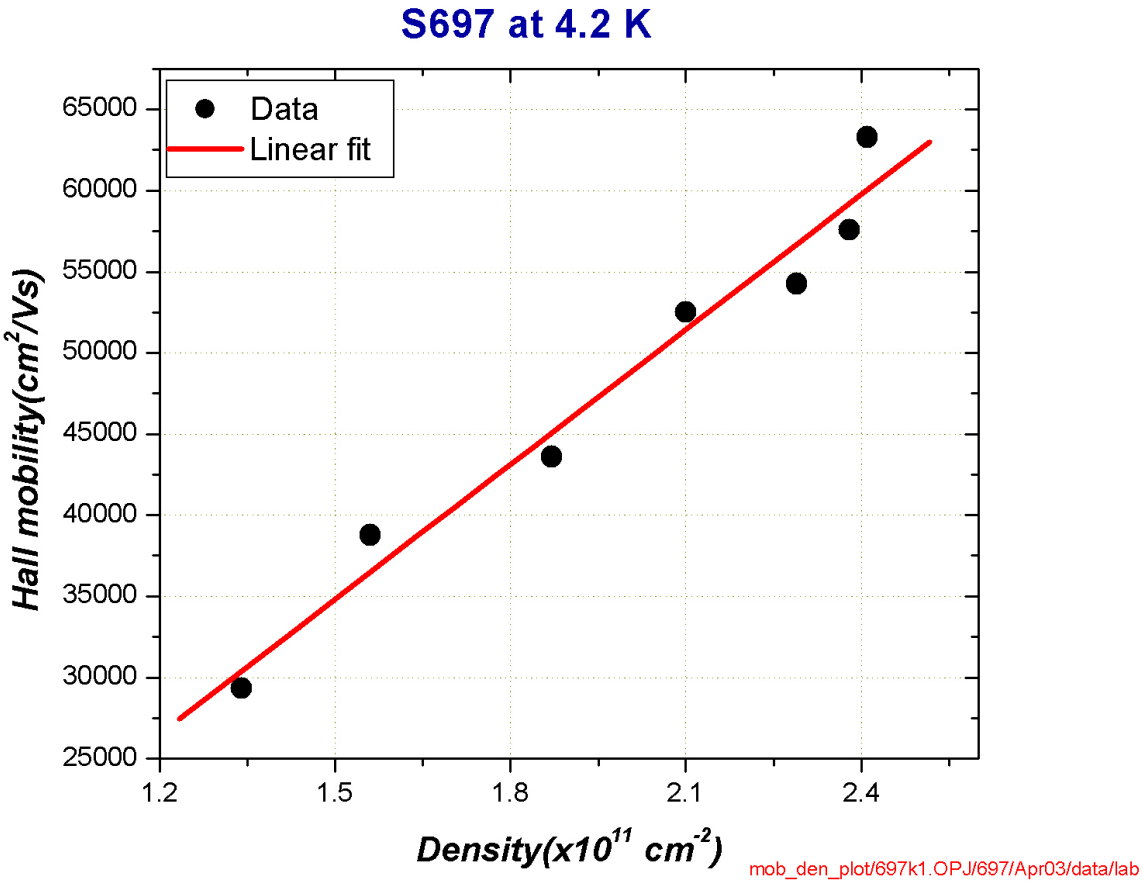

Figure 4.4: Hall mobility versus density for sample S697 at 4.2 K. The density was tuned using a front gate voltage. The change of Hall mobility with carrier density indicates that interface roughness does not contribute significantly to carrier scattering.

wafer	sample	geometry	x (%)	w (nm)	d (nm)	doping sym.	n_s/n_0	μ(77K)
S285	S285	square	9	30	50	asym*	1.4	69142
S372**	S372	Spider	9	30	30	sym	2.5	124694
S391**	S391	Spider	5	30	40	sym	0.6	100348
S413	S413	square	9	30	60	asym*	1.1	91343
S696	M0409a	Hall bar	9	30	60	sym	1.8	109917
S697	S697	Spider	9	20	30	sym	2.4	127936
S702	S702	Spider	9	20	30	sym	2.1	129621
S702	M0315b	Hall bar	9	20	30	sym	1.9	129621
S702	M0322c	Hall bar	9	20	30	sym	1.9	129621
S715	S715	Spider	9	20	15.7	asym	1.7	44039
S715	S715	square	9	20	15.7	asym	1.7	44039
S842	S842	square	15	25	40	sym	4.1	77271
S842	N1016E	Hall bar	15	25	40	sym	4.1	77271

Table 4.2: Relevant parameters of all the samples investigated. The mobilities values are data from the as-grown samples.* The uppermost Si-delta layer was not introduced in these samples.** GaSb buffer and GaSb/AlSb SLS used instead.n_0=10^{11} cm^{-2} .μ is in (cm^2/V.s) and sym.(asym.) means symmetric(asymmetric)

Chapter 5

Quantum Hall Ferromagnetism in InSb Quantum Wells: Experiments and Results

5.1 Introduction

Two-dimensional electronic systems (2DESs) in strong magnetic fields provide a fertile ground where subtleties of the physics at the microscopic level can be investigated and the results used to gain insights into what might be happening when atoms are bound to form larger structures. Energy levels overlap, and repulsion and/or hybridization play a vital role in the complexity of bulk materials. The overall properties of materials turn out to depend not only on the details and nature of the interactions involved but also on how the energy levels are distributed and populated. For example, ferromagnetism is observed mostly in materials with partially filled 3d or 4f shells. Also, in the bulk form, materials assume different degrees of conductivities depending on how their energy bands (valence and conduction bands) are distributed and populated. By examining in a 2DES the effects of forcing one filled spin-split Landau level (LL) to degeneracy with an empty spin-split LL of opposite real spin, we may shed some

light into what nature does at the atomic level where the system tries to minimize its energy under similar circumstances.

In this chapter we provide details of our experimental investigation on what happens when different spin-split LLs in InSb-based single quantum wells are forced into degeneracy using the tilted field technique. We start by presenting and justifying our experimental procedure; next the results are presented and discussed in the light of theory of quantum Hall ferromagnetism. Finally a summary of what we have learned and what requires further investigation is given.

5.2 Experimental procedure

We force different LLs into degeneracy using the tilted field technique introduced in chapter 3. The exceptionally large $\boldsymbol{m^*g^*}$ ($\boldsymbol{m^*}$ is the electron effective mass and $\boldsymbol{g^*}$ is the electronic Lande g-factor) of InSb allows level crossings to occur at relatively small angles and at readily available magnetic fields. Among all the commonly studied semiconductors, InSb is second only to AlAs as material of choice for tilted field experiments. Table 6.1 gives a list of popular semiconductors and the angles at which the first coincidence *i.e.*, crossing between the n = 0 spin up and the n = 1 spin down LLs occurs, assuming a non-interacting system. As was shown earlier, if r is the coincidence index and theta the angle between the applied magnetic field and the sample normal, level crossings in a non-interacting 2DES will occur when

$$\boldsymbol{cos(\theta) = \frac{1}{2r} m^* g^*} \tag{5.1}$$

Theoretical calculations by Giuliani and Quinn [32] on the $\boldsymbol{\nu = 2}$ QHE state predicted that the spin transition from paramagnetic to ferromagnetic states during the tilted field experiments would take place as a sudden jump at an angle smaller than the one from single particle calculation if electron-electron interactions are considered. A more realistic calculation by Yarlagadda [33] that included disorder-broadening of LLs and screening effect, not considered by Giuliani and Quinn, showed that the ratio of

the Coulomb energy to the level broadening must be greater than a certain threshold value for the magnetization jump to occur. Therefore, during our experiments, the values of the angles for non-interacting electrons plus 2 degrees were considered as upper bounds for the coincidence.

Semiconductor	Effective mass (m*)	Lande g-factor	coin. angle(r = 1)
Si	0.26	2.0	78.5^{o}
GaAs	0.067	-0.44	89.1^{o}
InAs	0.023	-15	80.0^{o}
$\mathbf{In_{0.53}Ga_{0.47}As}$	0.041	-4.1	85.2^{o}
AlAs	0.41	-1.9	67.1^{o}
InSb	0.015	-51	67.5^{o}

Table 5.1: First coincidence (r = 1) angle for most common semiconductors assuming non-interacting electrons. $\boldsymbol{m^*}$ and $\boldsymbol{g^*}$ in the table are the 4 K values.

5.3 Illustration of the experimental procedure

Because the cyclotron and the Zeeman gaps determine the strength of the QHE effect, we keep the cyclotron gap (which depends only on the perpendicular component of the applied field) fixed (fixed filling factor) and increase the Zeeman gap via increasing the total field ($\boldsymbol{B_{total}}$) till the levels of interest overlap. The experimental monitoring of the level crossing is quite simple. When we are dealing with purely single particle levels, when no QHF is expected, starting at zero tilt angle, the QHE state of interest must be strong. But as the sample is tilted, the QHE state weakens *i.e.*, the minimum in the longitudinal resistance rises up in resistance as a result of reduction of the energy gap around the Fermi level. The QHE state disappears at the coincidence angle, because of the vanishing of the gap at the Fermi level. Further tilt beyond the coincidence angle, causes the QHE state to reappear as the gap at the Fermi level is

reopened when the energy levels go past one another. Figure 5.1 gives a schematic of the evolution of the $\nu = 2$ QHE state under tilted magnetic fields.

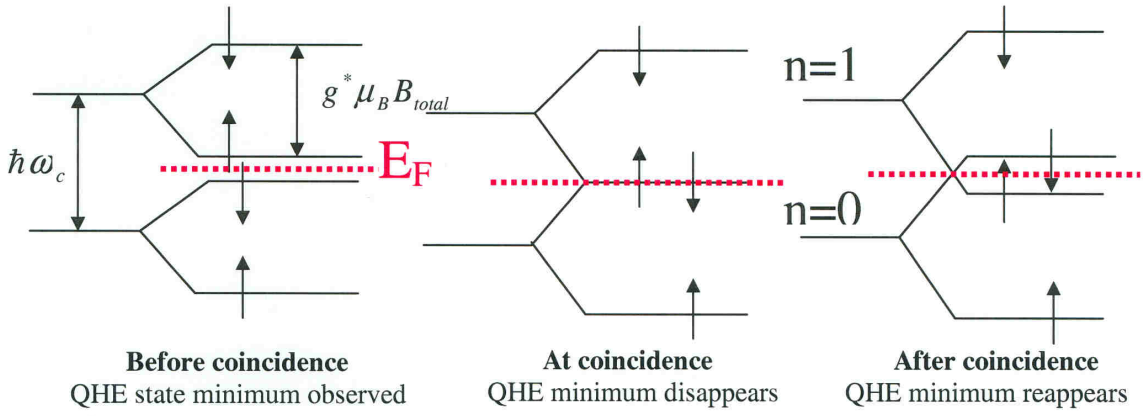

Figure 5.1: Schematic of the evolution of the LLs in a non interacting system when the $\nu = 2$ QHE state is under tilt.

In a system with perfectly parabolic energy bands, even QHE states ($\nu = 2, 4, 6$) disappear at the first coincidence angle, the odd states ($\nu = 3, 5, 7$) at the second coincidence, and at the third coincidence, only ($\nu = 4, 6, 8$) states disappear while at the fourth coincidence, odd filling states starting at $\nu = 5, 7, 9$ disappear. Figure 5.2 shows the energy level configuration for the first three coincidence indices. Because level crossing is induced by enlarging the Zeeman gap, the $\nu = 1$ QHE state will never disappear upon tilting. The $\nu = 2$ and 3 states disappear once at r = 1 and 2 respectively, while $\nu = 4$ and 5 disappear twice at r = 1 and 3, 2 and 4 respectively, and $\nu = 6$ and 7 states disappear 3 times etc.

5.4 Experimental setup

Our experiments are carried out in a standard setup for QHE study with the sample probe equipped with a rotating stage. For this work, we used either the low temperature laboratory at the University of Oklahoma or the facilities of the National High

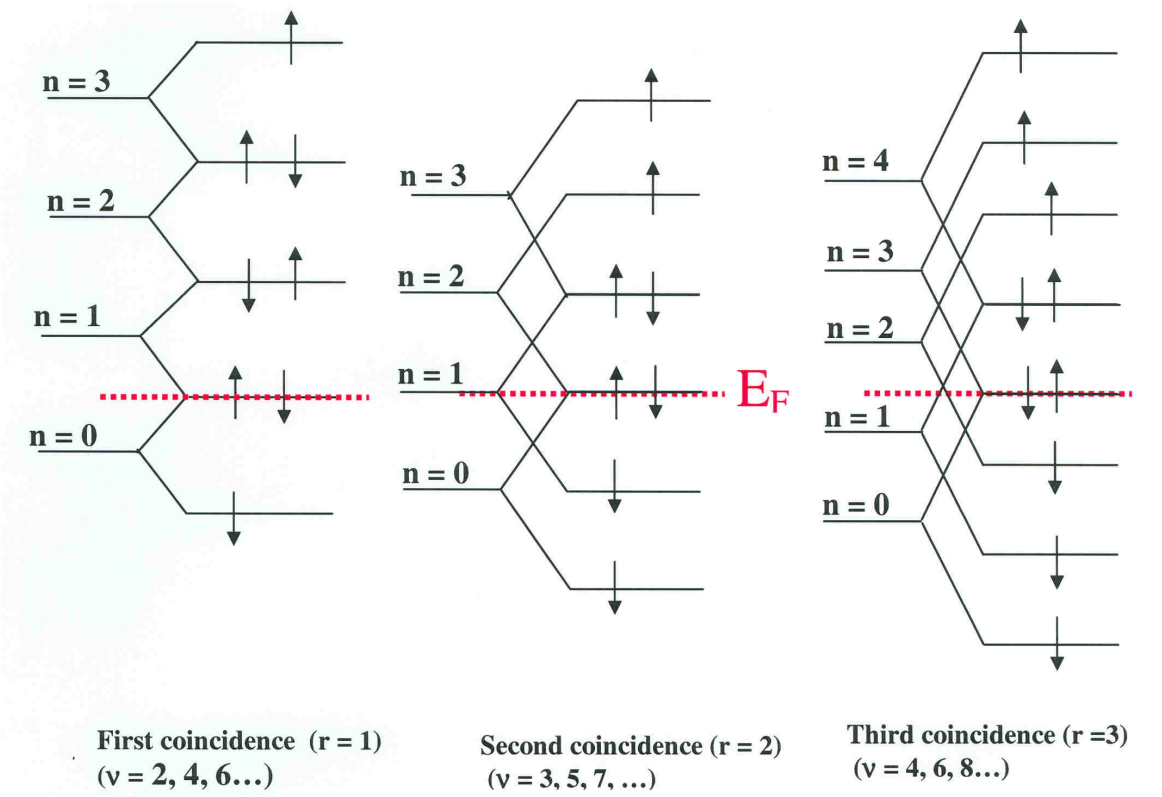

Figure 5.2: Schematic of energy level configuration for the first three coincidence indices.

Magnetic Field Laboratory (NHMFL) in Tallahassee, Florida. At the University of Oklahoma, we used a pumped ^{3}He cryostat equipped with a 9 Tesla superconducting magnet, capable of attaining temperatures just below 0.5 K. The home-built tilter for this setup can cover angles ranging from $\mathbf{0^o}$ to about $\mathbf{85^o}$. At NHMFL, we had access to the millikelvin facilities (SCM I and SCM II) and cells using resistive magnets. The millikelvin facilities house a dilution refrigerator (SCM I) and a pumped ^{3}He cryostat (SCM II) all equipped with an 18 Tesla superconducting magnet. The dilution refrigerator operates at a base temperature of 30 mK, but the operation temperature can be raised to $\sim$ 1.3 K by dumping heat (via resistive heaters) in the mixing chamber. The ^{3}He cryostat was operated in the 17 K to 0.25 K temperature range. The resistive cells were equipped with a 33 Tesla resistive magnet and could fit a dilution

or a pumped ^{3}He cryostat. The sample probe at the millikelvin facilities had enough room to fit multiple samples (2 to 4) while the reduced bore on the resistive magnets allowed one sample to be loaded at the time. The tilters at the NHMFL could cover very broad angle range, typically from $\mathbf{-180^o}$ to $\mathbf{180^o}$.

5.5 Experimental protocol

Typical experimental protocol consisted of the following, irrespective of the system on which we were running the experiment.

5.5.1 Bench test

The samples were mounted to the probe and checked for good wiring. On the bench, contact-to-contact resistance should be low, typically below 8.0 k$\mathbf{\Omega}$. The tilter was next tested to ensure that the samples would rotate smoothly without any hindrance or entanglement between wires. The tilter consists of a micrometer head at the top of the probe, attached via a Kevlar string, to one end of the rotating body held on axis by two pivots. A second string is run in the opposite direction and attached to a small spring. With this arrangement, the linear displacement of the string, read on the micrometer head, causes the rotation of the rotating body that houses dual in-line packages (DIP) sockets (at NHMFL) or a plastic leaded chip carrier (PLCC) socket (at OU). At this point, the displacements corresponding to $\mathbf{0^o}$ and $\mathbf{90^o}$ tilts are jotted down in the lab notebook. The purpose of this rough tilter calibration is to keep track of the tilting direction during the more accurate low temperature tilter calibration.

5.5.2 Low temperature hunt for best contact configurations

After loading the sample in the cryostat and cooling the system to liquid Helium temperature (4.2 K) or less, we looked for the contact configurations giving the best

longitudinal or Hall resistances by performing magnetic field sweeps with the field range covering at least three QHE states. The best contact configurations had nearly zero longitudinal resistance minima, linear low field Hall resistance, and well defined plateaus for each integer QHE state.

5.5.3 Tilter calibration

Once the best contact configurations were determined, several low magnetic field sweeps at various displacements of the tilter were taken. These linear displacements corresponded to rotation of our samples via the linear to angular coupling mechanism of the tilter. From the classical Hall effect results, the low field Hall resistance slope (S) is proportional to the cosine of the angle between the applied B-field and the sample normal.

$$\boldsymbol{S = \frac{cos(\theta)}{n_s e}} \tag{5.2}$$

We measured the Hall slope (S) as a function of the tilter displacement (X) and fitted the data with a cosine function of the form:

$$\boldsymbol{S = P_1 cos(P_2 X + P_3)} \tag{5.3}$$

Where $\boldsymbol{P_1}$, $\boldsymbol{P_2}$, and $\boldsymbol{P_3}$ are the fitting parameters. $\boldsymbol{P_1}$ is sample dependent and related to carrier concentration; $\boldsymbol{P_2}$ is a measure of the linear displacement versus angular change of the tilter; and $\boldsymbol{P_3}$ is the offset from zero tilt. From the best fit, the tilter angle is given by:

$$\boldsymbol{\theta = P_2 X + P_3 \pm 360n, n = 0, 1, 2...} \tag{5.4}$$

The last term in the equation giving the angles, takes care of the $\boldsymbol{360^o}$ periodicity of the cosine function, while its sign, helps keep the angle between $\boldsymbol{-180^o}$ and $\boldsymbol{180^o}$. The ambiguity introduced by the parity of the cosine function is confidently removed based on the rough tilter calibration performed on the bench. Figure 5.3 shows a typical tilter calibration performed at $\sim$ 1.7 K. the two samples (S697 and S702) were mounted on the same 14-pin DIP header. In figure 5.3 (a) the variation of the

Hall slope with the displacement is shown on a scatter plot. The fits are used to determine the tilt angle represented on figure 5.3(b). The data show angle offset of less than $\mathbf{5}^{o}$ between the two samples, the offset decreasing with increasing tilt. The offset most likely occurred during the attachment of the samples to the DIP header.

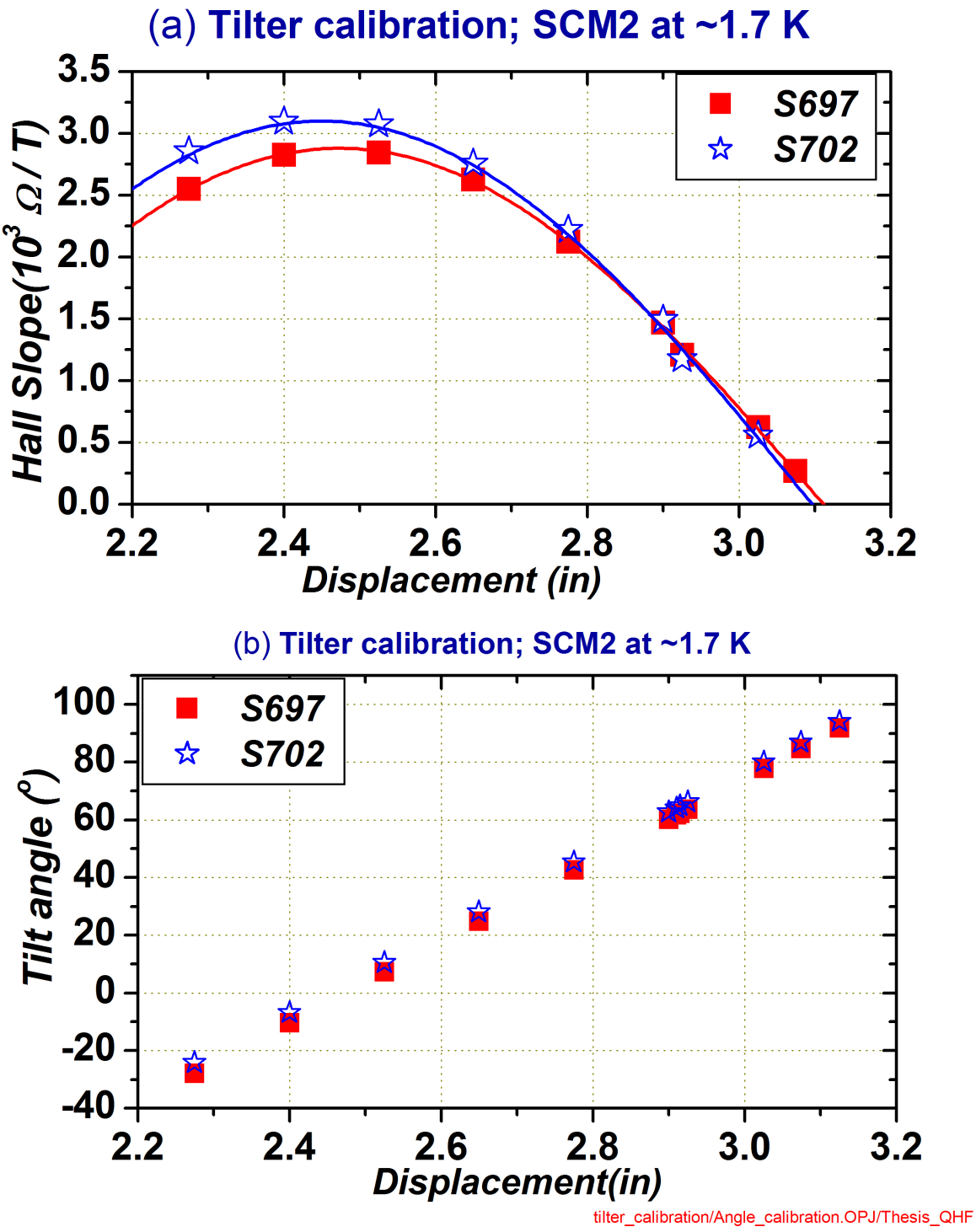

Figure 5.3: Typical tilter calibration graphs: (a) Hall slope versus tilter displacement. The lines are the best fits to the experimental data (symbols). (b) Angle versus tilter displacement deduced from (a) as described in the text.

5.5.4 Magnetoresistance measurements

Once the tilter is calibrated, magnetoresistance data at various tilt angles are collected. We used four-point probe technique with the standard low frequency ac lock-in technique. The excitation current was kept low (equal or less than 100 nA) so to minimize sample heating during the experiments. To avoid errors in the tilter displacement due to play in the vernier on the tilter and/or reading errors, the displacements were dialed-in by moving the cursor consistently in the same direction and the readings done with the help of a magnifying glass at normal view angle.

5.6 Experimental results

5.6.1 Single particle behavior

In systems with weak electron-electron interactions where the QHF is not expected, the minima in $\boldsymbol{\rho_{xx}}$ defining the QHE states must rise in resistance with increasing tilt, turn into resistance maxima at coincidence when the energy gap around the Fermi level vanishes, and reappear with further tilt. Figure 5.4 presents the results for a low-density sample ($\boldsymbol{n_s} = 0.6\text{x}\mathbf{10^{11}}\ \boldsymbol{cm^{-2}}$) that is consistent with the single particle picture. As expected, the first three coincidences occur at $\mathbf{67.5^o}$, $\mathbf{77.3^o}$, and $\mathbf{81.2^o}$ respectively. We also observed a similar behavior in a high-density sample ($\boldsymbol{n_s} = 2.2\text{x}\mathbf{10^{11}}\ \boldsymbol{cm^{-2}}$) (see figure 5.5). For the high-density sample however, the trend is only observed for high filling factors ($\boldsymbol{\nu > 4}$).

In all the samples investigated, low-density samples ($\boldsymbol{n_s} < 1.4\text{x}\mathbf{10^{11}}\ \boldsymbol{cm^{-2}}$) displayed non-interacting behavior at all filling factors while high-density samples exhibited this behavior only at high fillings ($\boldsymbol{\nu > 4}$). The observation of persistent resistance minima at low filling factors in high-density samples (see figure 5.5) is indicative of strongly interacting systems, and hence quantum Hall ferromagnets.

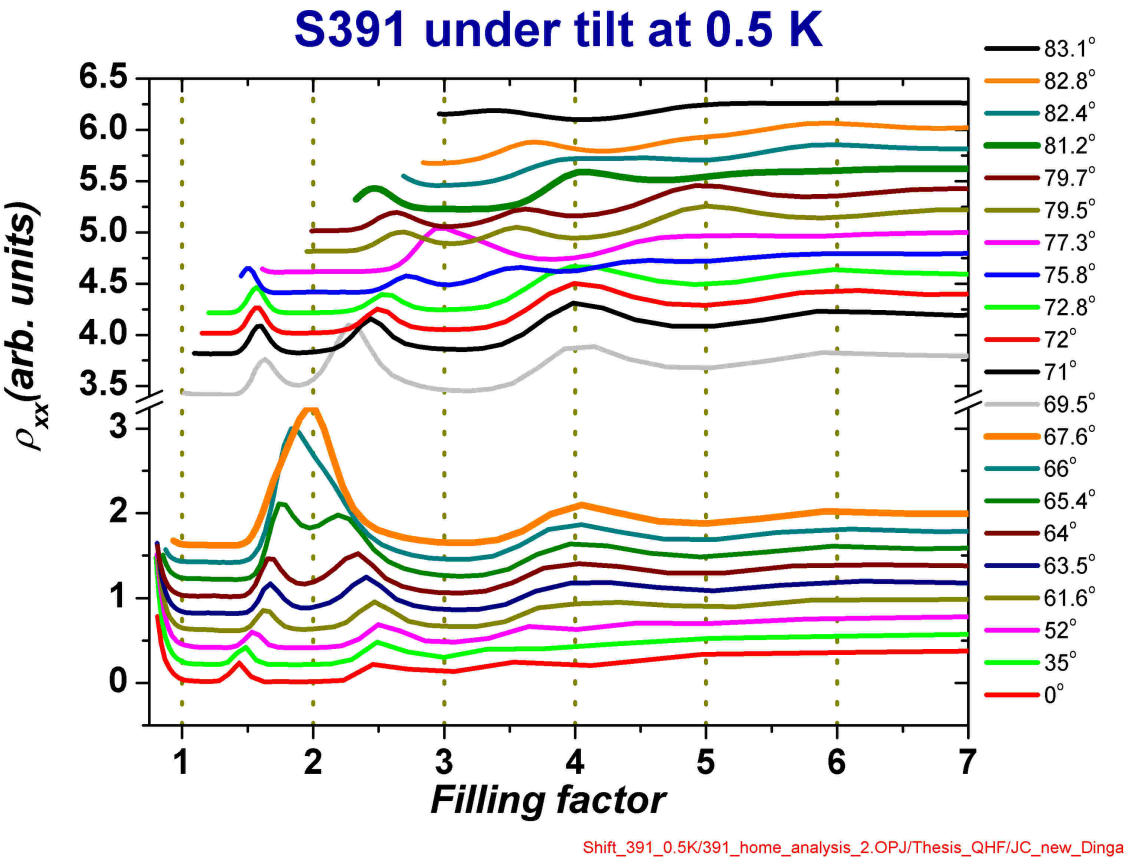

Figure 5.4: Low density sample (S391; $\boldsymbol{n_s} = 0.6\text{x}\mathbf{10^{11}}\ \boldsymbol{cm^{-2}}$) under tilted fields at 0.5 K. Note the disappearance and reappearance of all the QHE states at filling factors greater than 1.

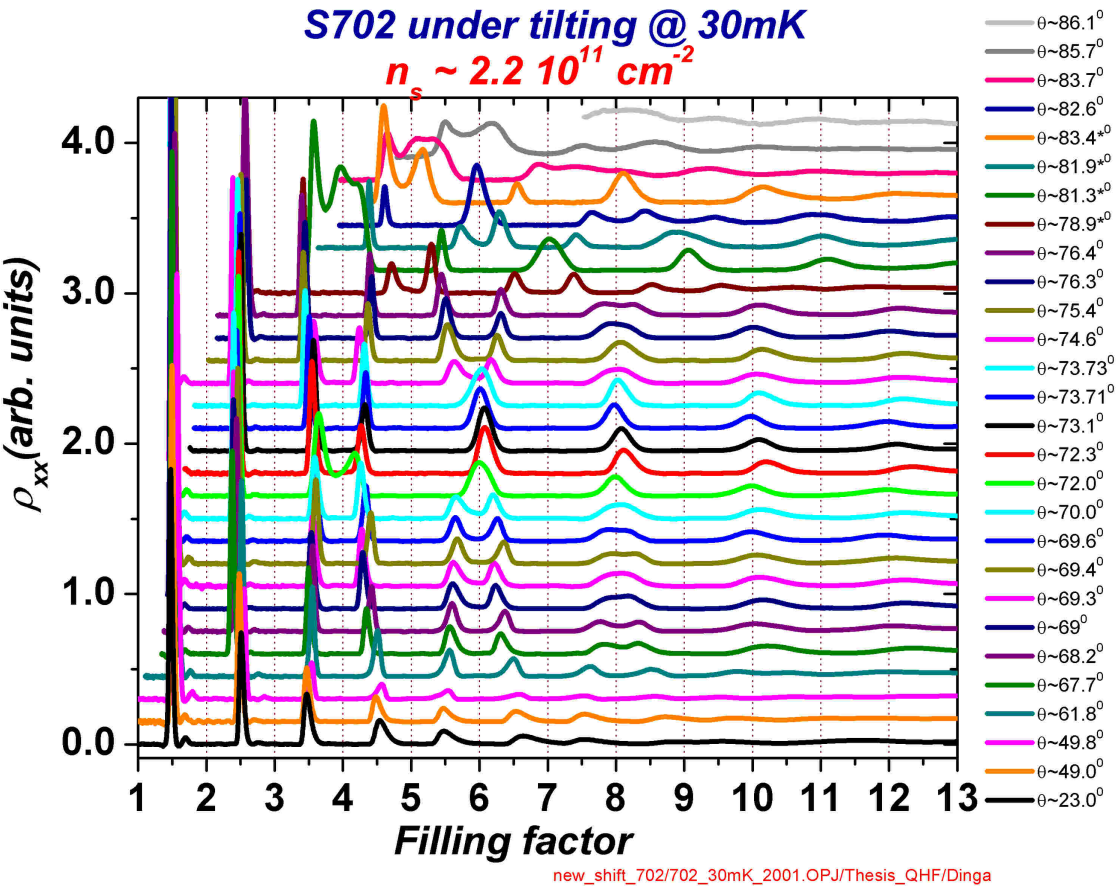

Figure 5.5: High density sample (S702) under tilted fields at 0.03 K. Note the disappearance and reappearance of all the QHE states at filling factors greater than 4, while QHE states at lower fillings seem unaffected.

5.6.2 Quantum Hall ferromagnetism

. When the electron-electron interactions are stronger than the Zeeman energy, the two levels approaching the Fermi level will not overlap. In fact this is the regime, according to Giuliani and Quinn, where the spin phase transition would occur by a sudden jump before the single particle coincidence angle. According to Hunds rule, at degeneracy between an empty spin-down level and a filled spin-up level, the low energy configuration consists of all the electrons having the same spin orientation, i.e. preservation of an energy gap around the Fermi level, hence the persistence of the QHE state. This hallmark of quantum Hall ferromagnetism has indeed been observed at integer quantum Hall states in material systems such as AlAs[16], InGaAs [34], InAs [35], CdMnTe [36], and GaAs [37]. In the following section, we give details of features that we observed in InSb-based quantum Hall ferromagnetic states.

Temperature effect

As shown in figure 5.5, QHE states with low filling factors show very little activity upon tilting at low temperatures, but keeping the sample at tilt angle where level crossings were expected and raising the system temperature, revealed a resistance peak within the QHE resistance minimum that grows with increasing temperatures. Figure 5.6 and figure 5.7 show the behavior of the $\boldsymbol{\nu} = 2$ and 3 quantum Hall ferromagnets. The metallic-like behavior ($\frac{\boldsymbol{d\rho}}{\boldsymbol{dT}} > 0$) of these resistance features, also reported in other systems, is understood as resulting from the ferromagnetic nature of the states.

The origin of the resistance feature is described within the QHF theory as follows. At coincidence, the ground state of the system can be composed of two possible pseudospin phases. At temperatures above 0K, both pseudospin states are present, separated by domain walls. Transport in the system involves scattering of carriers at the domain walls, hence the enhanced resistance [38]. At lower temperatures, there are fewer domains, thus fewer domain walls are formed and because carriers are

scattered less, a smaller resistance peak is observed. At higher temperatures, just as in standard ferromagnets, the system is stabilized by the formation of many smaller domains. The proliferation of domain walls that results, leads to enhancement of the resistance peak. The split of the longitudinal resistance minima into two does not create new QHE states. The confirmation of the preservation of the QHE states despite the onset of dissipation can be seen in the Hall resistance trace in figure 5.6. The Hall plateau is well preserved and a resistance bump indicative of loss of incompressibility appears only where the longitudinal resistance is significant. The fact that the resistance peak in the $\boldsymbol{\nu} = 3$ QHF is large even at the base temperature of 0.03 K is indicative of a weaker exchange interaction in this state. Figure 5.8 shows the temperature effect on $\boldsymbol{\nu} = 2$ QHF over a broader temperature ranges. The sample is the same as in figure 5.6, but the carrier density was increased using gate bias. The change in the line shape of the split resistance minimum at temperatures above 1.5 K is nothing but the result of the relative temperature variation of the features defining the overall shape. A model of the temperature variation of the magnetoresistance of the $\boldsymbol{\nu} = 2$ QHF shown on figure 5.9 duplicates the line shape of the experimental data. The model is described in appendix 4.

Activation energy studies

To gain a better understanding of transport mechanism in observed quantum Hall ferromagnets, we performed activation energy studies by measuring the temperature dependence of the resistance peak and valleys. The data on figure 5.10 are consistent with $\frac{\mathbf{1}}{\sqrt{\boldsymbol{T}}}$ activated transport *i.e.* Coulomb gap hopping transport. It is likely that transport occurs by hopping of carriers from one pseudospin phase to the next. Fitting the data with:

$$\boldsymbol{\rho_{xx} = \rho_0 exp(-\sqrt{\frac{T_0}{T}})} \tag{5.5}$$

gives the characteristic temperature $\boldsymbol{T_0}$, related to the localization length by:

$$\boldsymbol{T_0 = \frac{Ce^2}{k_B \epsilon \epsilon_0 \xi}} \tag{5.6}$$

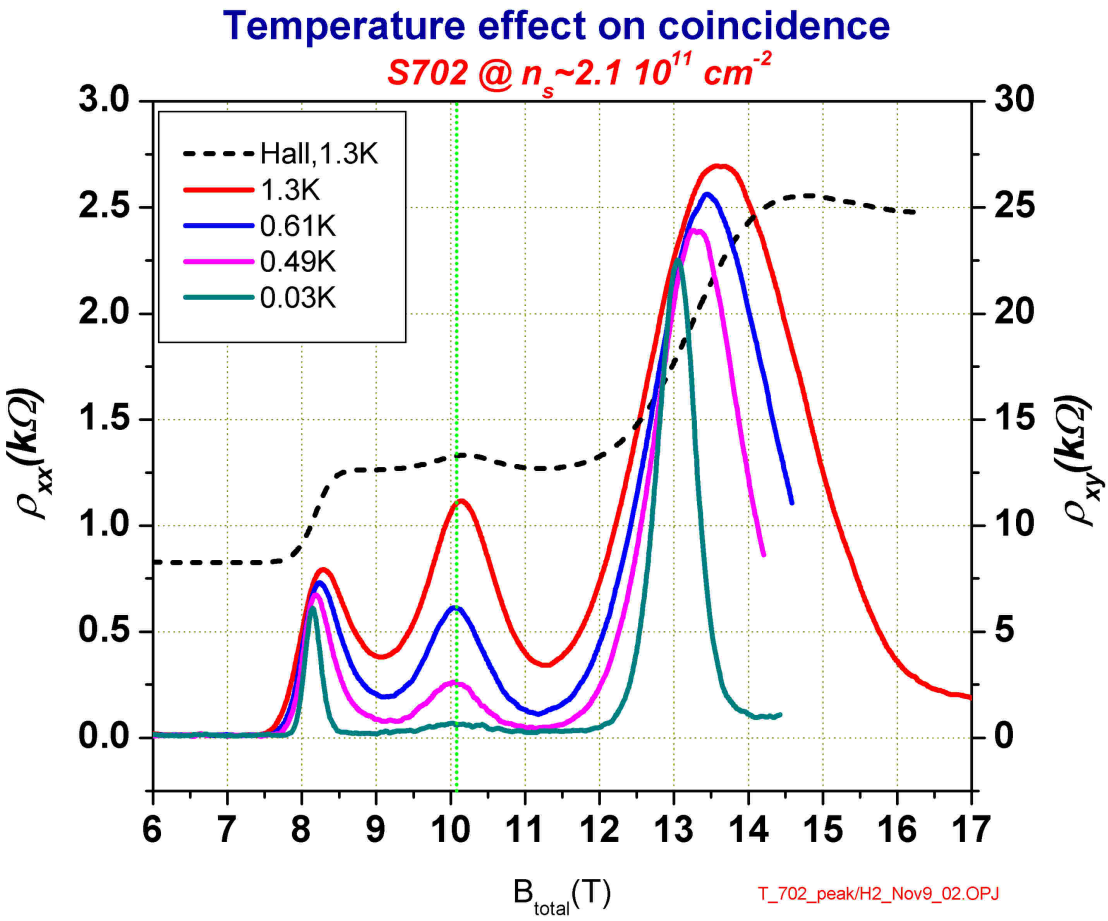

Figure 5.6: Temperature effect on the $\nu = 2$ QHF in S702. The vertical dotted line indicates the location of filling factor 2.

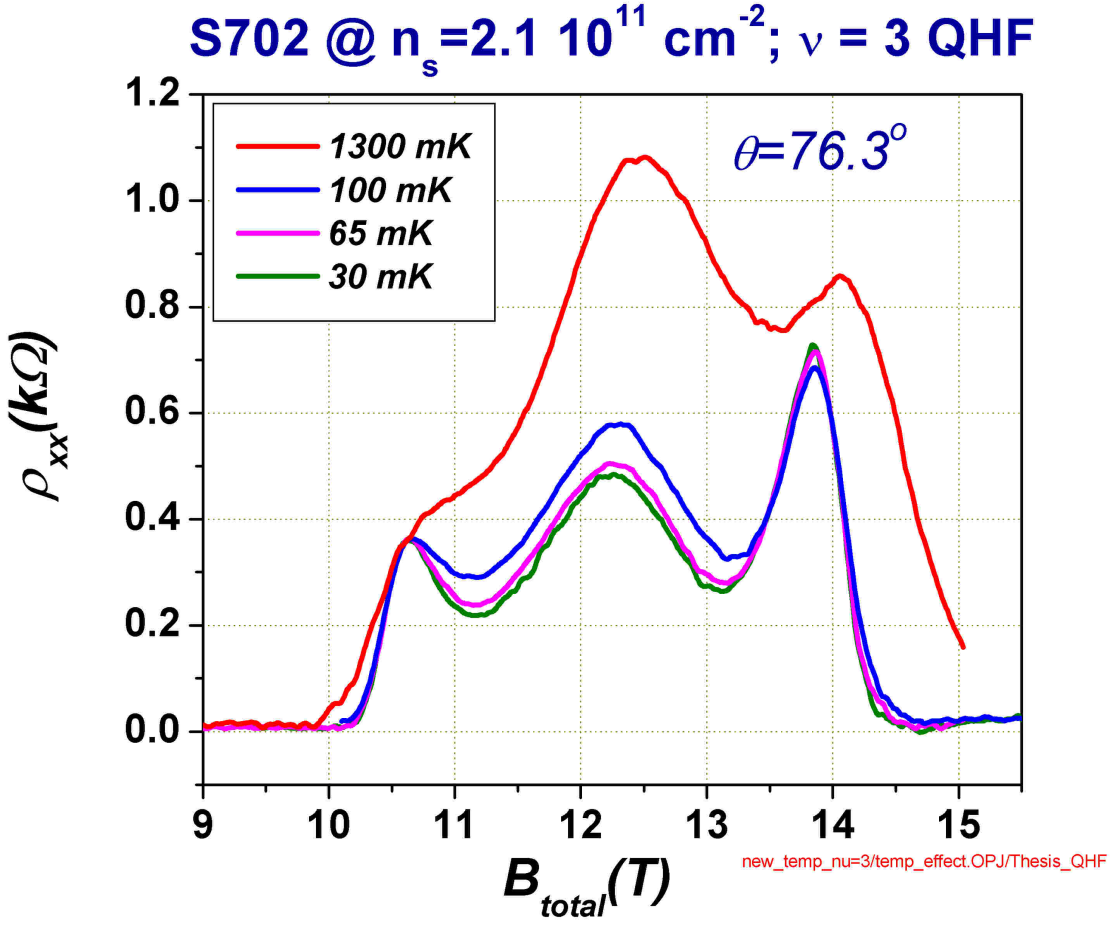

Figure 5.7: Temperature effect on the $\nu = 3$ QHF in S702. The resistance peak grows with increasing temperatures. Note however that unlike the $\nu = 2$ case, the resistance peak is large even at the base temperature of 30 mK.

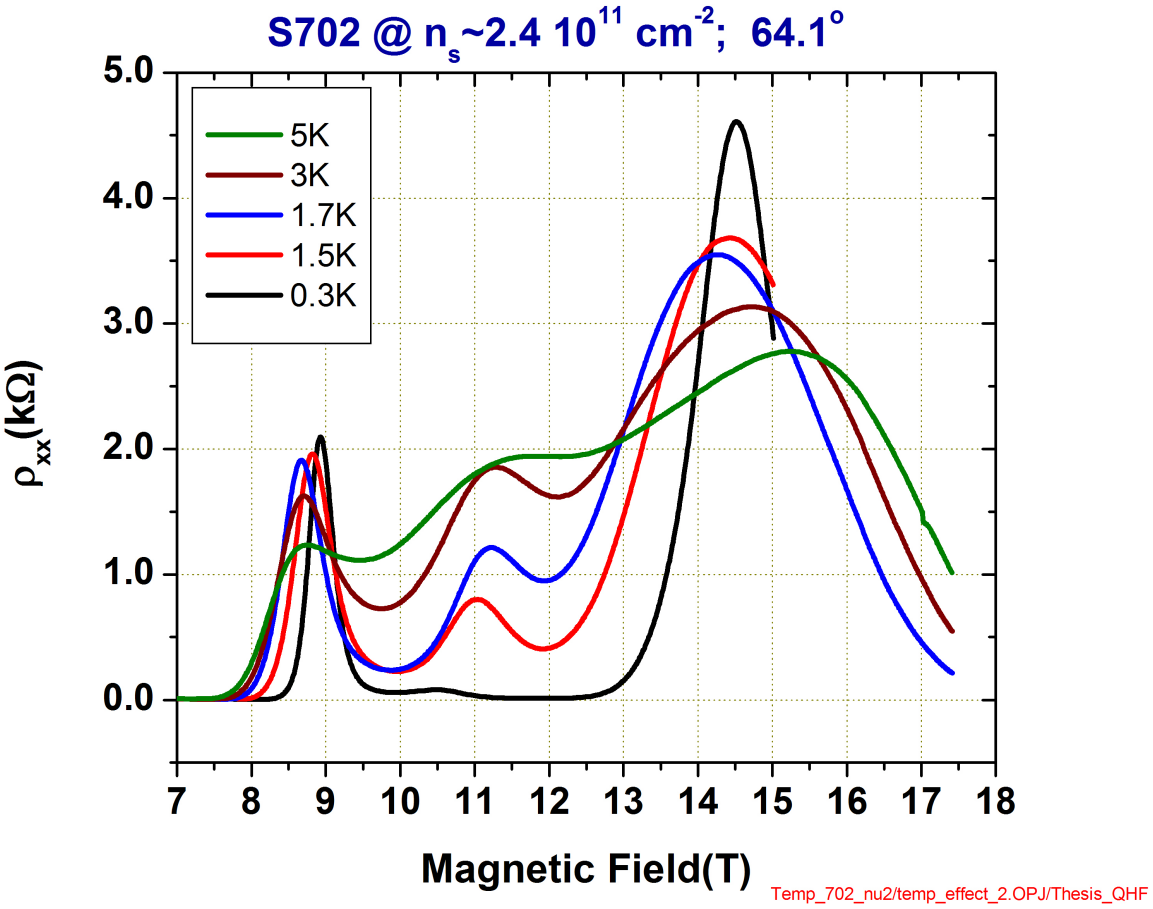

Figure 5.8: Temperature effect on the $\nu = 2$ QHF in S702 over a broader temperature range. Note the change in line shape of the magnetoresistance with increasing temperatures.

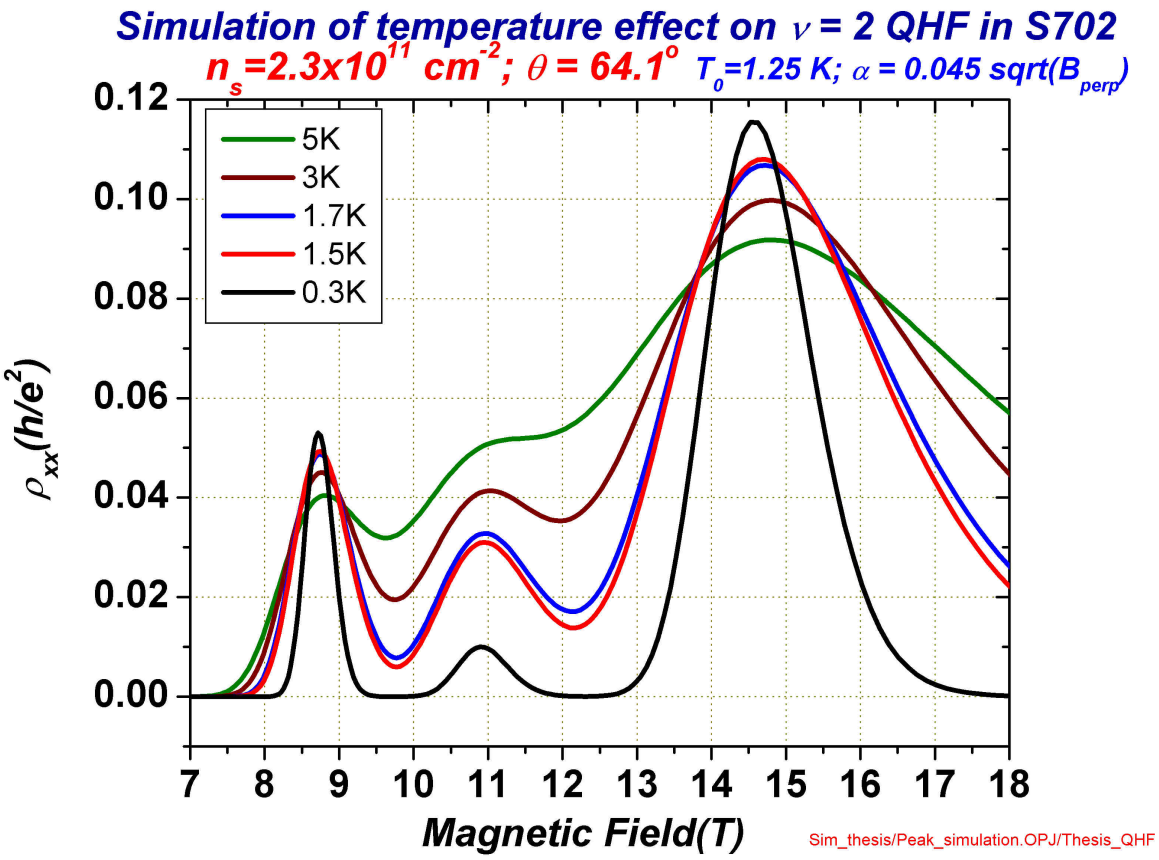

Figure 5.9: Simulation of the temperature effect on the $\boldsymbol{\nu} = 2$ QHF in S702. The model captures the line shape change of the magnetoresistance with increasing temperatures seen in figure 5.8

With C = 6.2 [39] for 2DES. Using T_0 = 10 K, the localization length is of the order of 7 μm. The Coulomb gap hopping transport observed in QHF in InSb is unique in comparison to activation studies in other integer QHF systems. In narrow GaAs QWs, a simple 1/T activation was observed [15]; in AlAs [16], a deviation from the 1/T activated transport occurred at low temperatures; while the resistance peak showed nearly no temperature dependence in wide parabolic GaAs QWs [40].

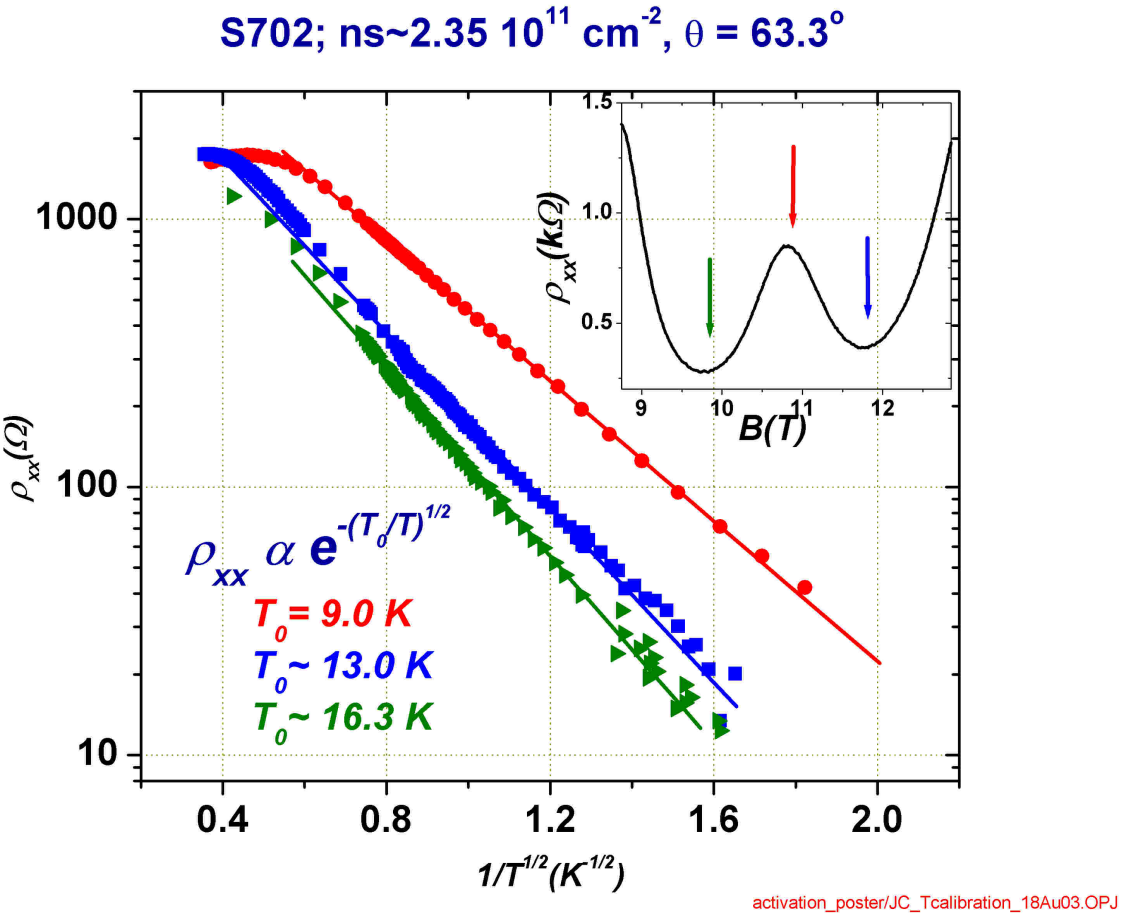

Figure 5.10: Activation energy data for ν = 2 QHF in S702. The lines are linear fit to experimental data. The inset shows the longitudinal resistance as a function of applied fields. The arrows indicate magnetic fields at which data were taken.

Angular evolution

In standard ferromagnets, the magnetization evolves with the application of an external magnetic field due to the increase in size of the magnetic domains with magnetic moment parallel to the external field. From the pseudospin analogy, and the presence of domains in quantum Hall ferromagnets, we expected that changing the effective magnetic field-the field responsible for the gap around the Fermi level-would produce a change in the domains and hence, be observed in the magnetoresistance data. It is important to keep in mind that the effective field is related to the actual magnetic field, but they are not exactly the same thing. Referring back to figure 5.1, at coincidence the effective field is zero but as we move away from coincidence we apply a non-zero effective field.

Sure enough, consistent with what has been observed in other QHFs, we noticed a shift of the resistance peak with increasing tilt angle. In our case this shift is consistently to higher filling factor (lower perpendicular magnetic field) with increasing tilt. Figures 5.11 and figure 5.12, representing data taken at temperatures where the resistance peaks were well-resolved show that the resistance peaks start as a shoulder in the vicinity of $\boldsymbol{\nu}$ = n+1/2, n=1 (for $\boldsymbol{\nu} = 2$), 2(for $\boldsymbol{\nu} = 3$) at low tilt angles and move towards higher filling factors. They eventually disappear in the resistance maximum at $\boldsymbol{\nu}$ = (n+1)+1/2.

Figure 5.13 shows in the $\boldsymbol{B_{perp}}$-$\boldsymbol{B_{total}}$ plane, the evolution of the resistance peaks in various samples from wafers S702 and S372. The linear relationship between the data points in the tilt angle range where level crossing is expected justifies the label coincidence line given to the linear fit [38]. In a single particle picture, the slope of the coincidence line must equal $\boldsymbol{1/2m^*g^*}$. Using $\boldsymbol{m^*}$=0.015 and $\boldsymbol{g^*}$=-51, the slope should be 0.382. The slope of the experimental coincidence line is $\sim$ 0.622 *i.e.* more than 1.5 times the non-interacting value. This enhancement of $\boldsymbol{m^*g^*}$ is consistent with stronger electron-electron interactions (exchange interactions) in samples exhibiting quantum Hall ferromagnetism.

The angular evolution of the resistance peaks in InSb-based QHFs is similar to that observed in many other material systems e.g. GaAs[40], Cd(Mn)Te [36], but is opposite to that reported in AlAs [16] where the resistance peaks moved to higher filling factors with increasing tilt.

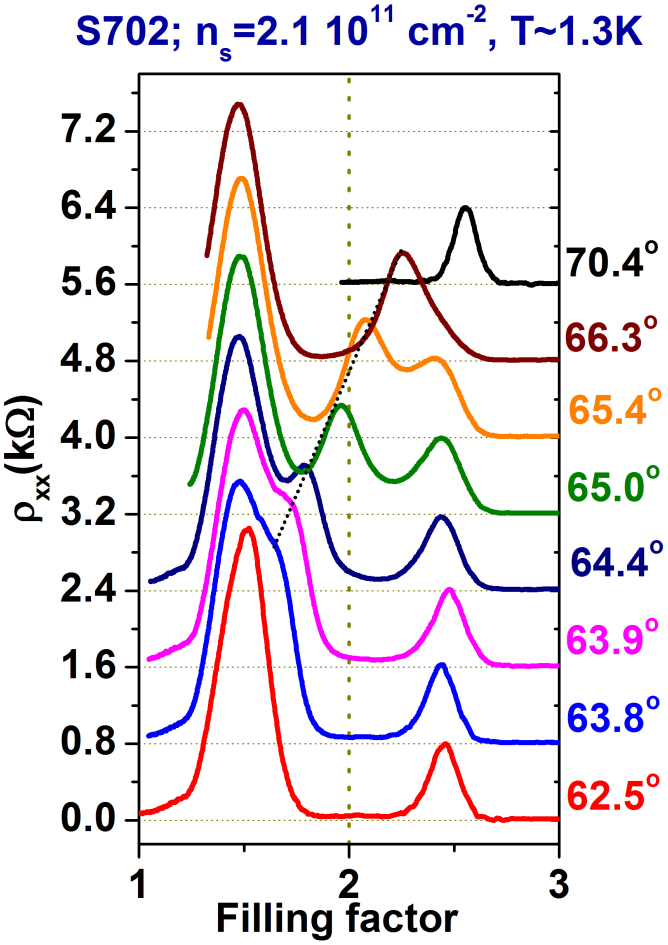

Figure 5.11: Angular evolution of the resistance peak in $\nu = 2$ QHF upon increasing tilt angle. The dotted lines are guides for the eyes.

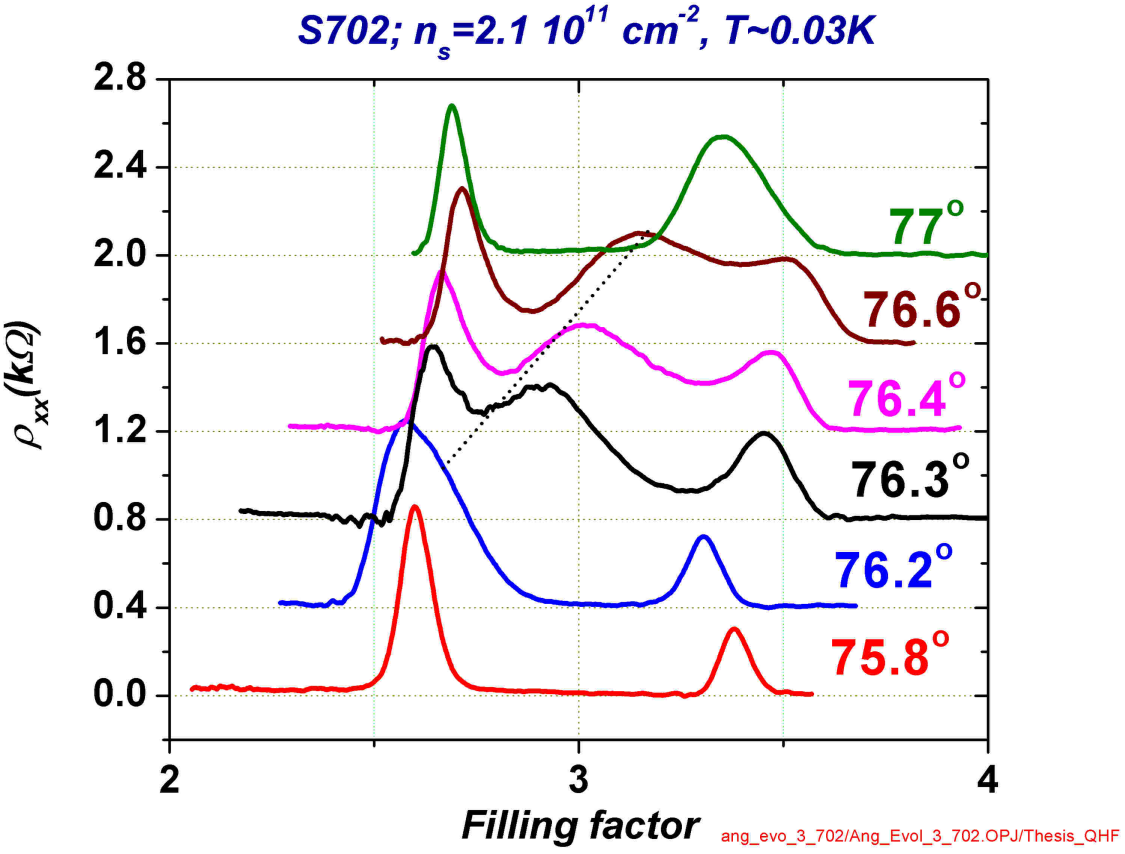

Figure 5.12: Angular evolution of the resistance peak in $\nu = 3$ QHF upon increasing tilt angle. The dotted lines are guides for the eyes.

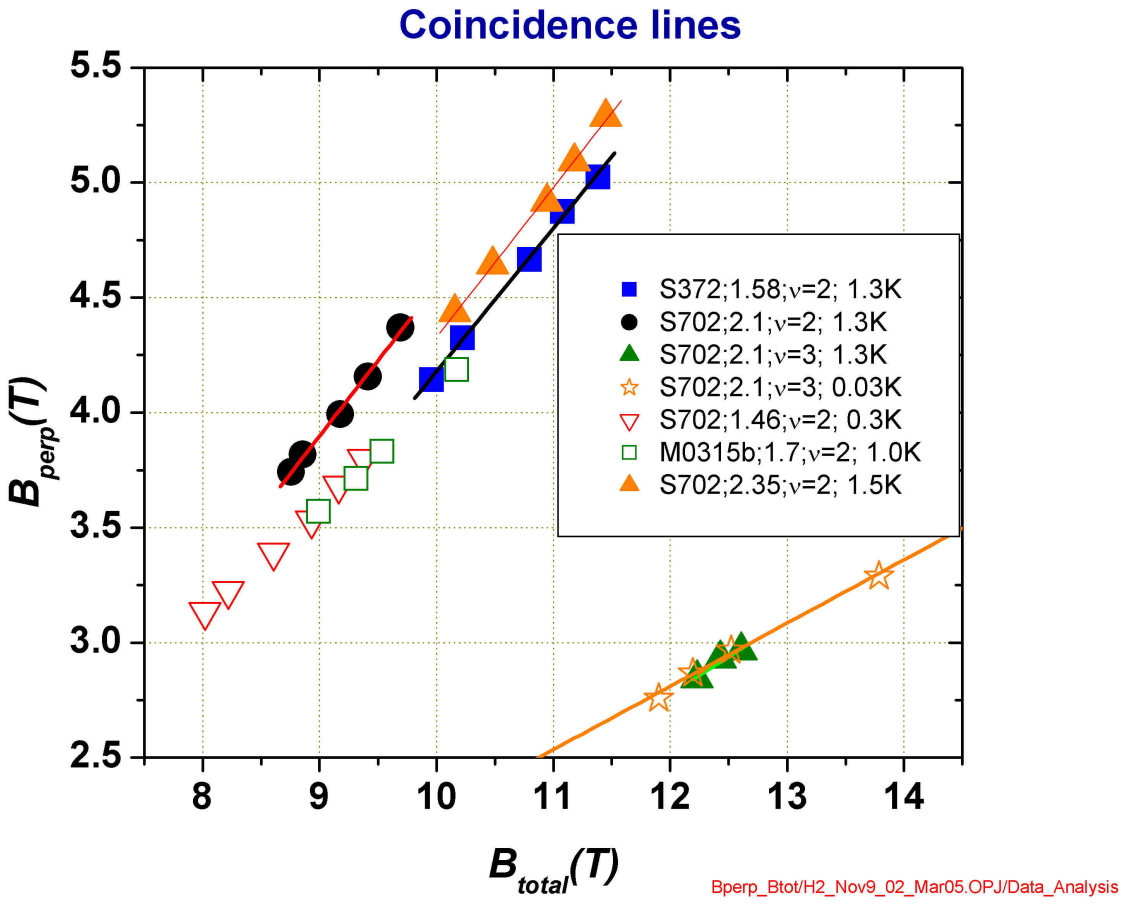

Figure 5.13: Resistance peaks motion in B_{perp}-B_{total} plane for various samples, mostly from wafers S702 and S372. In the legend, after the symbol, the name of the sample is given, followed by the sample density in units of $10^{11}\ cm^{-2}$, then the QHF state and finally, the temperature at which the data were taken. The lines are fits to the experimental data and represent the so-called coincidence lines.

Hysteresis

According to the theoretical classification of quantum Hall ferromagnets (QHF) in single layer 2DES, QHF states reported in this work are Ising-like since they originate from crossing between LLs from same electrical subband having different LL indices and opposite real spin orientations. They are therefore expected to exhibit hysteretic

behavior upon reversal of the magnetic field sweep direction. Figure 5.14 and figure 5.15 for the $\boldsymbol{\nu} = 2$ QHF show that sweeping the magnetic field up and then back down, introduced hysteresis loops in the magnetoresistance (MR) only within the QHF states. The down sweep data were shifted slightly in magnetic fields to account for the magnetic field lag between the up and down sweeps. The insets of figures 5.14 and 5.15 show the temperature variation between the up and down sweeps and suggest that temperature variation alone cannot account for the hysteretic behavior observed. Contrary to what was observed in AlAs [16]; the up magnetic field sweeps yield larger magnetoresistance than down field sweeps, there is no way to anticipate which field sweep direction will give the larger magnetoresistance in our samples.

Figure 5.16 shows the temperature effect on hysteretic features in $\boldsymbol{\nu} = 2$ QHF. Though for these particular data, the hysteresis loops are very small, they seem more pronounced at intermediate temperatures just as was reported by other research groups [16]. Figure 5.17 showing hysteretic features in $\boldsymbol{\nu} = 3$ QHF is still consistent with the general observation above as 100 mK for the $\boldsymbol{\nu} = 3$ QHF might be equivalent to a high temperature regime for the $\boldsymbol{\nu} = 2$ QHF due to the exchange interactions weakening with increasing filling factors.

An attempt to study hysteresis in our QHF under regulated temperatures gave some perplexing results. Figures 5.18 and 5.19 show data from same sample under very similar experimental conditions. The temperature was regulated by trying to keep the probe temperature (from a ruthenium oxide thermometer sitting very close to the sample) constant. Under good temperature regulation as in figure 5.18, strong hysteretic behavior was observed in the QHF. A repeat of the experiment after the system has warmed up to 1.7 K, see figure 5.19, did not duplicate the initial results. Two things happened during the latter run: the temperature regulation was not as good but most importantly, the probe temperature was higher. It is unfortunate that we could not have a better handle on the temperature during the experiments. The irreproducibility of the hysteresis could be due to the temperature difference.

Further attempts to observe strong hysteresis loops in this sample failed (see figures 5.20 and 5.21) either because we were not able to achieve as good temperature regulation as in figure 5.18 or the temperature and angles at which the data were taken were not appropriate. Because of the irreproducibility of the hysteresis despite our best efforts we cannot definitely state that hysteresis due to Ising QHF is present in our samples. It has been observed [16] that there is a direct relationship between the size of hysteresis loops and the tilt angle and the temperature at which data are

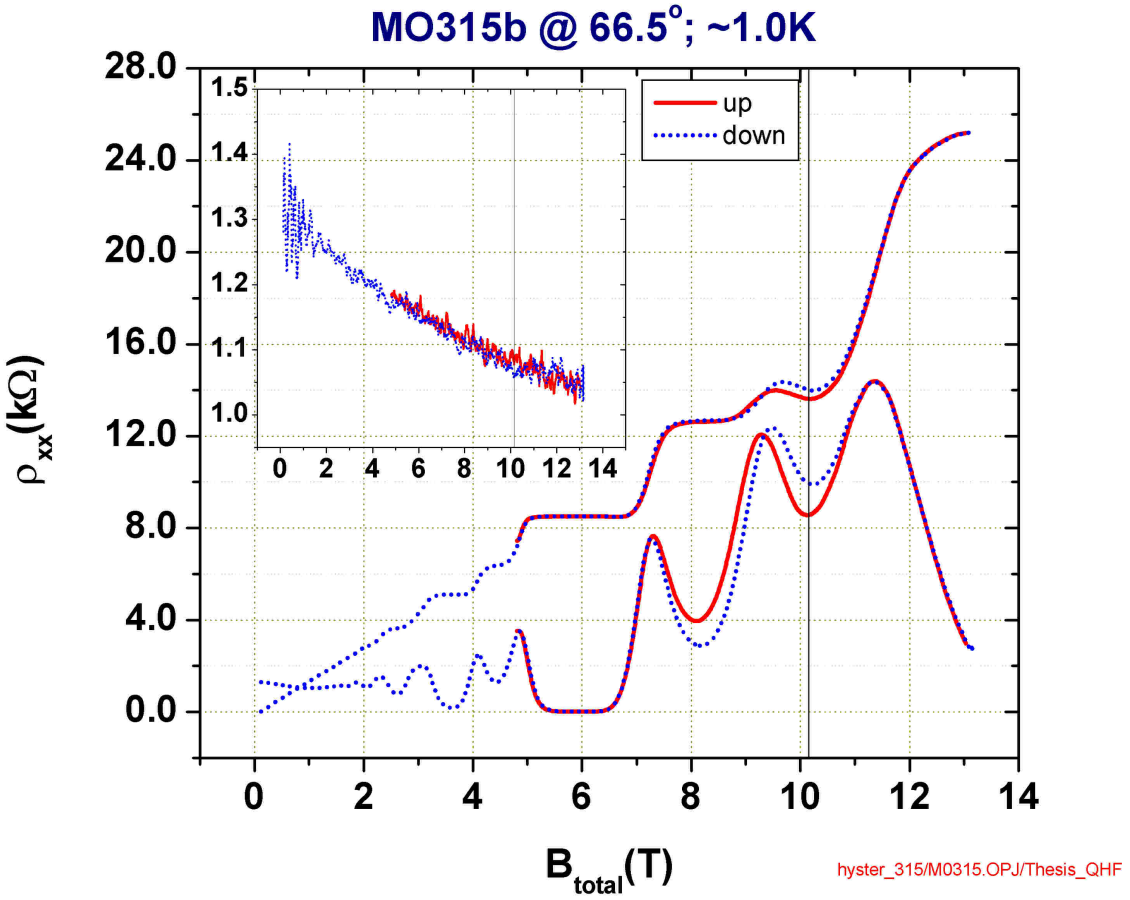

Figure 5.14: Hysteresis in the $\nu = 2$ QHF in sample M0315b at $\sim$ 1.0 K. full line is the up sweep trace and dotted line is the down sweep trace. The inset shows the variation of the temperature during field sweeps.

taken. The unpredictability of our data may come from our inability to tightly control these parameters during our experiments. At any rate, hysteretic behavior in QHF still requires further theoretical and experimental investigations as to date there is no consistent trend from materials to materials and even from samples to samples within the same material system. For example, while larger hysteresis loops were observed in AlAs-based QHF [16], no hysteresis whatsoever was seen in GaAs [37].

In QHF from the FQHE regime [41], very large hysteresis loops were observed

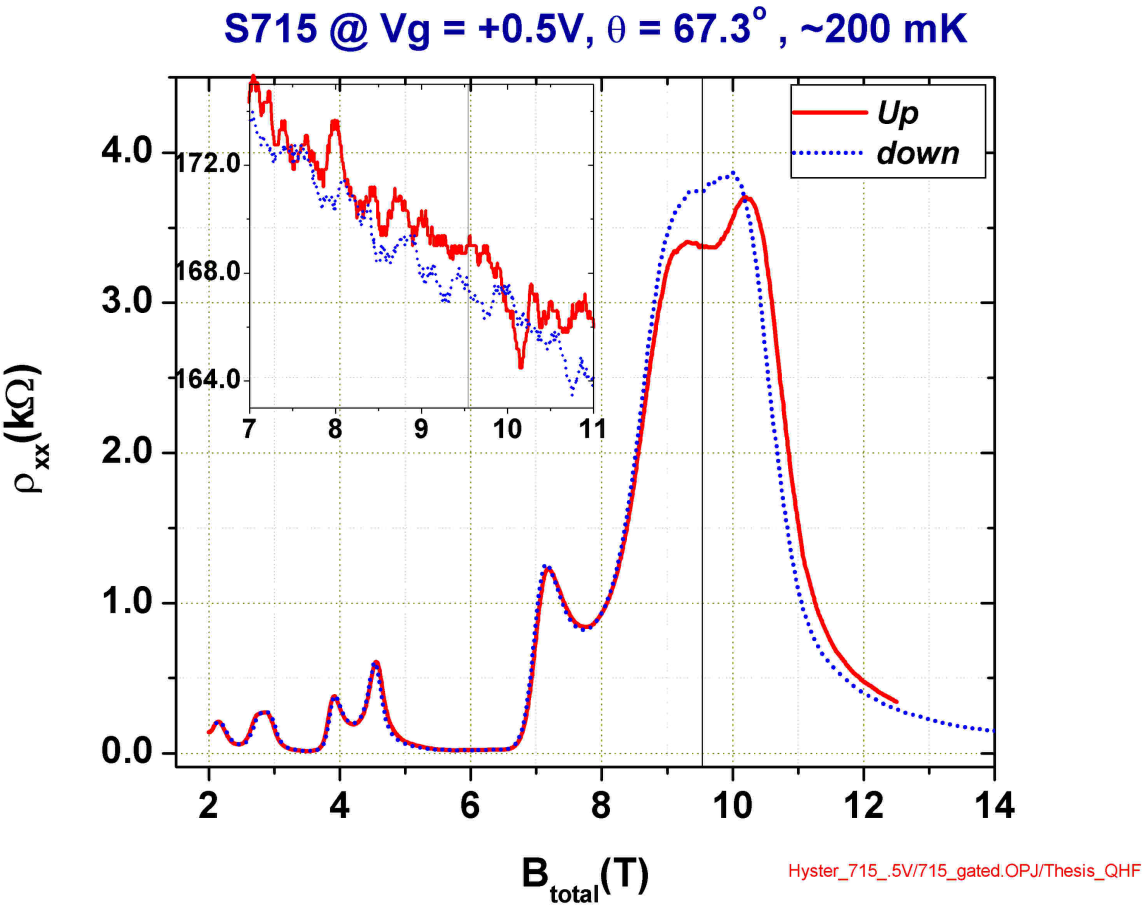

Figure 5.15: Hysteresis in the $\nu = 2$ QHF in sample S715 at $\sim$ 200 mK. full line is the up sweep trace and dotted line is the down sweep trace. The inset shows the variation of the temperature during field sweeps.

only when the field sweep rates were reduced to few milli Tesla per minute (mT/min). Disorder induced pinning of the pseudospin domains and/or the relatively fast sweep rates used in our work (>0.1 T/min) might be responsible for our tiny hysteresis loops and their irreproducibility. To fully investigate hysteresis would require more time at NHMFL and that we repeat these experiments at much slower field sweeps and under well-controlled thermal conditions over a very wide tilt angle-temperature-field sweep rate phase space.

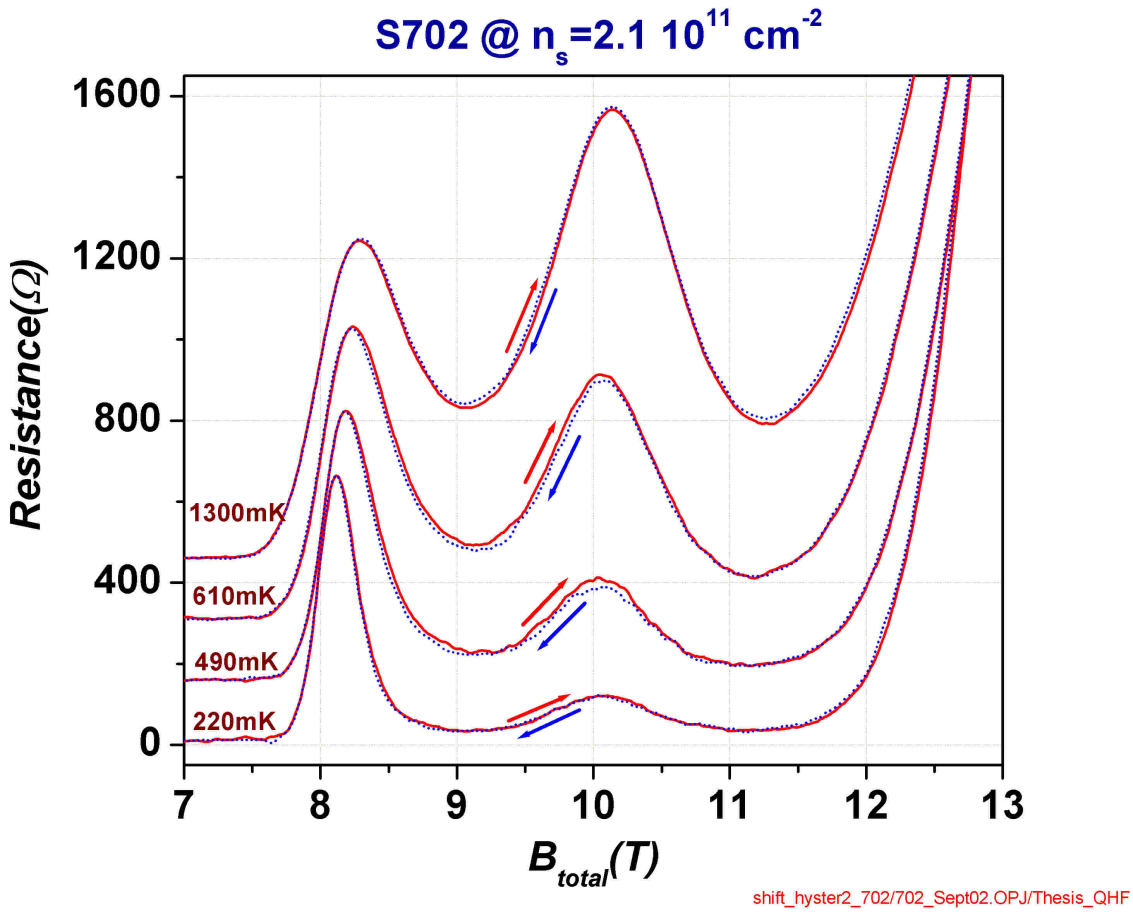

Figure 5.16: Temperature effect on hysteresis loops in the $\nu = 2$ QHF in sample S702. Full lines represent up sweep traces and dotted lines, down sweep traces. The sets of data are shifted vertically for clarity.

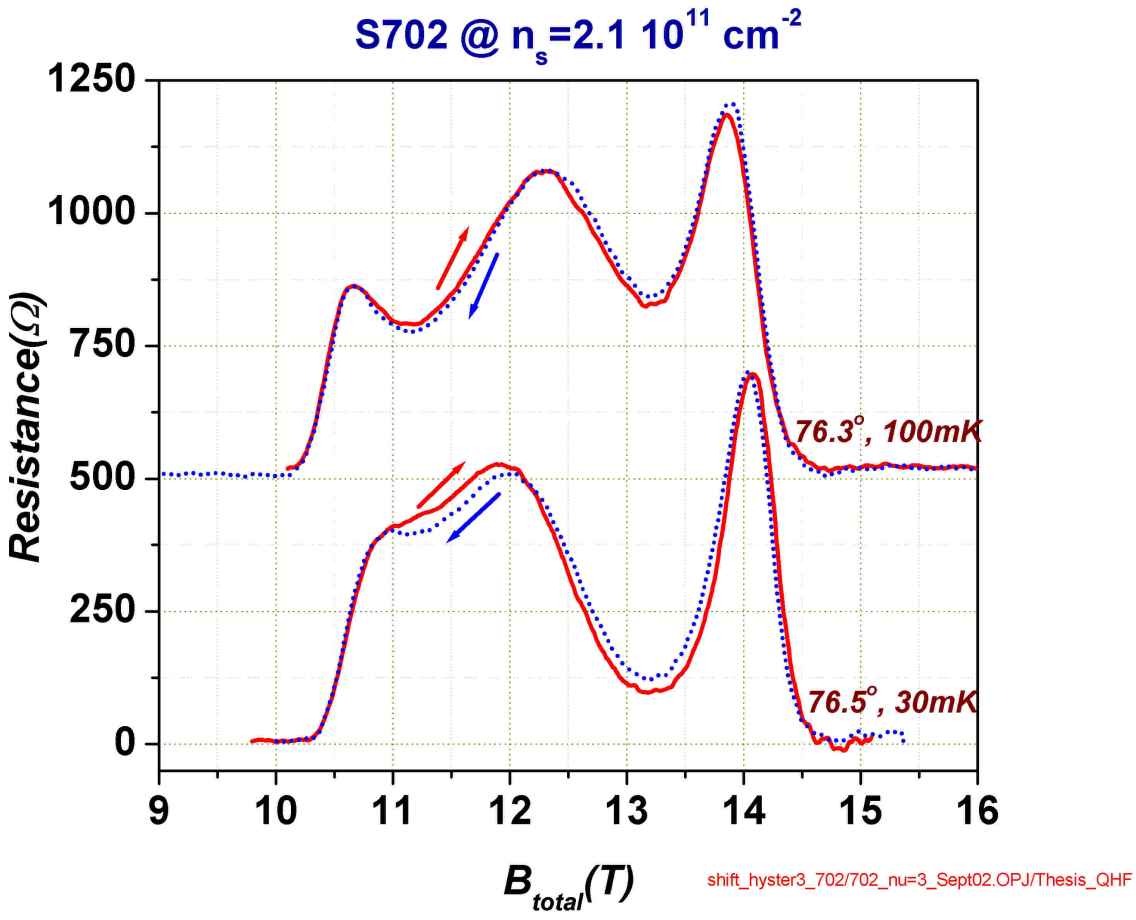

Figure 5.17: Hysteresis in the $\nu = 3$ QHF in sample S702 at 2 different tilt angles and temperatures. Full lines represent up sweep traces, and dotted lines, down sweep traces. Because the exchange energy is much smaller for the $\nu = 3$ QHF compared to the $\nu = 2$ QHF, 100 mK is in the high temperature regime, hence the smaller hysteresis loops. The 2 sets of data are shifted vertically for clarity.

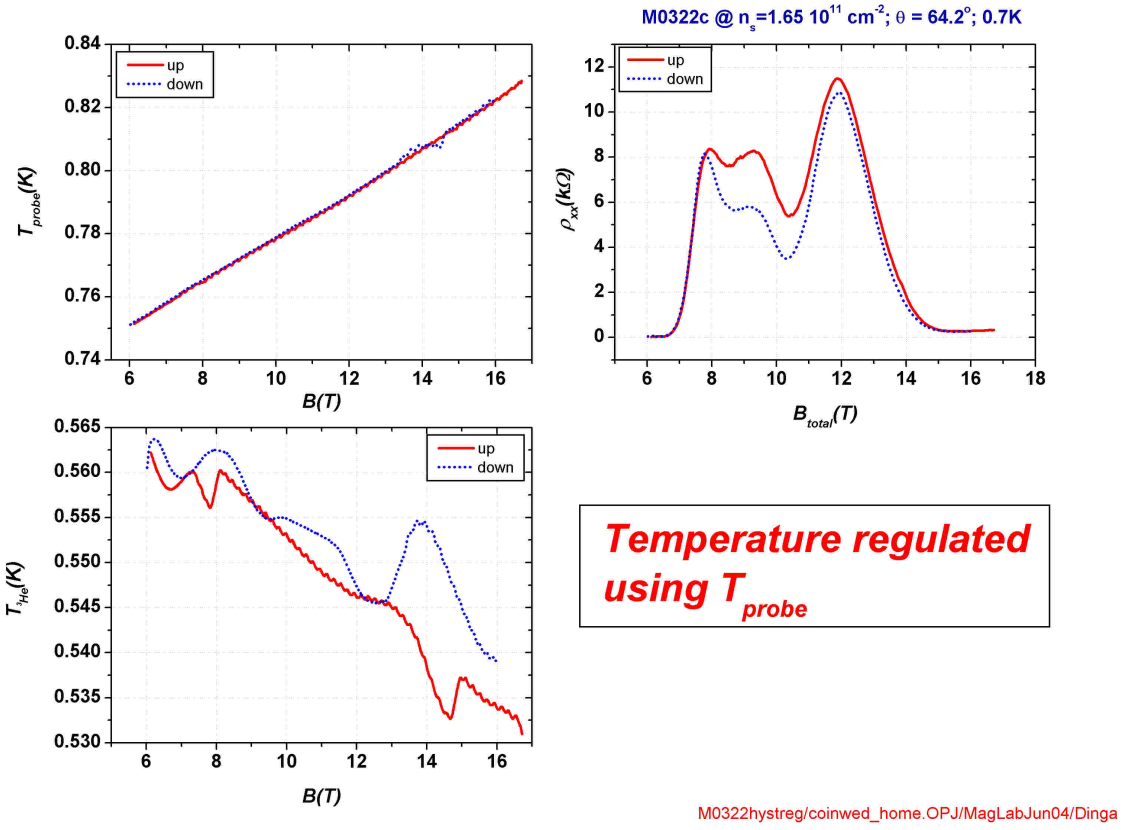

Figure 5.18: Hysteresis study in $\boldsymbol{\nu} = 2$ QHF in sample M0322c ($\boldsymbol{n_s} = 1.65\text{x}\mathbf{10^{11}}$ $\boldsymbol{cm^{-2}}$, $\boldsymbol{\theta} = \mathbf{64.2^o}$) at T $\sim$ 0.7K. The upper left panel shows the probe temperature during the run, the upper right panel the magnetoresistance data, and the bottom left panel, the ^{3}He temperature. Note the good probe temperature regulation and the huge hysteresis loop within the QHF.

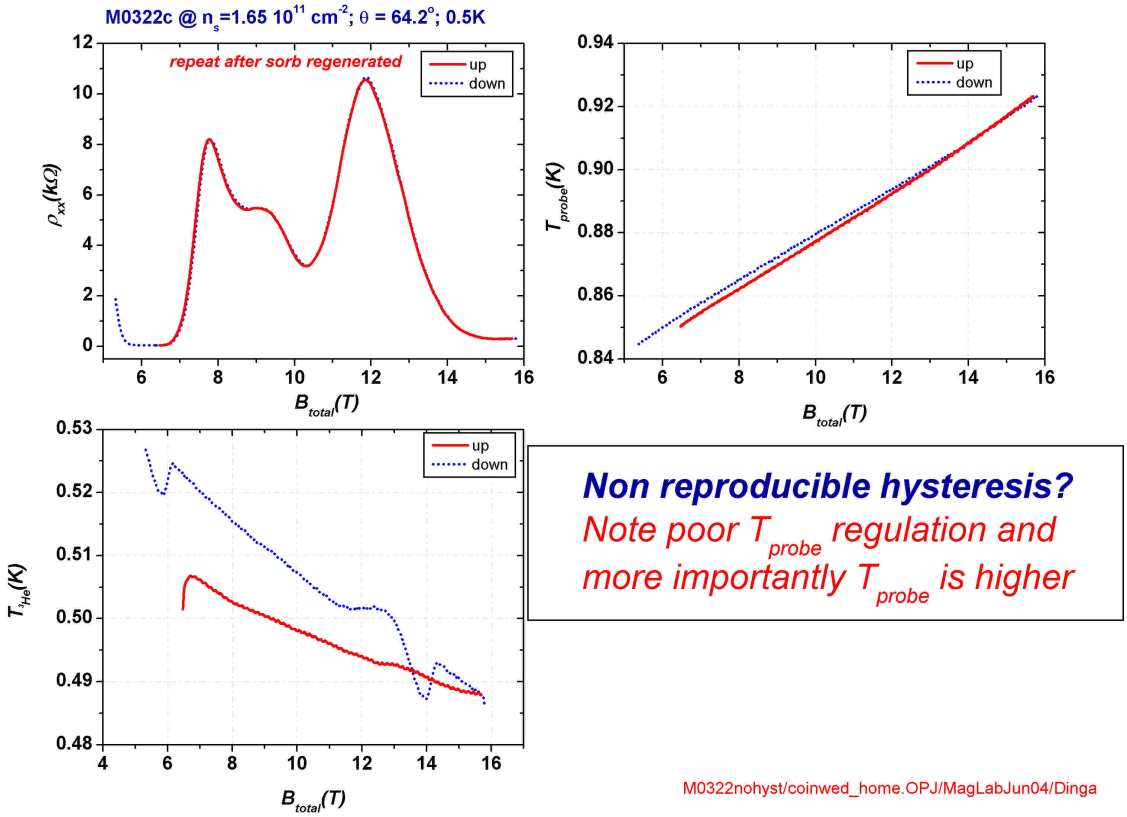

Figure 5.19: Repeat of the run with data shown in figure 5.18. No hysteresis found in the magnetoresistance data shown in the upper left panel. The upper right panel shows the probe temperature while the bottom left panel shows the ^{3}He temperature during the run. Note however, the probe temperature was higher and the temperature regulation was not as good.

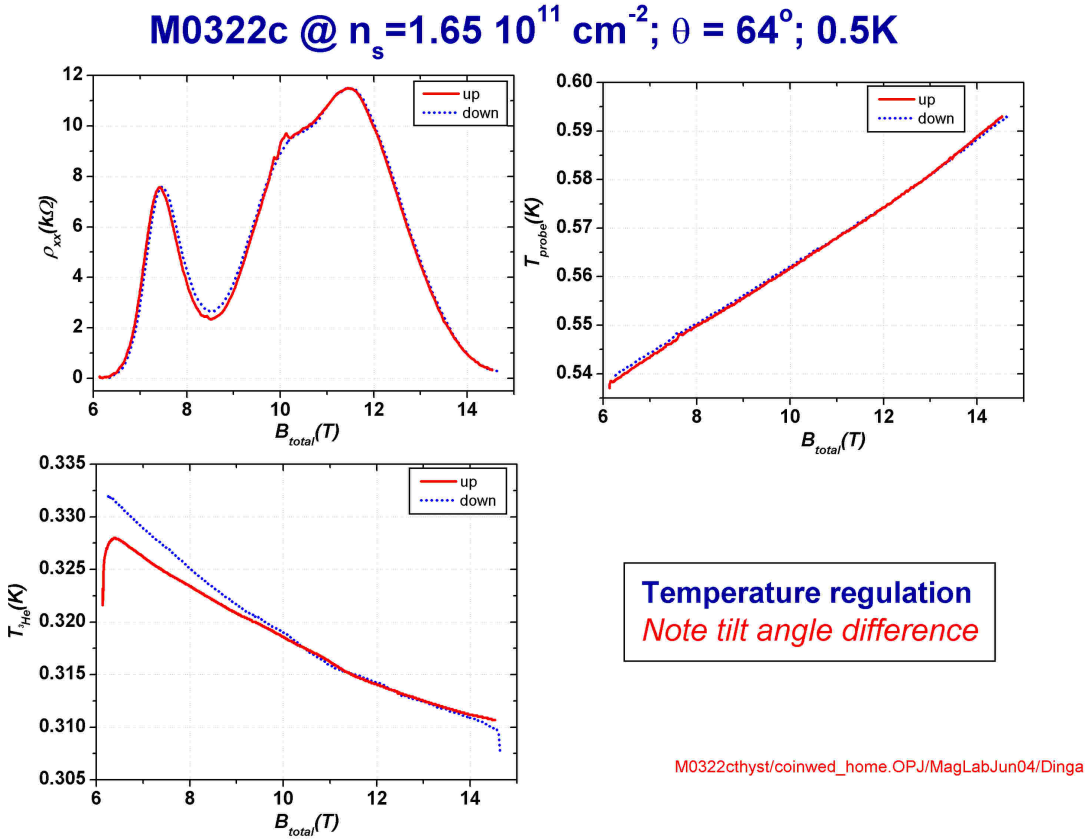

Figure 5.20: No hysteresis found in M0322c ($\boldsymbol{n_s}$ = 1.65x$\mathbf{10^{11}}$ $\boldsymbol{cm^{-2}}$, $\boldsymbol{\theta}$ = $\mathbf{64.0^o}$) at T $\sim$ 0.5K. The magnetoresistance data is shown in the upper left panel. The upper right panel shows the probe temperature while the bottom left panel shows the 3He temperature during the run. Note however, the tilt angle difference and the relatively good temperature regulation.

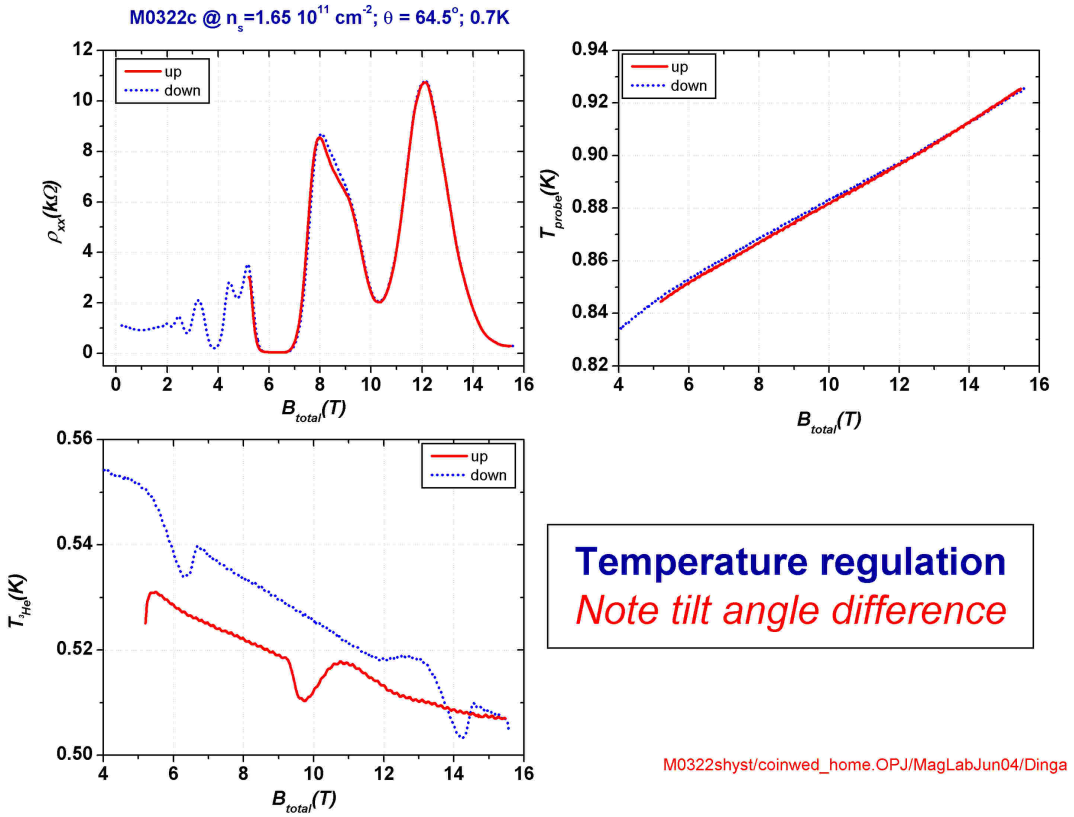

Figure 5.21: No hysteresis found in M0322c ($\boldsymbol{n_s}$ = 1.65x$\mathbf{10^{11}}$ $\boldsymbol{cm^{-2}}$, $\boldsymbol{\theta}$ = $\mathbf{64.5^o}$) at T $\sim$ 0.7K.The magnetoresistance data is shown in the upper left panel. The upper right panel shows the probe temperature while the bottom left panel shows the ^{3}He temperature during the run. Note the tilt angle difference and the not so good temperature regulation.

Anisotropy

Because observed QHF are from the Ising class of ferromagnets, they are expected to possess easy-axis anisotropy. But contrary to standard ferromagnets where the easy axis is defined with respect to crystallographic axes of the substrate, the easy-axis in QHF is defined with respect to the orientation of the in-plane component of the applied magnetic field. The reason being, quantum Hall ferromagnets are magnetic-

field induced ferromagnets. For our anisotropy study, we used spider patterned mesa structures. Upon tilting the sample, the direction of the in-plane field is easily determined and the magnetoresistance data were collected with the probing current running parallel (I para $\boldsymbol{B_{ip}}$), diagonal (I diag $\boldsymbol{B_{ip}}$) or perpendicular (I perp $\boldsymbol{B_{ip}}$) to the in-plane magnetic field. Because we were not using the same contact pads for all the configurations, in any real sample these measurements always give different resistance values. Differences in resistance values that are due to inherent anisotropy in the sample (from dislocations, roughness etc.) and/or contact leads should be independent on the strength of the applied magnetic field, thus allowing a collapse of magnetoresistance curves from various configurations to one curve using appropriate scaling factors, leaving differences arising from the orientation of the pseudospin domains to show up only within the QHF states.

For this work, we performed anisotropy studies over magnetic field ranges covering the QHF state of interest and its closest neighbor QHE states. We observed that in some samples, we could force the curves to collapse onto a single curve except within the QHF, indicating anisotropic transport in the quantum Hall ferromagnet. The ideal setup for this study would be a two-axis tilter allowing to go from one configuration say I para $\boldsymbol{B_{ip}}$, to the other, say I perp $\boldsymbol{B_{ip}}$, by rotating the sample by 90 degrees and keeping the same current and voltage leads. Doing so, will clearly show anisotropy (if there is any) without the need to scale the data.

Figures 5.22 and 5.23 show the longitudinal resistance data as function of the applied magnetic field under various conditions before and after scaling. The scaled data show that the configuration where the current runs perpendicular to the in-plane field is the least resistive while the configuration with the current parallel to the in-plane field is the most resistive. The same trend is observed in a sample from a different wafer shown in figure 5.24. For this sample no scaling was needed. Not all samples however displayed this anisotropy. In some samples the inherent anisotropy present due to growth swamped any QHF anisotropy. In these samples a single scaling

factor could not be found to force the two curves for low tilt atop one another.

Our data on anisotropy are consistent with the formation of unidirectional pseudospin domains oriented perpendicular to the in-plane field (see figure 5.25 below). Running the current parallel to the in-plane field, results in enhanced scattering as the electrons cross barriers introduced on their path by the domains, but when the current runs perpendicular to the in-plane field, the carriers move along paths of least resistance in the stripe-like domains. The current diagonal to the in-plane field leads to resistance values intermediate between the two previous configurations.

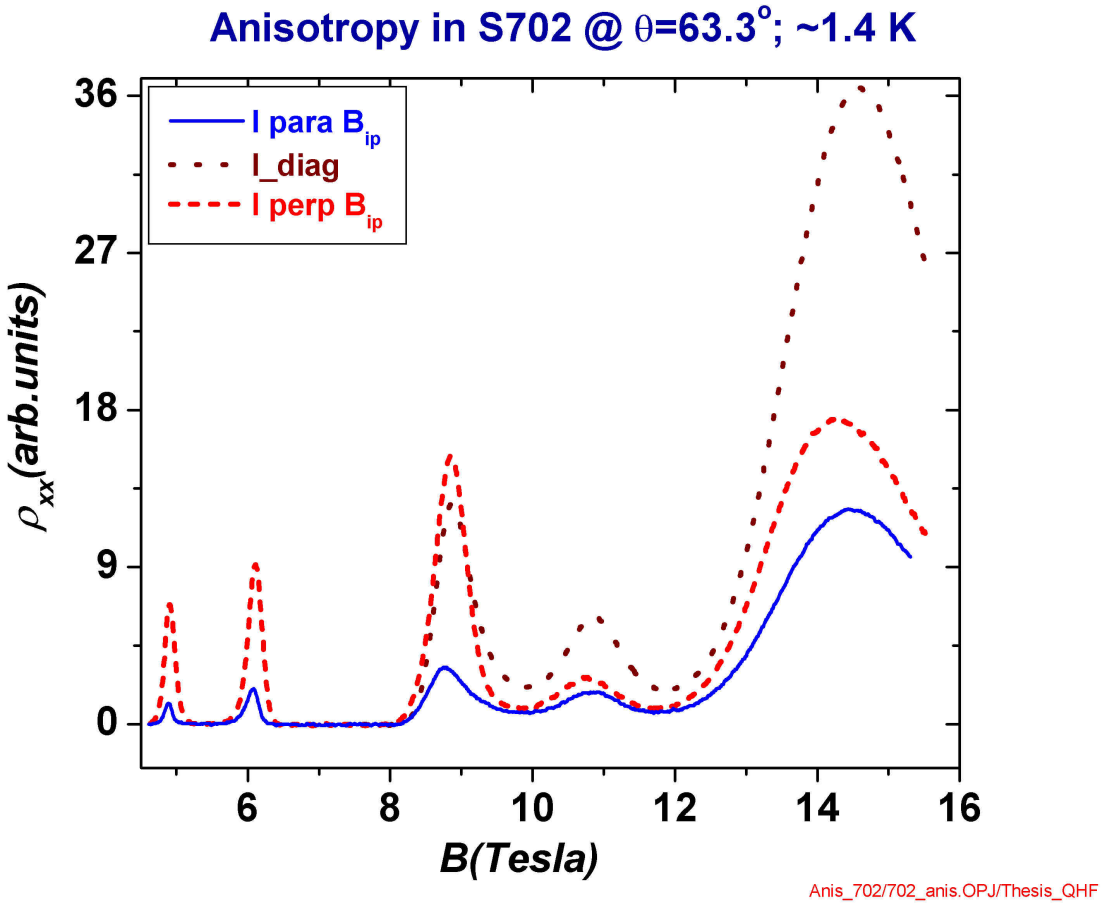

Figure 5.22: Raw data on anisotropy study in the $\nu = 2$ QHF in S702. Without scaling nothing could be said about differences observed in the QHF.

These findings are strikingly similar to those reported in integer QHE states in Si/SiGe heterostructures [42], and in very clean GaAs quantum wells [43] at half filling of the spin split level of the n = 1 LL, where the initially "isotropic" $\boldsymbol{\nu} = 5/2$ and 7/2 FQHE states became anisotropic with increasing in-plane fields. The quotes on isotropic is to say that a scaling factor was needed to cause the curves to collapse onto a single curve.

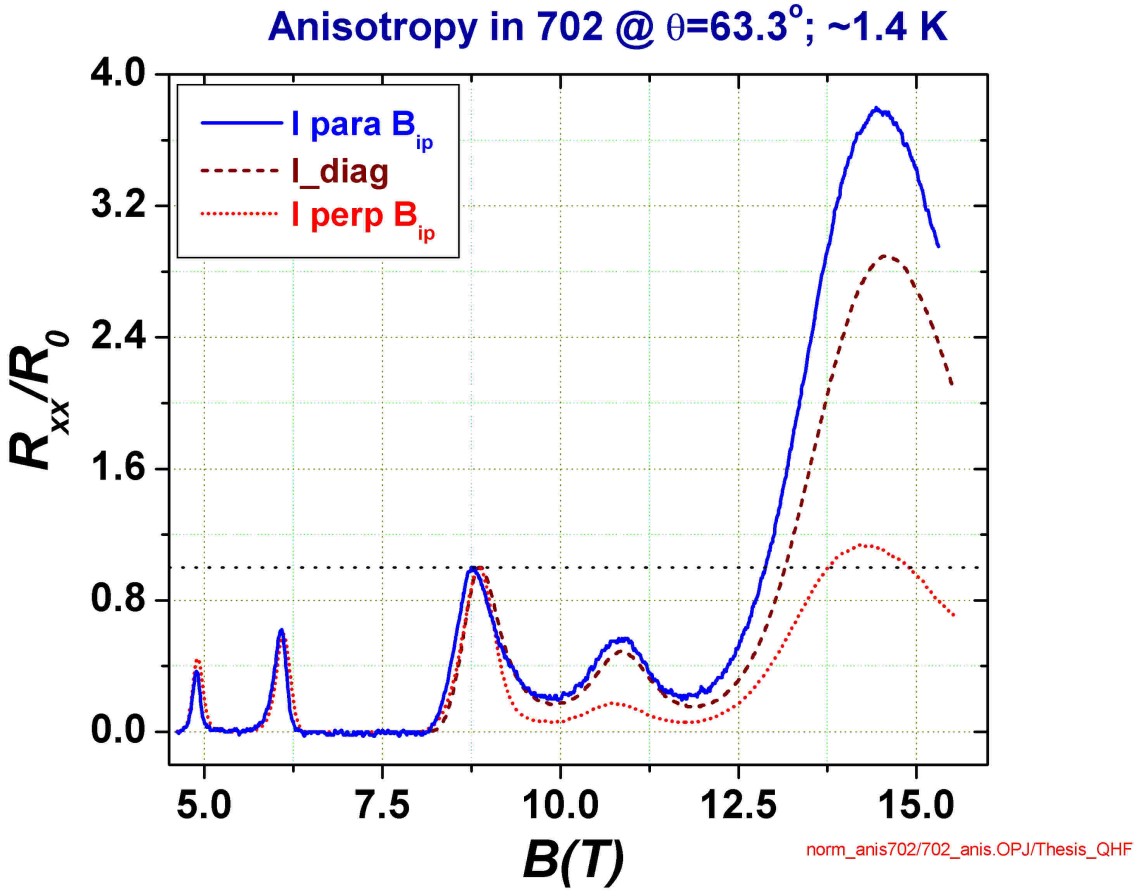

Figure 5.23: Same data from figure 5.22 after scaling the resistances. The longitudinal resistance was normalized with respect to the resistance value corresponding to filling factor 2.5 (dotted horizontal line). The scaling helped visualize that the system is less resistive when the current runs perpendicular to the in-plane field.

Anisotropic transport is inconsistent with a uniform electron state. Other possible causes of anisotropy such as density inhomogeneity in the starting wafer, anisotropic distribution of dislocations in the samples, or vicinal surfaces from slight miscut of (001) GaAs substrate were all ruled out because: density variation from one configuration to the other was usually less than **0.5%**, and any structural anisotropy or unforeseen order of the static disorder would have led to anisotropic behavior at all QHE states. A possible cause of anisotropy in an otherwise uniform 2DES under

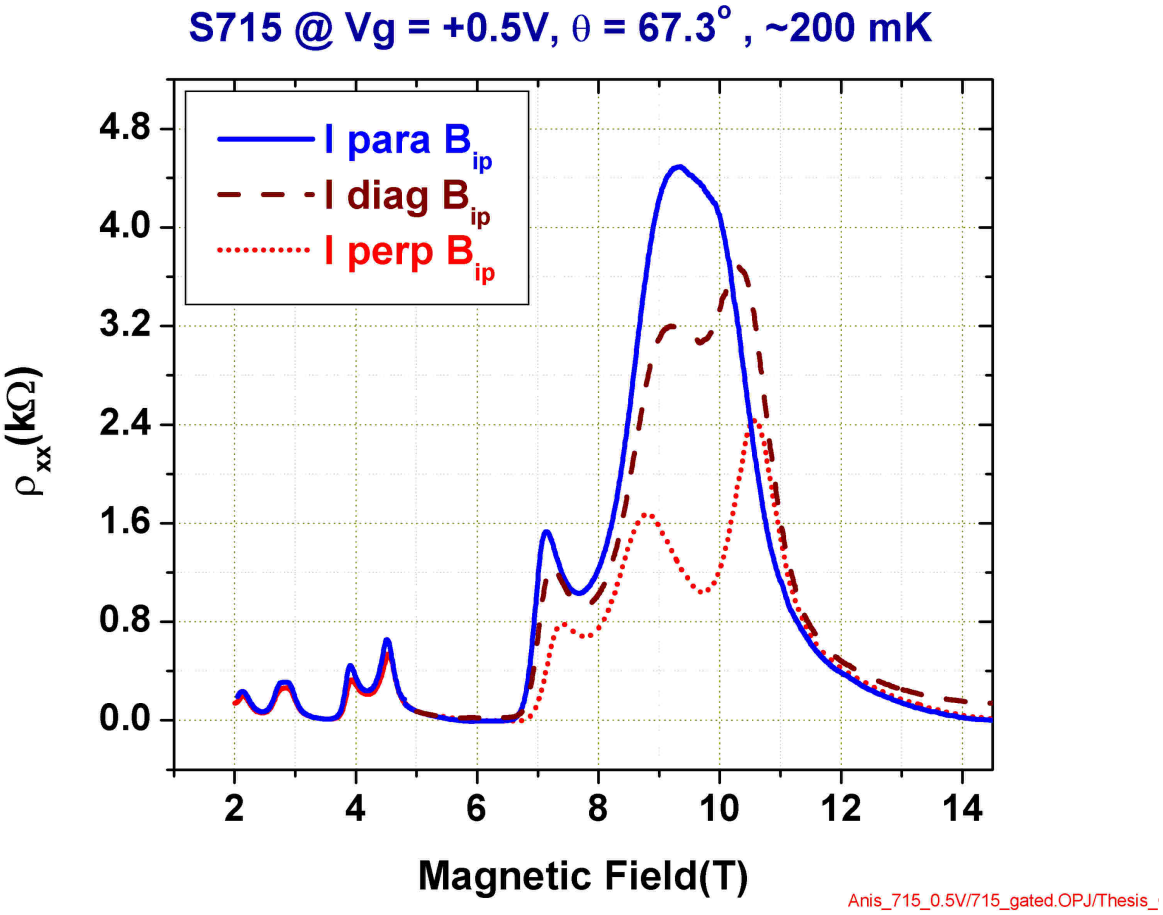

Figure 5.24: Anisotropy in $\nu = 2$ QHF in S715. The system is less resistive when the current runs perpendicular to the in-plane magnetic field. No scaling was used for these data.

tilted magnetic fields, is the instability introduced by charge density wave (CDW) formation as proposed by Koulakov, Fogler and Shklovkii [44] and Moessner and Chalker [45]. They suggested that when the magnetic field is sufficiently low but not so low that disorder destroys the cyclotron gap, periodic stripe or bubble phases, with spatial periodicity of close to three cyclotron radii, were more energetically favorable. The dominant phase being dictated by how filled is the top LL. The bubble phase was found to occur mostly at very low filling ($\nu_{top} < 0.3$) while stripe pattern won at higher filling ($\nu_{top} > 0.3$). In the QHF, the energy gap around the Fermi level reaches its minimum value. This can be thought of as being the condition where the effective magnetic field is sufficiently low but not so low as to destroy the gap. The ground state in QHF more likely might have the top LL filled enough to cause stripe pattern formation.

We note however that in samples used for anisotropy studies, at zero tilt there was a crossing of magnetoresistance traces at low fields *i.e.*, the configuration giving initially the larger resistance values became the least resistive at certain magnetic fields. Figure 5.26 shows low fields data for sample S702. To match the curves as shown, the resistance from the configuration with the current running parallel to

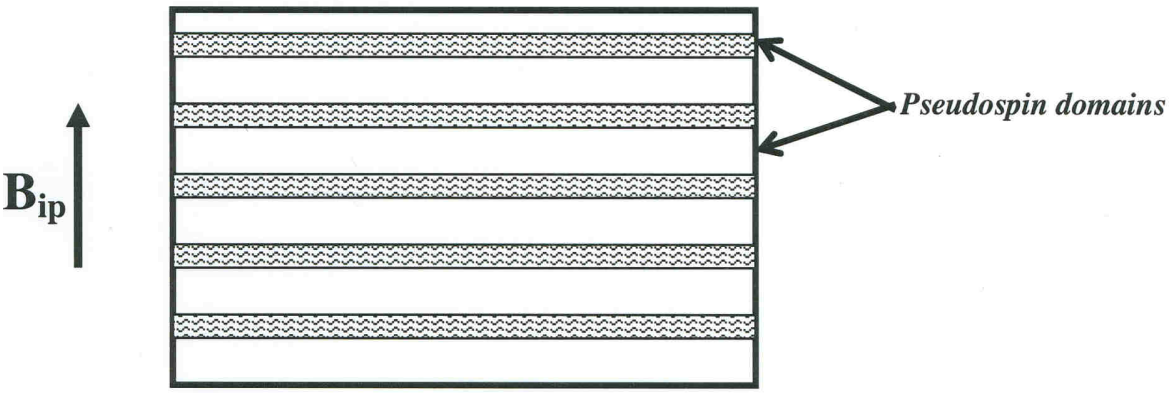

Figure 5.25: Schematic of possible pseudospin domains orientation in InSb-based QHFs. The domains are stripes perpendicular to the in-plane magnetic field.

the in plane field was multiplied by 4.4. This unexpected behavior might cast some shadow on our conclusions on anisotropy but we think comparing what was happening in the QHF to that in the closest QHE states was appropriate.

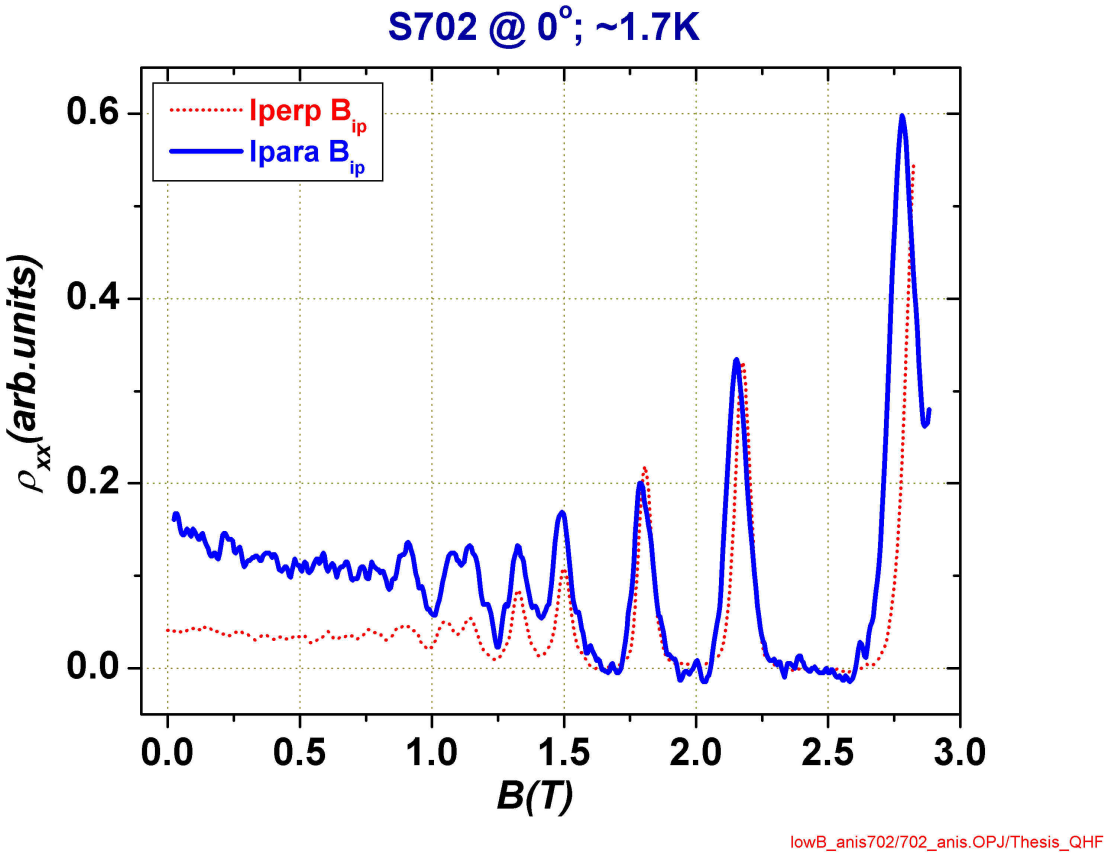

Figure 5.26: Low magnetic fields data for anisotropy studies in sample S702 ($\boldsymbol{n_s}$=2.1x$\mathbf{10^{11}}$ $\boldsymbol{cm^{-2}}$) at 1.7 K. Data from Ipara $\boldsymbol{B_{ip}}$ configuration was multiplied by $\sim$ 4.4 in an attempt to force the two curves to collapse onto a single curve. Note that the two traces cross at $\sim$ 1.7 T making any attempt to have the two traces collapsing onto a single curve impossible.

Density effect

Having noticed that well resolved quantum Hall ferromagnetic states were found only in high density samples ($\boldsymbol{n_s} > 1.3\text{x}\mathbf{10^{11}}\ \boldsymbol{cm^{-2}}$) regardless of the electron mobility, we were interested in seeing if starting with high density sample showing QHF, we could cause the state to disappear only by reducing the carrier density. Our finding is summarized on figure 5.27. As we reduced the density with the sample held at a constant temperature of 0.3 K, the initially strong QHF gradually weakened and eventually disappeared around the density threshold mark of $\sim 1.3\text{x}\mathbf{10^{11}}\ \boldsymbol{cm^{-2}}$. From there on, the persistent resistance minimum turned into a resistance maximum at coincidence angle. Interestingly, the plot of the coincidence angle for the degeneracy between the n = 0 and n = 1 LLs as a function of the carrier density (see figure 5.28) shows that below the threshold density, the coincidence angle is fairly independent of the carrier density. At higher densities however, the coincidence angle value is reduced as the density is increased. These results are consistent with a single particle behavior at sub-threshold densities and an enhanced many-body effects at larger carrier densities. Figure 5.29 showing the density dependence of the characteristic temperature ($\boldsymbol{T_0}$) extracted from the activation energy data taken at the resistance peak, also corroborated the idea of increasing many-body interactions with increasing density. In fact, the increase of $\boldsymbol{T_0}$ with increasing density means a reduction of the localization length, hence longer coherence length in the electronic system.The location of data points from sample S697 at much lower $\boldsymbol{T_0}$ value for a given carrier density is consistent with a longer localization length hence more disordered system.

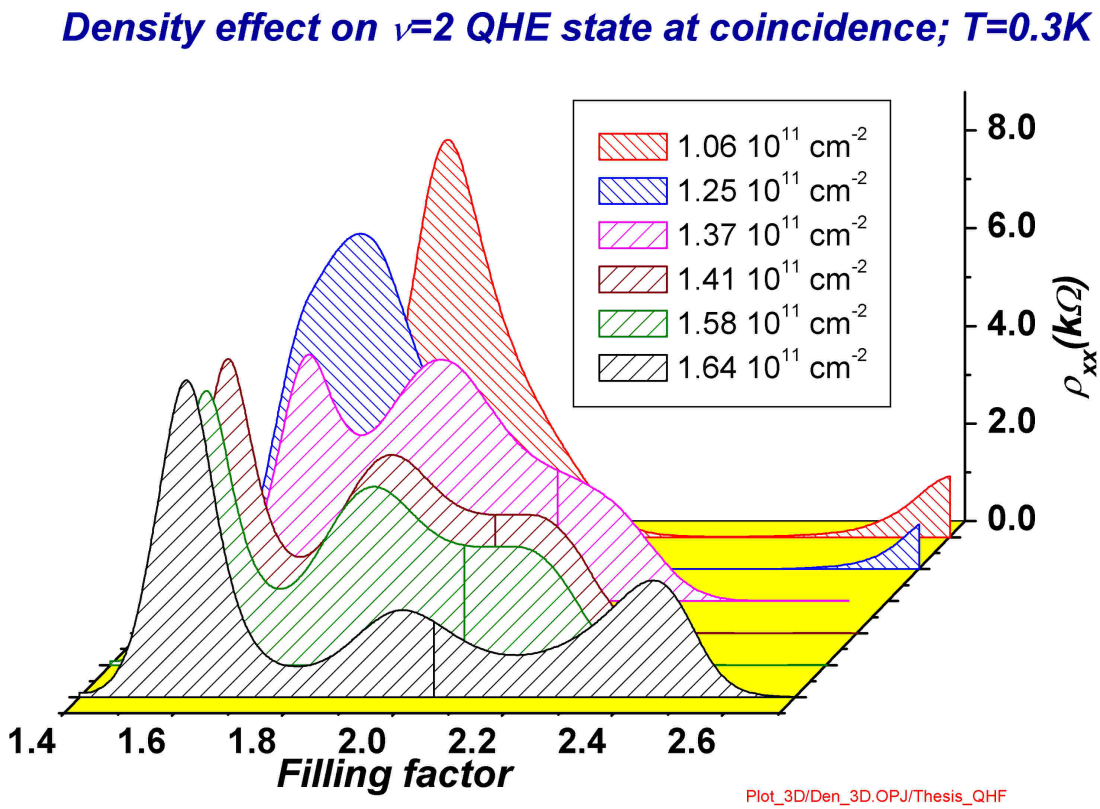

Figure 5.27: Density effect on the persistent resistance minimum in the $\boldsymbol{\nu} = 2$ QHE state. The sample (S702) was held at a constant temperature of 0.3 K and the density changed using gate bias.

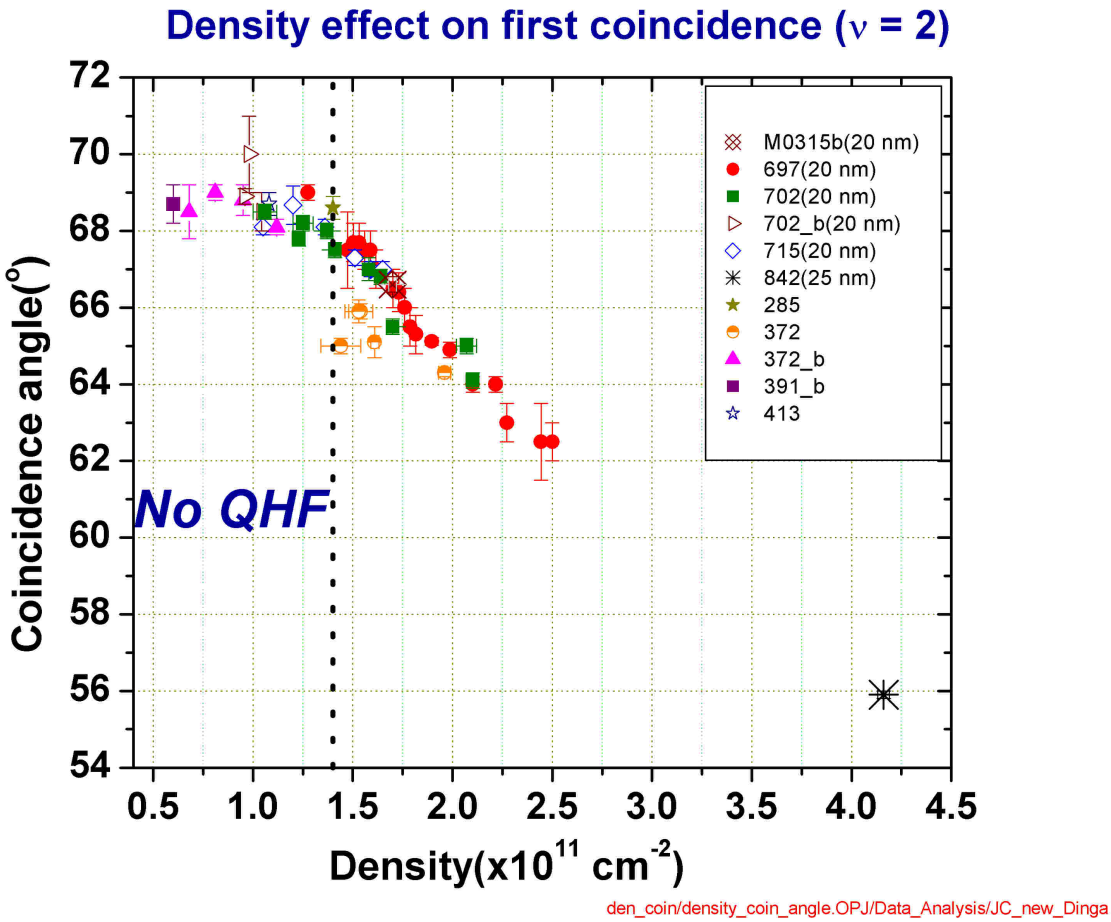

Figure 5.28: Density effect on the first coincidence angle ($\boldsymbol{\nu} = 2$) for all the samples investigated. The dotted vertical line corresponds to the threshold density for the emergence of QHF. In the legend, the number in parentheses corresponds to the QW width; no indication means the well width was 30 nm.

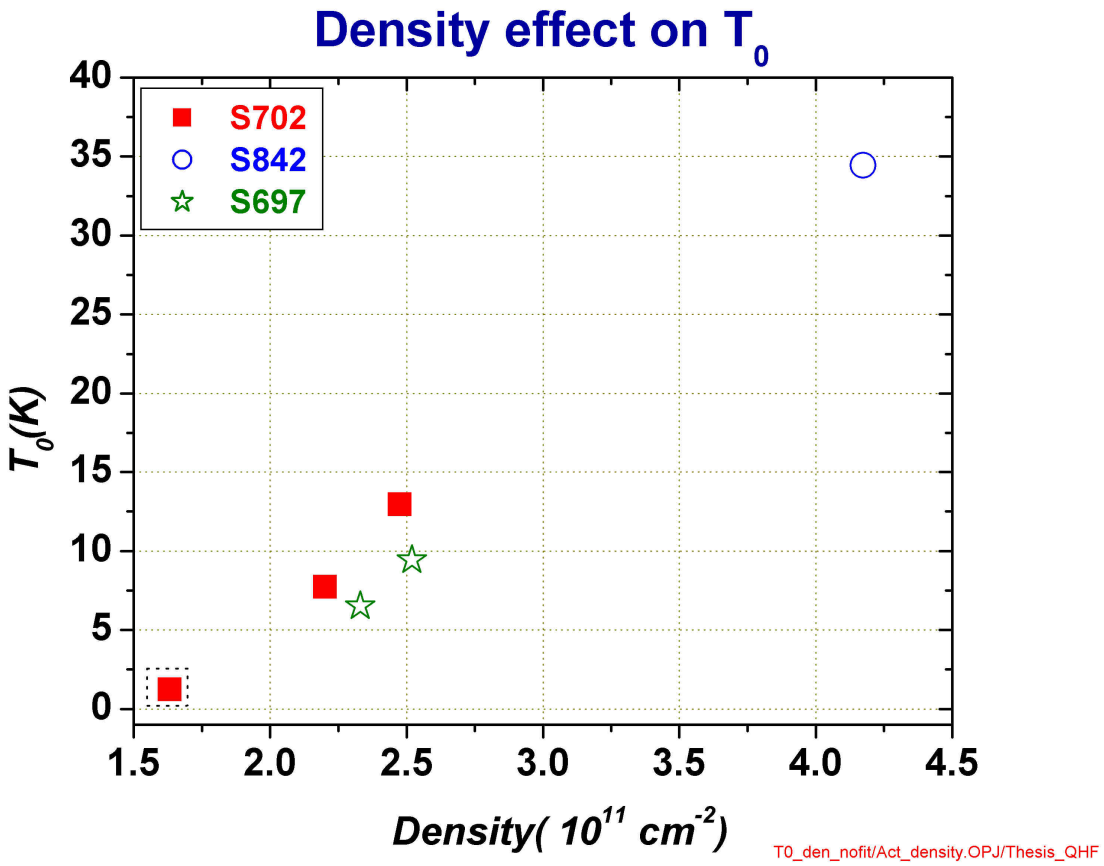

Figure 5.29: Density effect on the characteristic temperature T_0. The data point in the box is questionable because the resistance change was less than a decade in the activation data. There is undoubtedly a monotonic increase of T_0 with increasing densities.

Dirty quantum Hall ferromagnets

In common QHFs, the resistance peak arising in the persistent QHE state, has a characteristic behavior under tilting and temperature change. With increase tilt, the resistance peak consistently moves in one direction within the QHE state, leading to the so-called coincidence line. Changing the temperature at fixed tilt angle leads to growth of the resistance feature without significant change in the line shape of the magnetoresistance. The magnetoresistance line shape at a given tilt angle is

determined mostly by the temperature, since it is the temperature that determines the size and density of the pseudospin domains. The position of the resistance peak within the QHE state for a given temperature is determined by the tilt angle.

Figure 5.30 shows the angular evolution of the $\boldsymbol{\nu} = 3$ QHF in sample S697 at a fixed temperature of $\sim$1 K. Upon increasing tilt, the resistance peak barely moves while the line shape of the magnetoresistance changes dramatically. The high field valley looks as if tilting caused thermal activation in the sample. Such a large change in magnetoresistance could not be accounted for by possible temperature fluctuations. Stranger results are observed in the temperature dependence of the magnetoresistance at fixed tilt angle for QHF states in this sample. The data shown on figure 5.31 revealed a double-peak structure with the peaks moving in opposite directions when the temperature is increased.

These data are consistent with dirty QHF where defects and/or impurities can pin down the domains and/or create complex multi-domain structures. In such systems, high temperatures can unpin the domains, hence the shift of the peak position with temperature, while multi-peak may originate from various type of domain walls. Why the two peaks move in opposite directions is an interesting question requiring further investigation.

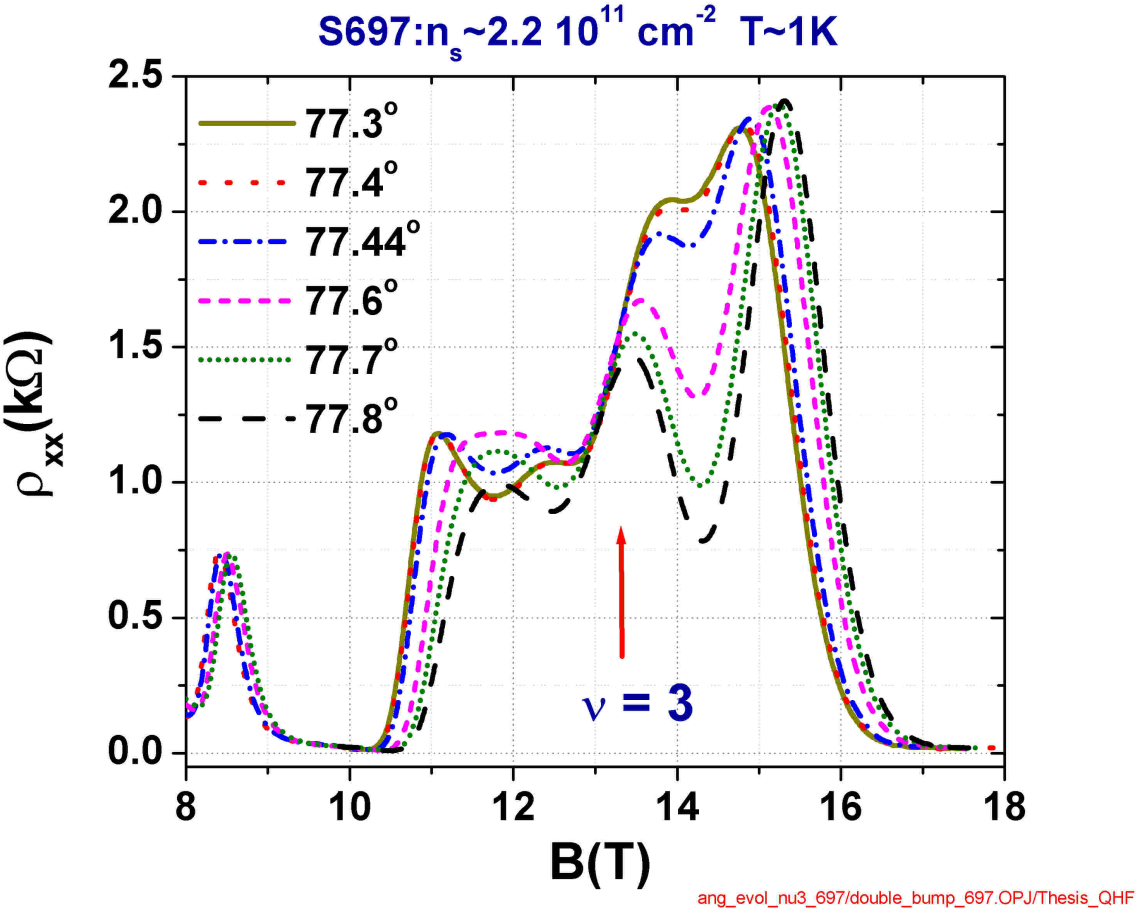

Figure 5.30: Angular evolution of the ν=3 QHF in S697 at a fixed density of 2.2x$\mathbf{10^{11}}$ $\boldsymbol{cm^{-2}}$ and a temperature of $\sim$1 K. The resistance peak barely moves while the high field valley deepens with increasing tilt.

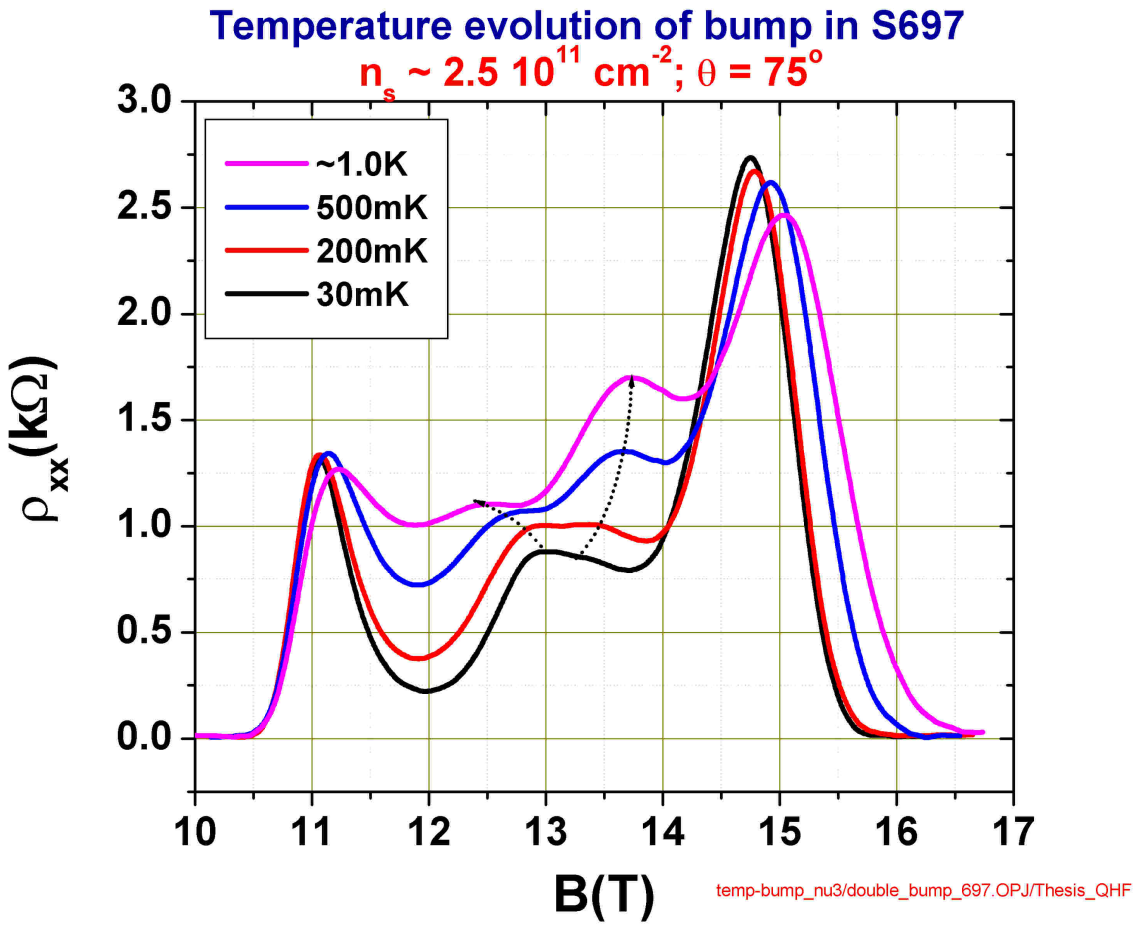

Figure 5.31: Temperature evolution of the $\nu = 3$ QHF at a fixed density of 2.5x$\mathbf{10^{11}}$ $\boldsymbol{cm^{-2}}$ and tilt angle of $\mathbf{75^o}$. Note the two peaks moving to opposite directions. The arrows are guiding lines for the eyes.

5.7 Lessons learned

5.7.1 g-factor determination

The tilting field technique is becoming almost the standard for the determination of the Lande g-factor in 2DES using level crossings deep in the integer QHE regime [46]. It is assumed in this approach, that if any exchange interaction exists in the system, it is additive to the bare Zeeman energy so that the effective Zeeman energy is in

fact:

$$\boldsymbol{E_{Z_{eff}} = g_0 \mu_B B_{total} + E_{ex} = g^* \mu_B B_{total}} \tag{5.7}$$

Where $\boldsymbol{g_0}$ and $\boldsymbol{g^*}$ represent the bare and the enhanced Lande g-factors respectively. From the coincidence condition (equation 5.1), knowing the first few coincidence angles, a plot of cos ($\boldsymbol{\theta}$) versus 1/r yields a slope equals to $\boldsymbol{m^* g^*}$. From there, knowledge of $\boldsymbol{m^*}$ allows one to calculate $\boldsymbol{g^*}$. We believe this method could not be applied to InSb QWs for the following reasons:

First, the exchange energy is not proportional to $\boldsymbol{B_{total}}$ but to its square root. So, even if the exchange energy is additive to the Zeeman energy, the relation

$$\boldsymbol{E_{Z_{eff}} = g^* \mu_B B_{total}} \tag{5.8}$$

cannot be used to define the real Lande g-factor in the system. Second, the determination of the coincidence angle is very uncertain especially in high-density samples were the QHE states of interest do not disappear. Finally and most importantly, InSb has a strongly non-parabolic band structure so that the product m*g* varies from one QHE state to the next. This makes the slope technique irrelevant.

5.7.2 Scattering mechanism

The dependence of the electron mobility on the carrier density discussed in chapter 4, hinted to strong contribution of remote ionized impurities and structural defects to carrier scattering in our samples. The observation that high carrier density samples display QHF irrespective of their electron mobility points to a great role played by remote ionized impurities in our samples. It is possible that high electron densities are needed to screen effectively the fluctuating potential profile introduced in the plane of the electron gas by remote ionized impurities in the $\boldsymbol{\delta}$-doped layers. The location of the $\boldsymbol{\delta}$-doped silicon layer in this case plays a key role on the properties of the system. It has been shown [47] that, the closer these $\boldsymbol{\delta}$-doped layers, the higher the chances of obtaining high-density samples. This happens because it is easier for

electrons from the $\boldsymbol{\delta}$-doped layer to fall into the QW when the spacer thickness is small. Unfortunately, the proximity of positive ions in the delta-doped layer leads to stronger scattering of carriers in the well due to Coulomb interactions between the ions and the electrons.

5.7.3 Consequence of disorder on quantum Hall ferromagnetism

Just as for standard ferromagnets, disorder affects how fast a QHF responds to the changing polarization field, by pinning the pseudospin domains at various lattice sites. The need to use very slow magnetic field sweeps to observe clear hysteresis loops in most of our samples points towards defects pinning of pseudospin domains. This effect is further displayed in the double bump formation in S697 and its unusual angle and temperature dependence. To the best of our knowledge, such behavior (multi resistance peaks) has never been reported in a QHF and requires further investigation.

5.8 Conclusions

Tilted fields experiments in InSb QWs revealed Ising QHF states at low filling factors ($\boldsymbol{\nu}$ <4) in high-density samples. The density threshold for the emergence of QHF was found close to 1.3x$\mathbf{10^{11}}$ $\boldsymbol{cm^{-2}}$. Our quantum Hall ferromagnets resembled those observed in other narrow single well from non-magnetic semiconductor materials such as AlAs in the sense that they are accompanied by resistance peaks that grow with increasing temperatures and move with increasing tilt angles. They differed from AlAs-based QHF in two ways: the resistance peak motion with tilt angle and the density effect on the angle for the onset of QHF. While in AlAs the resistance peaks moved to lower filling factors with increasing tilt and the QHF appeared at higher angles with increasing densities, in InSb, the opposite trend is observed: the resistance peak moved to higher fillings and the onset of QHF is pushed to lower tilt angles with

increasing densities. The fact that resistance peaks did not show up simultaneously at more than one QHE states in InSb as was seen in AlAs can be attributed to non-parabolicity of the energy bands in InSb and a quicker drop of the exchange energy with increasing filling factors in InSb due to its extremely small r_s values. It is also possible that the opposite trend in tilt angle effect on the peak motion and the carrier density on the onset of QHF has its origin in AlAs and InSb being on the opposite ends of the r_s scale. Using for AlAs, m^*=0.41m_e, ϵ(AlAs)=10.0ϵ_0, it can be shown that r_s(AlAs)$\sim$49 r_s(InSb). This work showed that stronger electron-electron interactions are found not at low density as in most semiconductor QWs,but at high density in our InSb QWs.

Left for future investigations are for instance, how do QHFs from crossings between levels from different electrical subbands differ from those presented in this thesis? Since localization lengths of the order of couple of microns are observed in our QHFs, it might be interesting to see how these states behave when the sample size is of the order of the localization length. We would also like to see the issues of hysteretic and anisotropic transport in InSb-based QHF settled. The hysteresis can be dealt with by repeating what we have done but in a much broader tilt angle-temperature-magnetic field sweep rate-current direction phase space. For the anisotropy, a double-axis tilter is necessary to nail down the question about the orientation of the pseudospin domains with respect to the in-plane field.

Finally, it might be interesting to compare our results to data from similar experiments in InAs. To the best of our knowledge such a study has not yet being done at very low filling factors ($\nu < 4$) in this material. Because r_s(InAs)$\sim$2 r_s(InSb), InSb data should compare better with InAs than AlAs data.

Chapter 6

Gating InSb Quantum Wells

6.1 Introduction

InSb combines features that make it attractive for many fundamental and technological applications. Application wise, its use has been limited to IR detectors operating at liquid helium temperature and magnetic field sensor applications only because of its non-mature technology. Recent progress in growth of high quality two dimensional electronic systems (2DESs) has opened a whole new world of possible applications: its high mobility at room temperature can be used to make high speed devices; its large Lande g-factor can be used to fabricate low field spin related devices; its large spin-orbit effect which gives rise to the Rashba effect in conjunction with its intrinsic Dresselhaus effect can be used in the emerging field of spintronics or more fundamental physics such as the spin-Hall effect. Work on the Rashba effect by the group at the University of Oklahoma [21] has shown that there is a significant zero field spin splitting in asymmetric InSb quantum wells. This can be enhanced using a gate bias to increase the electric field at the hetero-interface. Additionally to really take advantage of high temperature operation of quantum devices (QPC, ballistic transport etc) made on InSb, there is an urgent need to develop a reliable process by which high quality gate insulator can be grown or deposited since Schottky gates are impossible

on InSb. Finally for transport study, gates help to explore various density regimes within a single good sample.

Unlike silicon, thermally grown oxides on III-V semiconductors are poor for two main reasons: the oxide is a mixture of the group III and the group V oxides; and the oxidation must be carried out at temperatures higher than the sublimation temperature of the group V oxide. The oxide mixture introduces weak spots especially at grain boundaries, which ultimately increase the gate leakage current. Also problematic for oxide growth on InSb, is the difficulty of getting rid of the $\sim$3 nm thick native oxide which unfortunately introduces a high concentration of interface states. At high concentration, these states screen the semiconductor by pinning the Fermi level at the surface. The volatility of antimony oxide requires gating fabrication to be operated exclusively in the low temperature regime.

Many attempts have been made to grow / deposit high quality insulators with minimal interface state density on InSb [48]. At the time we started this project, good results were reported only for low temperature chemical vapor deposition (LTCVD) of $\boldsymbol{SiO_2}$ [49]. There are however reports indicating that CVD oxides grown at low temperatures manifest electrical instability due to large incorporation of hydrogen [50]. Moreover, the presence of an inherent native oxide [51] of questionable quality, between the semiconductor and the deposited oxide makes this gating scheme unreliable. We undertook an approach that avoids the use of CVD and consists in sandwiching a well-controlled anodic oxide between the semiconductor and another layer of insulator deposited by magnetron sputtering. The anodic oxide allows us to control the quality of the highly sensitive interface between the semiconductor and the oxide, and reduce sputtering deposition induced damage of the semiconductor surface.

This chapter gives a full detail of our gating fabrication.

6.2 Anodization

6.2.1 Introduction

Anodization offers the advantage of room temperature oxidation, making it the gating procedure of choice for InSb, should the anodic oxide (AO) be of high quality. Unfortunately, AOs on III-V semiconductors in general do not have the mechanical, chemical, and electrical strength required for device applications [52], however, properly grown AOs have superior quality compared to thermal or native oxides that instantly grow when the semiconductor is exposed to an oxidizing ambient. The quality of a gated structure depends on that of the gate insulator (it must be free of any structural defects (stacking faults, precipitates, pinholes, etc) and any electronic defects (no mobile and/or fixed charges, no trapped charges)), but most importantly on the quality of the semiconductor-insulator interface. We found that deposition of gate insulator straight onto an InSb surface results in a failed structure as one cannot deplete the semiconductor even if, its surface was carefully cleaned and /or etched. This observation is consistent with the pinning of the Fermi level in the conduction band at the semiconductor surface. Successful gating i.e., meaningful depletion of the semiconductor in a metal-insulator-semiconductor (MIS) structure, was realized only when a thin anodic oxide was grown on the semiconductor prior to gate insulator deposition. The quality of the AO-semiconductor interface shows no dependence on pre-anodization surface treatment but a strong dependence on: electrolyte composition, anodization conditions (anodization voltage and duration), and post-anodization heat treatment / annealing.

6.2.2 Experimental setup and procedure

The anodization process is carried out under constant voltage conditions in an electrochemical cell where the anode is the semiconductor to be oxidized, and the cathode, an inert metal electrode (platinum foil in our study).

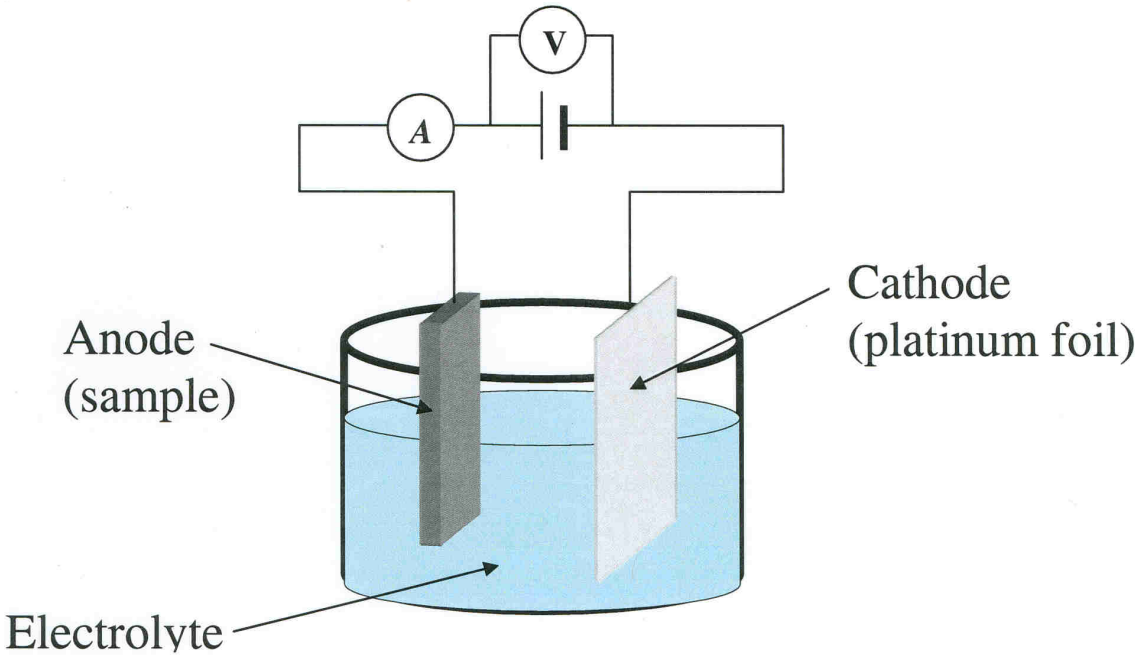

Figure 6.1: Schematic of the electrochemical cell used for anodization

The most important parameters to control are the electrolyte composition, the operating voltage, and the anodization time. Other parameters such as the geometry of the cathode (circular ring or rectangular foil), the separation distance between the electrodes (the smaller the better), illumination of the semiconductor, and the type of the semiconductor (n or p-type) did not show a marked effect on the properties of the grown oxides.

6.2.3 Results

The composition of the electrolyte plays a vital role in determining the properties of the anodic film and also the reproducibility of the process. It is well known that for a given semiconductor, some electrolytes may give barrier-type oxide films, some porous films, and others either of the above depending on the film thickness. For gating purposes, pore-free barrier-type oxide films are desirable. Below are the electrolytes

that have been tested during this study. Because thicker AO films tend to be porous, we always kept the grown film thin (<80 nm).

Electrolytes used

Ammonium Phosphate dibasic $(NH_4)_2HPO_4$

Ammonium phosphate dibasic with a molarity of 0.1 M was the first electrolyte we tried. This solution prepared by dissolving $(NH_4)_2HPO_4$ powder in deionized water, gave us non-reproducible results and more importantly, the electrolyte would regularly rise and touch the tungsten clip that we used to lower the semiconductor in the solution. The nonreproducibility of anodization in aqueous solutions is related to the fact that these electrolytes give optimum results only over a narrow pH range and are very sensitive to reagent contamination [53]. Failure to obtain reproducible results with $(NH_4)_2HPO_4$ electrolyte, forced us to explore other electrolyte systems.

Glycol based electrolytes

Mixed aqueous glycol electrolytes are known to be relatively insensitive to the presence of contaminants and to consistently give high quality oxides compared to that obtained with aqueous solutions [54].In these systems, water is the oxidant and an acid or a base is used for pH/conductivity control. Because glycol is relatively viscous, its role seems to be to limit the diffusion rate of ions and / or dissolution products in the electrolyte. We had no problem with a rising meniscus with this electrolyte. The following variations were investigated in our study: 3% citric acid (1 part) + ethylene glycol (2 to 4 parts) (2% or 3%) tartaric acid (1 part) + propylene glycol (2 to 4 parts) 2% tartaric acid (1 part) + ethylene glycol (2 to 4 parts) 29% ammonium hydroxide (1 part) + ethylene glycol (5 parts) All of these electrolytes gave reproducible high quality anodic oxides. There was no difference in using ethylene or propylene glycol. The oxide quality did not show a major difference with the increase of the glycol content from 2 to 4 parts. To decide which acid system to use, we performed

a simple electrical breakdown test on AO grown under same conditions (anodization voltage of 10 V, and anodization time of 4 minutes), from citric acid and tartaric acid and found that the oxide from tartaric acid based system could withstand higher voltages than the oxide from citric acid based solutions (minimum breakdown voltage of 20 V versus 5 V).

From there on, we adopted the mixture of 2% tartaric acid and propylene glycol with a volume-mixing ratio of 1:2, known in the literature as AGW (Acid Glycol water). The electrolyte from 29% $\boldsymbol{NH_4}$OH and Ethylene glycol with volume mixing ratio of 1:5 is referred to as BGW (Base Glycol Water). Fluorinated electrolytes (FAGW or FBGW) are those to which, few drops of 40% $\boldsymbol{NH_4}$F were added to improve the quality of the anodic oxide.

Anodization voltage

Once the semiconductor is dipped into the electrolyte, the difference in electrochemical potential between the electrolyte and the semiconductor causes holes transfer from the semiconductor to the electrolyte until equilibrium is reached. The charge transfer creates a depletion layer in the semiconductor, and promotes the semiconductor surface atoms to a higher oxidation state. This spontaneous effect results in the growth of few monolayers of anodic oxide upon reaction between the semiconductor ions and hydroxide ions in the electrolyte. Oxidation beyond these few monolayers requires supply of holes to the semiconductor surface. And it is done in this work, by applying a voltage bias exceeding the semiconductor/electrolyte junction breakdown voltage ($\boldsymbol{V_{break}}$). During anodization, AO growth on the semiconductor causes a reduction of the voltage bias available across the depletion layer ($\boldsymbol{V_{dep}}$). The oxide growth stops when $\boldsymbol{V_{dep} < V_{break}}$. Taking into account possible dissolution of the oxide being formed, it is shown that the oxide thickness ($\boldsymbol{d_{ox}}$) is related to the applied voltage ($\boldsymbol{V_A}$) by [55]:

$$\boldsymbol{d_{ox} = \frac{(V_A - V_r)}{E_{ox}}(1 - \frac{I_d}{I_0})} \tag{6.1}$$

where $\boldsymbol{V_r}$ is the sum of the rest potential of the anodization cell and the breakdown voltage associated with the depletion layer of the semiconductor, $\boldsymbol{E_{ox}}$ is the average electric field across the oxide, $\boldsymbol{I_d}$ is the equivalent dissolution current associated with the dissolution of the oxide film, and $\boldsymbol{I_0}$ is the initial current flow when the voltage is turned on. Figure 6.2 shows the anodization voltage dependence of the oxide thickness for a given electrolyte (AGW) and anodization time of 1 minute. The oxide grows quite linearly with increasing voltage ($\boldsymbol{d_{ox} \sim 29.2V_A + 34)\mathring{A}}$, but the growth rate is reduced by nearly $\boldsymbol{30\%}$ at higher voltages ($\boldsymbol{V > 8V}$) due to the combining effect of limited diffusion as the oxide gets thicker, and etching of the oxide being grown.

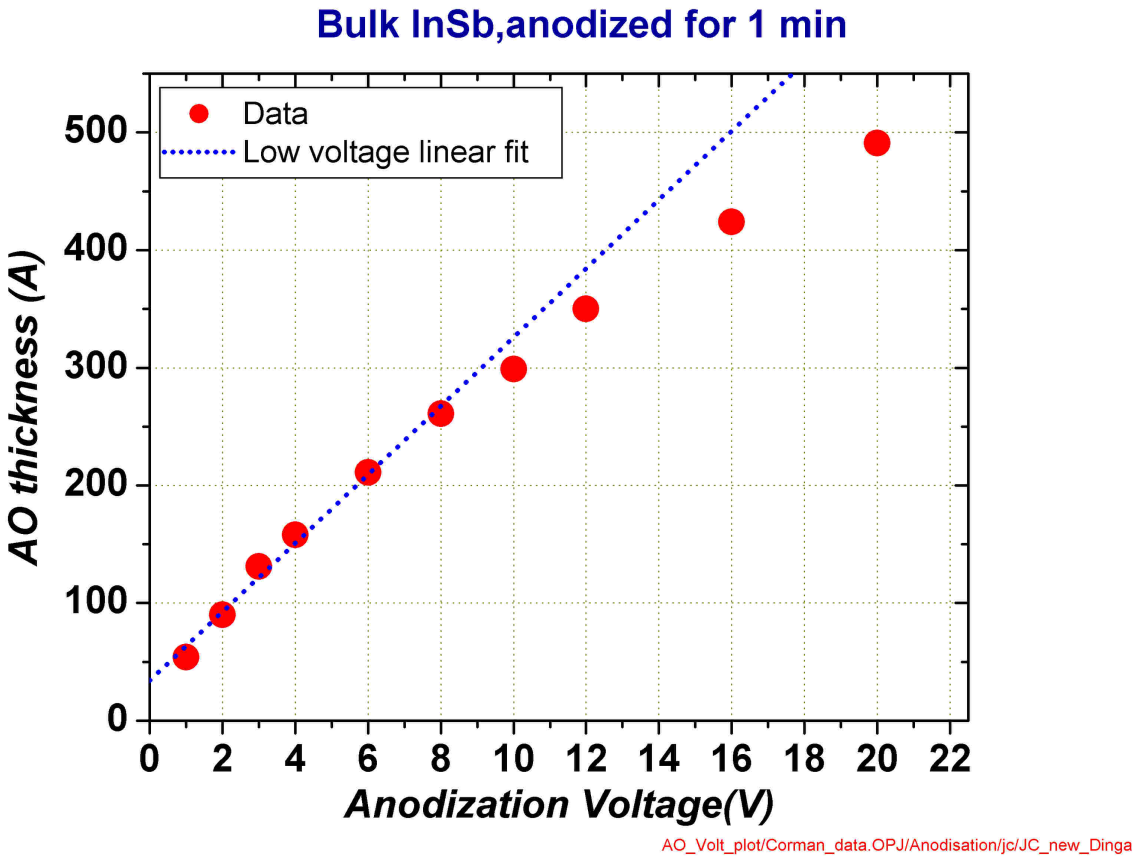

Figure 6.2: Dependence of oxide thickness on anodization voltage for bulk InSb anodized for 1 minute in AGW-like electrolyte (**2%** citric acid: propylene glycol, 1:2 volume mixing ratio). The dotted line represents the linear fit to low voltage data.

Anodization time effect

For a given anodization voltage, the thickness of the AO can be controlled by the anodization time. The AO is expected to exhibit an exponential growth of the form:

$$\boldsymbol{d_{ox} = d_0(1 - exp(-\frac{t}{\tau_f}))} \tag{6.2}$$

Where $\boldsymbol{\tau_f}$ is the time constant for growth, $\boldsymbol{d_0}$ is the final thickness for an infinite time of growth. Our data shown on figure 6.3 below is consistent with the prediction. The best fit to the experimental data used $\boldsymbol{d_{ox}} = 143\ \boldsymbol{\mathring{A}}$, and $\boldsymbol{\tau_f} = 4.475\ \boldsymbol{s^{-1}}$. The refractive index of the AO ranges from 1.98 to 2.17.

Anneal effect

The oxide grown by anodization is likely to have some trapped water molecules. Heating AO to higher temperatures might help remove those molecules and as a result change the physical and electrical properties of the oxide. Ellipsometric measurements could not detect any substantial difference (neither in oxide thickness nor refractive index) between the as-grown oxide and the same oxide annealed at $\boldsymbol{300^o}$C for 10 minutes in forming gas (20% $\boldsymbol{H_2}$ and **80%** $\boldsymbol{N_2}$). However, as will be shown later,annealing under these conditions has a marked effect on the electrical properties of the semiconductor/AO interface.

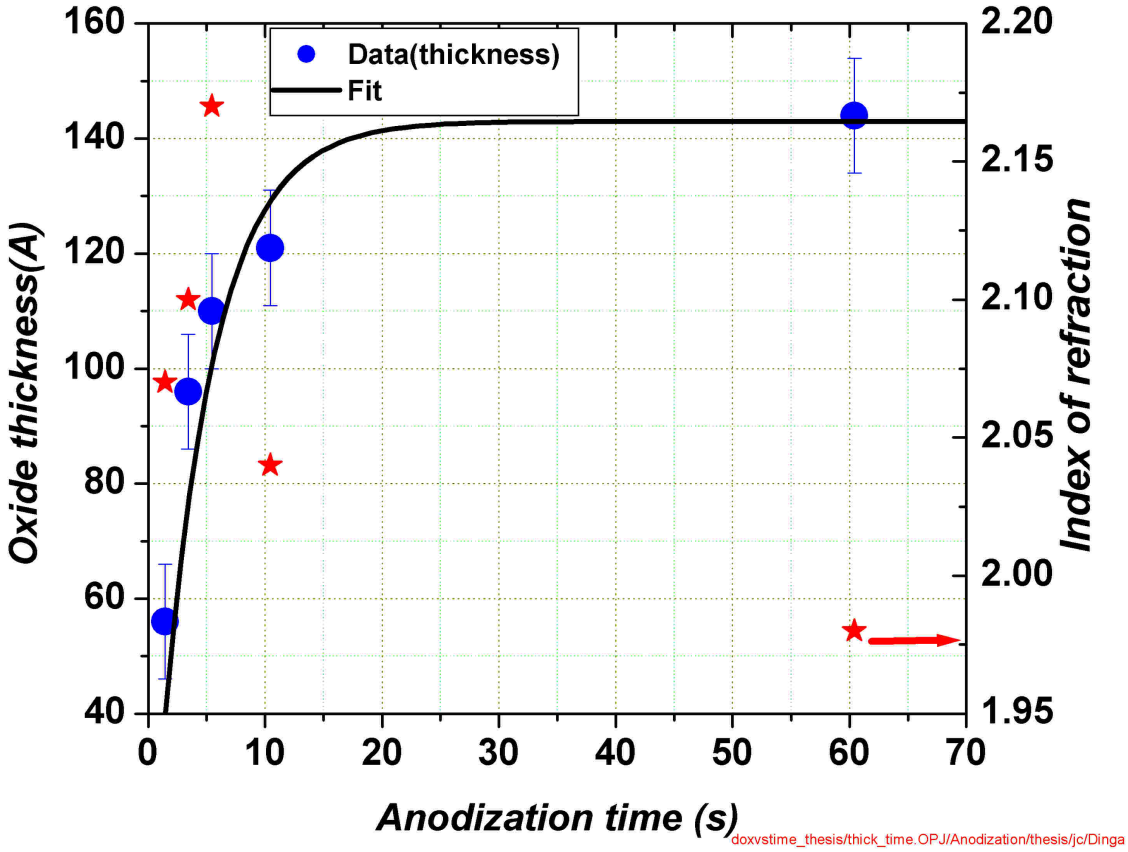

Figure 6.3: Time dependence of oxide thickness and index of refraction of AO on InSb (S849) at a constant voltage of 5.0 V in FBGW electrolyte (BGW + 1.33% vol. 40% NH_4F). Open circles represent the oxide thickness and the stars, the index of refraction on the right vertical axis.

6.2.4 Chemical analysis of anodic oxide by XPS

We used X-ray photoelectron spectroscopy (XPS) formerly known as electron spectroscopy for chemical analysis (ESCA) to understand the nature of oxides formed during anodization of InSb, and to look into the impacts of process parameters (electrolytes, annealing and fluorination) on the chemical composition of the grown oxide.

Developed in the mid-1960s by Kai Siegbahn [56], XPS is considered one of the

most important characterization techniques for studying the chemical nature of dielectrics grown or deposited on semiconductors [57]. The technique consists in irradiating the sample with monoenergetic soft X-rays and measuring the energy of the electrons emitted from the sample via the photoelectric effect. Though the incident X-ray can travel very large distances ($\sim$ microns) through solids, in XPS one is concerned only with elastically scattered electrons. This makes XPS useful mostly for the layers close enough to the surface to let the electrons escape without notable energy loss. It is shown that the kinetic energy (KE) of an ejected electron is given by:

$$\boldsymbol{KE = h\nu - BE - \phi_B} \tag{6.3}$$

Where h$\boldsymbol{\nu}$ is the energy of the excitation X-ray, BE the binding energy of ejected electron, and $\boldsymbol{\phi_B}$ the spectrometer work function. XPS is an element specific technique because each element has a unique set of binding energies whose chemical shifts are direct signatures of the immediate chemical environment the element is in. The data presented here were collected with a VGX900 data acquisition system (Fisons Instruments) with the samples in an analysis chamber equipped with a VG 100AX hemispherical analyzer, an XR3E2 dual anode x-ray source, and an LEG62 electron gun. The pressure in the analysis chamber during the experiments was kept at $\mathbf{10^{-9}}$ torr or lower, the photoelectrons excited either with Mg $\boldsymbol{K_\alpha}$ (h$\boldsymbol{\nu}$ = 1253.6 eV) or Al $\boldsymbol{K_\alpha}$ (h$\boldsymbol{\nu}$ = 1486.6 eV). The energy of the ejected photoelectrons was measured using the hemispherical analyzer operating in a constant analyzer energy (CAE) mode with a pass energy of 20 eV. The spectrometer work function was $\boldsymbol{\phi_B}$=4.2 eV as specified by the manufacturer.

We present in this thesis the results from samples (from wafer S849) with very thin anodic oxides (see table 6.1). Data from thicker AO were no different from those presented here. The samples were mounted on a gold-coated copper sample holder and held with tungsten clips. The sample holder with the samples was then positioned in the analysis chamber. For the anneal experiments, the samples were transferred from the analysis chamber to a heating stage without breaking the vacuum, where

they were heated at various temperatures in order of increasing temperatures. The temperature was measured with a thermocouple in good thermal contact with the heating plate. Because thermocouple was used, the temperatures quoted in this work are only known to $\pm\mathbf{50}^{o}$C.

Figure 6.4 and figure 6.5 show the Sb 3d and In 3d photolines of the three samples taken at room temperature. It is evident that the anodic oxides are very different from the native oxide on the bare sample, and that all the electrolytes lead to very similar oxides. Figure 6.6 shows however, that fluorine is being incorporated into oxide from the fluorinated electrolyte. The split of the Sb 3d peaks on the bare sample is consistent with the coexistence of bulk Sb/InSb peaks at low energy and antimony oxide (SbOx) peaks at higher binding energies. In the AOs only the SbOx peaks are clearly resolved. Because of the proximity of the Sb $3d_{\mathbf{5/2}}$ oxide peak to the O 1s line at $\sim$ 531 eV, the peak at $\sim$ 530.5 eV should be considered as being the contribution of SbOx and all other oxides present in the system (InOx, as well as AuOx or WOx (from sample holder), etc). The In 3d peaks are more difficult to identify because the chemical shifts between bulk InSb and InOx are very small (see table 6.2). The asymmetry of these photolines as well as their slight shift to lower binding energy in the bare sample, point, similar to the case for Sb 3d, to a mixture

		bare InSb	AGW	FAGW
Anod. conditions	Anod. voltage	N/A	5V	5V
	Anod. time	N/A	1sec	1sec
	Electrolyte	N/A	AGW	AGW+**1%** vol. NH_4F
Oxide properties	Thickness($\mathring{\boldsymbol{A}}$)	28	54	74
	Refractive index	2.63	2.40	2.21

Table 6.1: Useful data for samples used in the XPS characterization. The samples were from wafer S849 with typical size of 5x5 $\boldsymbol{mm^2}$. Oxide thickness and index of refraction were measured with L111 Gaetner Ellipsometer using a He-Ne laser.

of In 3d signals from In/InSb and InOx on the bare sample. The unambiguous shift of the In 3d peaks to higher binding energy in anodic oxides, and their symmetric line shapes indicate that the signal is mostly from InOx on AOs. The XPS data indicate that our anodization procedure produces passivating films made of a mixture of In and Sb oxides, with fluorine being incorporated in AOs from fluorinated electrolytes. The identification of the oxides as $\boldsymbol{In_2O_3}$ and $\boldsymbol{Sb_2O_5}$ was carried out using a combination of the modified Auger parameter (AP) for InOx and the extent of the chemical shift for SbOx. The concept of Auger parameter, introduced by C.D. Wagner [58] turns out to be a very efficient way to identify many chemical compounds by XPS. Because absolute location of photolines in XPS can be hampered by sample charging (thus the need for good energy reference (usually Carbon 1s peak)), or by errors on the spectrometer work function, Wagner suggested that a more accurate identification could be achieved using the energy difference between the photoline and the Auger line of the same element in a given sample. Because the Auger parameter is an energy difference, it does not suffer from errors introduced in peak position determination. The Auger parameter is defined as

$$\boldsymbol{AP = KE(AES) - KE(XPS)} \tag{6.4}$$

where KE(AES) is the kinetic energy of the Auger electron and KE(XPS) the kinetic energy of the photoelectron from the same element. Because the kinetic energy depends on the excitation source, a more universal term coined, modified Auger parameter was introduced and it is independent of the excitation source.

$$\boldsymbol{AP_{mod} = h\nu + AP = h\nu - [BE(AES) - BE(XPS)]} \tag{6.5}$$

Where BE stands for the binding energy. The kinetic energies were converted into binding energies using equation (6.3).

Various oxide species of the same element, including indium, have very large differences in their modified Auger parameters and can be identified even though the chemical shifts are nearly impossible to resolve. The modified AP value of 851.1

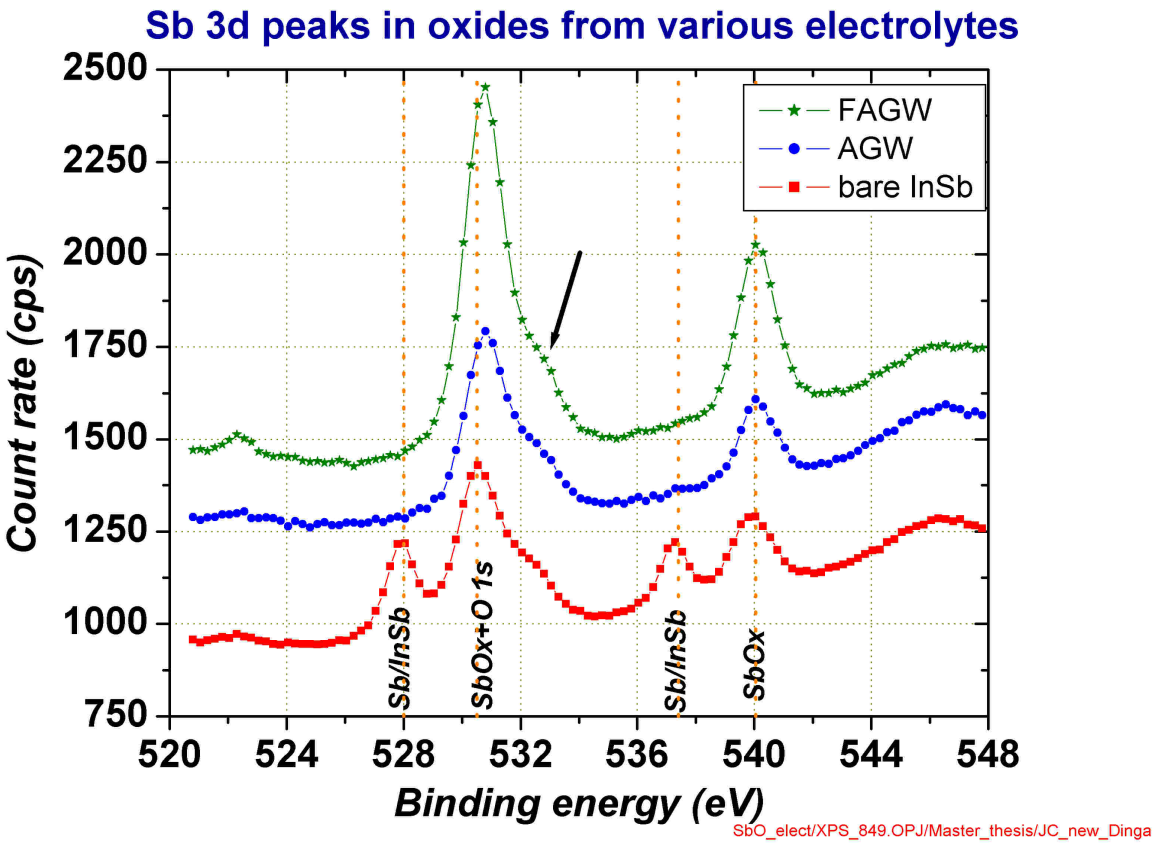

Figure 6.4: Room temperature XPS spectra for the Sb 3d photolines on samples mentioned in the text. Note the disappearance of the Sb/InSb peak in anodic oxides. The shoulder indicated by the arrow is O 1s peak at $\sim$ 532.5 eV in $\boldsymbol{Au_2O_3}$. It is coming from the Au coated sample holder. The spectra are shifted vertically for clarity.

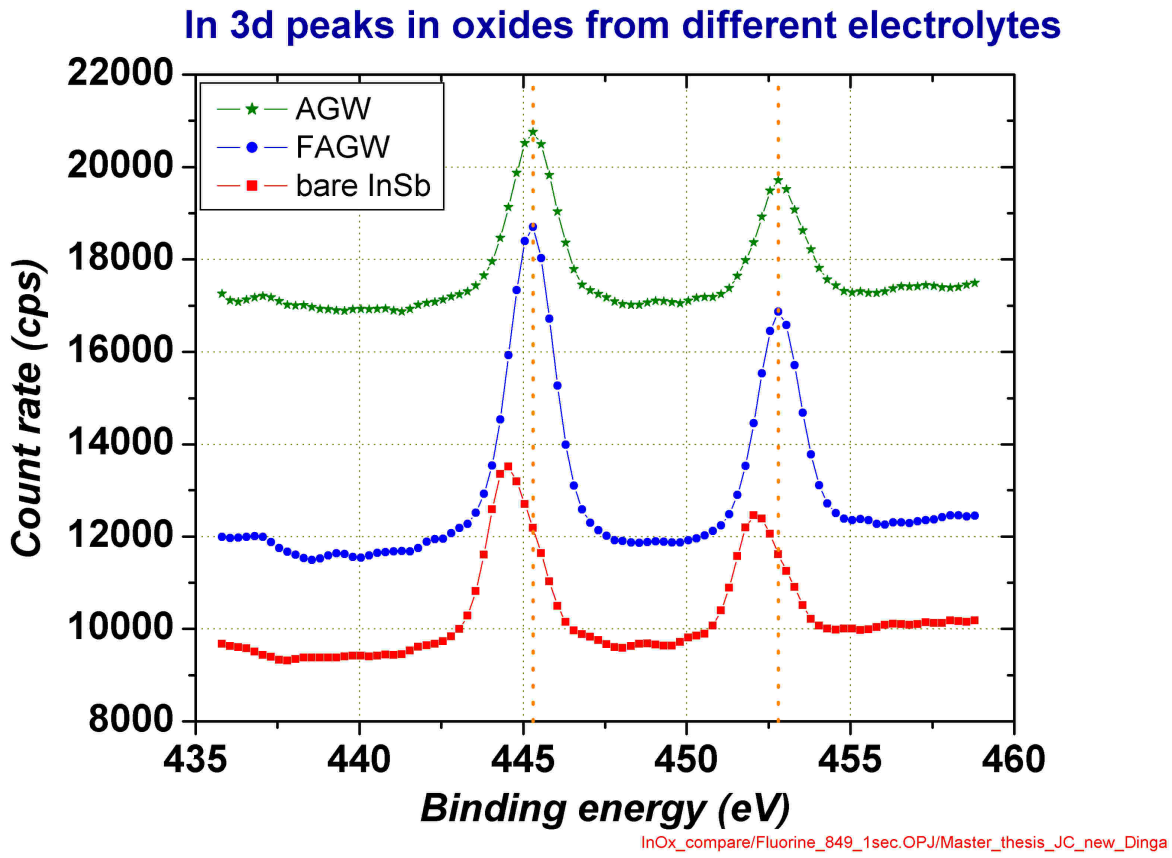

Figure 6.5: Room temperature XPS spectra for the In 3d photolines on samples mentioned in the text. Note the asymmetry and the shift to lower binding energies of the peaks in the bare sample. The spectra are shifted vertically for clarity.

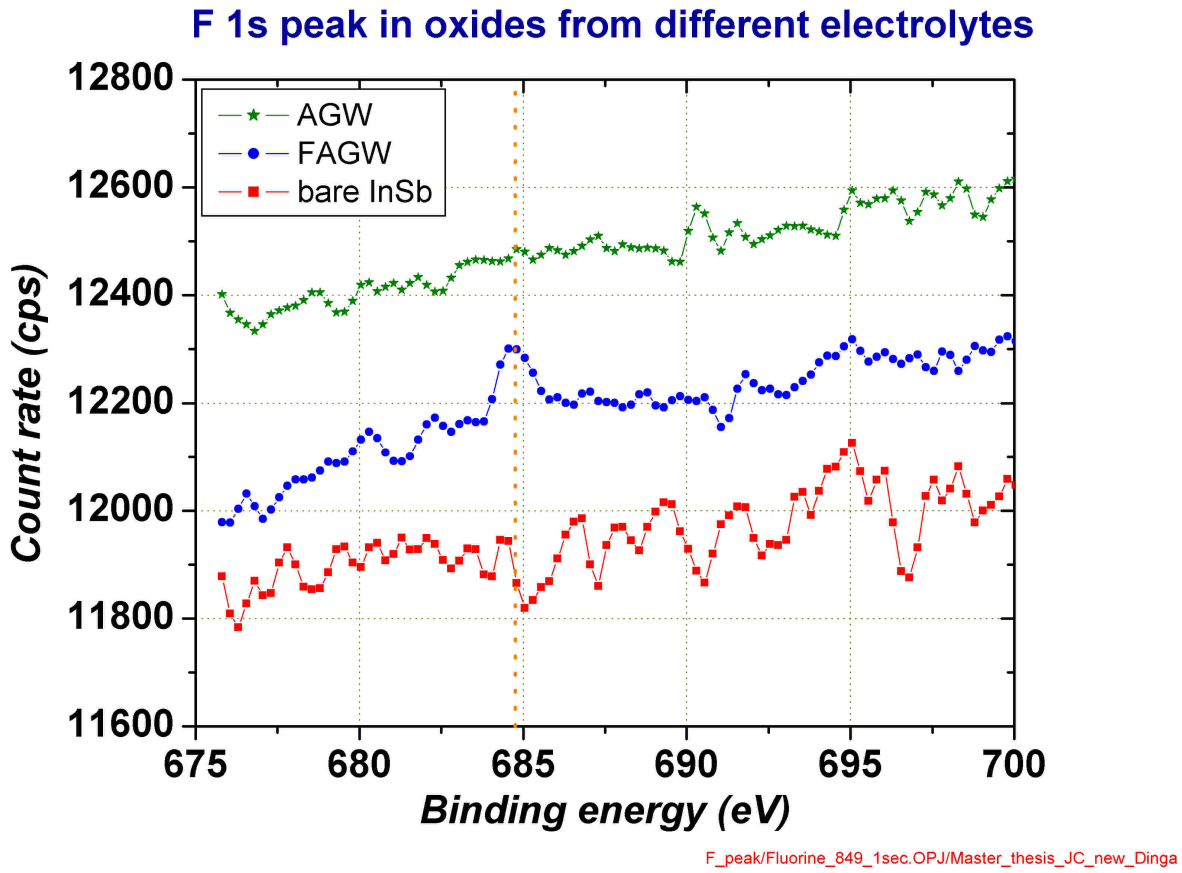

Figure 6.6: Room temperature XPS spectra for the F 1s photoline on samples mentioned in the text. Note the peak at $\sim$ 684.8 eV only in the oxide from the fluorinated electrolyte. The peak signals the incorporation of a detectable amount of fluorine in the AO. The spectra are shifted vertically for clarity.

Compounds	In $3d_{5/2}$(eV)	Sb $3d_{5/2}$(eV)	AP_{mod}(eV)
InSb	444.2[60]	527.8[60]	853.2[a]
InSb	*444.5*	*527.8*	*852.6*[a]
In_2O	444.3[b]		850.9[b]
$In(OH)_2$	445.2[b]		850.3[b]
In_2O_3	444.5[60]		851.2[b]
InOx	*445.3*		*851.1*
Sb_2O_3		529.4[60]	989.6[a]
Sb_2O_5		530.5[60]	989.7[b]
SbOx		*530.5*	*989.6*

Table 6.2: Summary of the binding energies and modified Auger parameters of In and Sb in various compounds. Our data are in italics. AP_{mod} values for InSb are with respect to In $3d_{5/2}$. [a] C.D. Wagner and A. Joshi, J. Elect. Spect. Rel. Phen.,47, 283 (1988). [b] D. Briggs and M.P.Seah, Practical Surface Analysis by Auger and X-ray Photoelectron Spectroscopy, John Wiley & Sons (1983).

eV between the In $3d_{5/2}$ and In M4N45N45, found for our InOx is consistent with In_2O_3 [59] being formed on all the AOs. AP cannot be used for the identification of SbOx, because Sb_2O_3 and Sb_2O_5, the most thermodynamically stable oxides for Sb, have almost the same Auger parameter [59]. Fortunately the chemical shifts of these oxides are different enough (>1 eV) to allow identification of the SbOx. The rather large chemical shifts (>2 eV) observed in our data are consistent with Sb being oxidized to a higher degree; hence Sb_2O_5 is more likely than Sb_2O_3 in our samples. Observation of In_2O_3 and Sb_2O_5 as main oxide species in anodic oxides grown on InSb is not new; it has already been reported by W.K. Liu *et al.* for the anodization of InSb in KOH [60].

Figures 6.7 and 6.8 show respectively the effect of anneal on the bare sample and the fluorinated AO. With increasing temperatures, the oxide peaks in the bare sample

weakened without shifting position, while the Sb/InSb peaks gained strength. This is consistent with oxide desorption upon high temperature anneal. Any modification happening in the fluorinated AO could not be resolved on our system. The peaks show no change upon high temperature anneal.

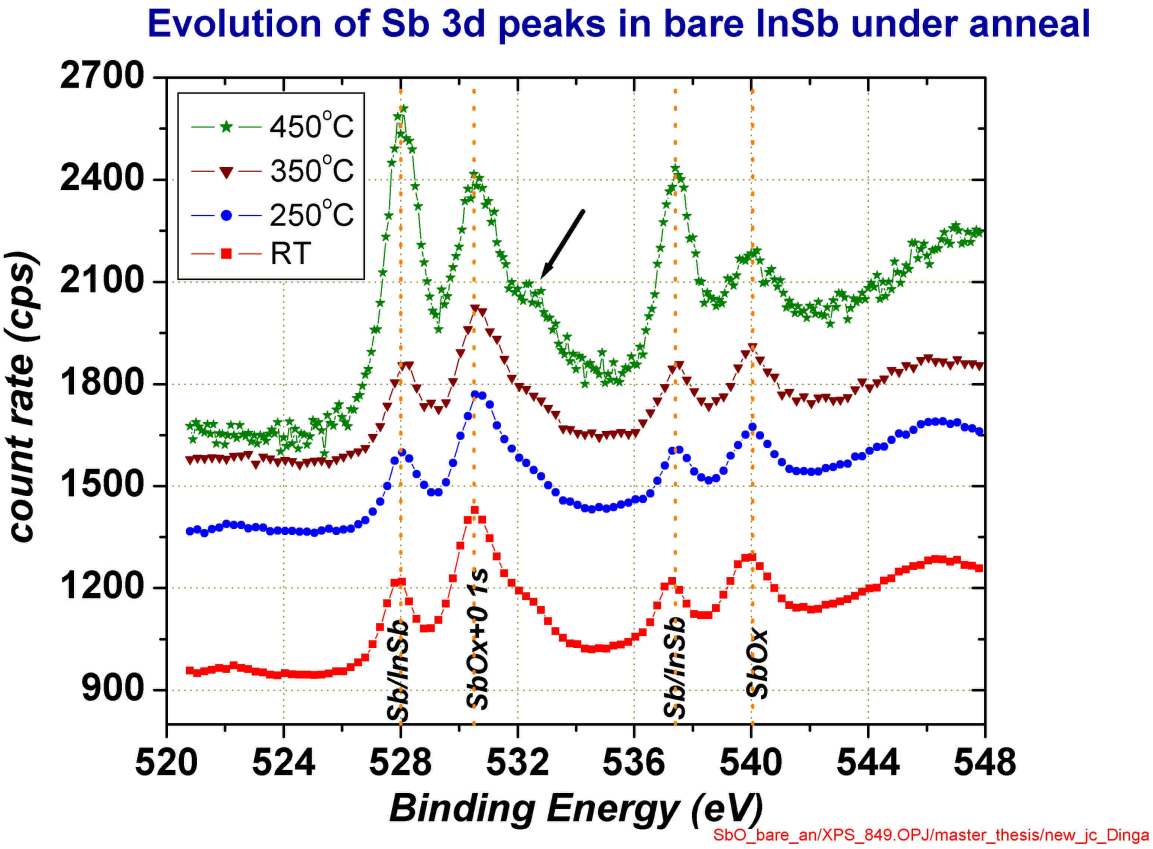

Figure 6.7: XPS spectra for the Sb 3d photolines on bare InSb after various high temperature anneals. Note the reduction in intensity of the SbOx photolines with respect to InSb photolines upon increasing anneal temperatures. The shoulder indicated by the arrow is O 1s peak at $\sim$ 532.5 eV in $\boldsymbol{Au_2O_3}$. It is coming from the Au coated sample holder. The spectra are shifted vertically for clarity.

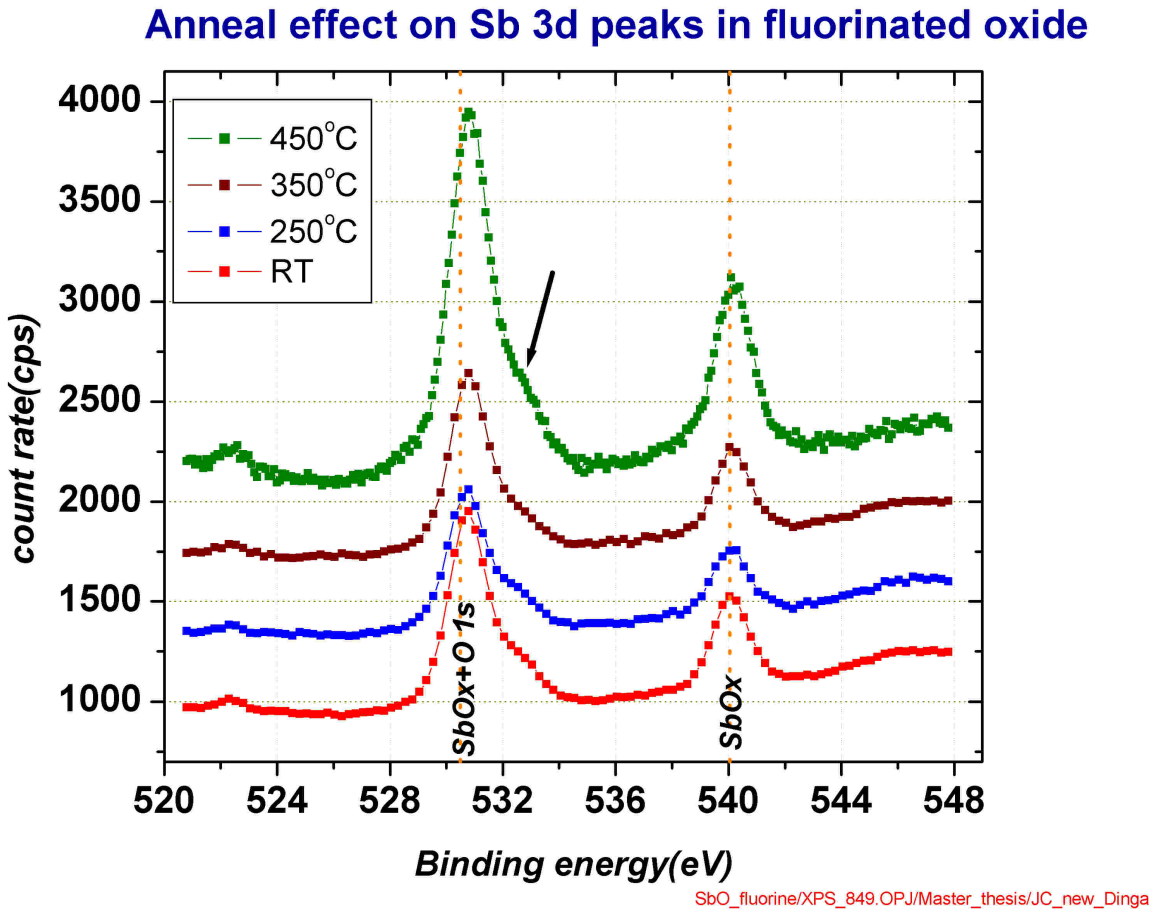

Figure 6.8: XPS spectra for the Sb 3d photolines on AO from fluorinated electrolyte (FAGW) after various high temperature anneal. Note that within the resolution limit of our system, the spectra are not affected by the anneal. The shoulder indicated by the arrow is O 1s peak at $\sim$ 532.5 eV in $\boldsymbol{Au_2O_3}$. It is coming from the Au coated sample holder. The spectra are shifted vertically for clarity.

6.2.5 Anodic oxide growth mechanism

To find ways to control the quality of the grown oxide, and keep the kinetics of the anodization process under check, it is important to understand the growth mechanism of these oxides. From the many studies conducted on anodic oxides on III-V semiconductors, the following growth mechanism, based on the mechanism suggested by P.A. Breeze *et al.*[61] seems likely. Water in the electrolyte medium dissociates into $\boldsymbol{H^+}$ and $\boldsymbol{(OH)^-}$

$$\boldsymbol{2H_2O \longleftrightarrow 2H^+ + 2(OH)^-} \tag{6.6}$$

The large electric field applied between the semiconductor and the cathode, ionizes by hole transfer the semiconductor into $\boldsymbol{In^{3+}}$ and $\boldsymbol{Sb^{5+}}$.

$$\boldsymbol{InSb + 8h^+ \longrightarrow In^{3+} + Sb^{5+}} \tag{6.7}$$

The ions then combine with $\boldsymbol{OH^-}$ to form hydroxide for In and antimony oxide ions for Sb.

$$\boldsymbol{In^{3+} + 3OH^- \longrightarrow In(OH)_3} \tag{6.8}$$

$$\boldsymbol{Sb^{5+} + 5OH^- \longrightarrow SbO_5^{5-} + 5H^+} \tag{6.9}$$

These compounds subsequently form $\boldsymbol{In_2O_3}$ and $\boldsymbol{Sb_2O_5}$

$$\boldsymbol{2In(OH)_3 \longrightarrow In_2O_3 + 3H_2O} \tag{6.10}$$

$$\boldsymbol{2SbO_5^{5-} + 10H^+ \longrightarrow Sb_2O_5 + 5H_2O} \tag{6.11}$$

The overall reaction is then

$$\boldsymbol{2InSb + 16h^+ + 8H_2O \longrightarrow In_2O_3 + Sb_2O_5 + 16H^+} \tag{6.12}$$

Subsequent oxide growth proceeds by interstitial migration of $\boldsymbol{In^{3+}}$ and $\boldsymbol{Sb^{5+}}$ from the semiconductor/oxide interface to the oxide/electrolyte interface under the influence of the electric field. At the same time oxygen is transported from the oxide

surface towards the interface via vacancies. This model accounts for possible group V build up in elemental form at the semiconductor/oxide interface as due to preferential oxidation of Indium (low oxidation activation energy) and higher In^{3+} drift rate (small ionic radius). This growth mechanism also explains the anodization voltage and the anodization time effects, and how the pH of the electrolyte or the addition of small amount of fluorine would affect the electrical quality of the semiconductor/anodic oxide interface, as will be shown later with the electrical analysis section of this chapter.

6.3 Sputtering deposition of insulators

6.3.1 Introduction

Introduced in 1852 by W.R. Grove [62], sputtering was developed into a thin film deposition technique by Langmuir in 1920s. Because of its attractive properties such as good step coverage, the capability for in-situ substrate cleaning prior to deposition, the ability to produce layers of compound materials, and its application to a wide variety of materials from metals to insulators, sputtering has quickly become the deposition technique of choice in microcircuit technology.

Sputter deposition is carried out in a self-sustained glow discharge (plasma) created by applying an electric field across a gap containing a low-pressure gas. The voltage (V_{bd}) required to breakdown the gas is given by Paschens law:

$$V_{bd} \propto \frac{PL}{log(P)L + B} \tag{6.13}$$

where P is the chamber pressure, L is the electrode spacing, and B is a constant.

Once the plasma, a mixture of ions, electrons, and neutral species is formed, charged species are accelerated towards specific electrodes. The charge transport between the electrodes will result in some ionizing collisions. The products of these collisions are themselves accelerated because of the electric field, so that they can

also enter into collisions with neutral molecules, thus resulting in an avalanche multiplication effect. The positive ions contained in the plasma are accelerated towards the target material held at the cathode where they eject target material atoms by momentum transfer and release secondary electrons. The ejected atoms are subsequently deposited at the substrate positioned at the anode. Electrons that do not collide with ions or other species in the plasma are collected at the anode (substrate) where they cause unwanted heating. In the magnetron configuration, a magnetic field is used to confine those electrons around the target surface preventing them from hitting the sample surface. Magnetron sputtering therefore offers many advantages: the confinement of electrons around the target surface prevents electronic heating of the substrate; increases the probability of ionizing collisions which in turn increases the sputtering gas ion concentration, and hence the film deposition rate. For reactive sputtering, the inert sputtering gas is replaced by an inert / reactive gas mixture, so that chemical reaction occurs between atoms ejected from the target and ions contained in the plasma before the material is deposited on the substrate. Under reactive sputtering, the deposited material is different from the target material.

6.3.2 System used

The deposition system used in this work consisted of a Torus-2C planar magnetron marketed by Kurt J. Lesker (KJL) Company. The Torus-2C is a water-cooled sputtering system that can be operated either in the DC mode (best for conducting targets) or RF mode (best for semiconducting and insulating targets). It utilizes a samarium-cobalt permanent magnet to confine secondary electrons near the surface of the target. The power supply is an advanced Energy RFX-600 operating at 13.56 MHz and is able to supply up to 600 W of continuous or pulse power. To keep the complex impedance of the plasma to 50 $\mathbf{\Omega}$, the power supply is connected to ATX-600 tuner, an RF matching network made of a combination of resistors, inductors, and variable capacitors. The capacitors are automatically tuned to keep the output

impedance constant. For more information about the Torus-2C and power supply, consult their manuals.

The vacuum system is composed of a roughing pump and a turbo molecular pump. Typically, we use the roughing pump to evacuate the deposition chamber to 2x$\mathbf{10^{-2}}$ torr in approximately 40 minutes and switch to the turbo pump to get the base pressure of $\sim$3x$\mathbf{10^{-6}}$ torr in about 30 minutes. To keep a reasonable pumping speed on the roughing pump, we change its oil every 3 to 6 months. For gate insulator deposition, we use 0.125 in thick by 2 in diameter high purity $\boldsymbol{SiO_2}$ (99.995%) or $\boldsymbol{Si_3N_4}$ (99.9%) target marketed by KJL. The process gas is an ultra high purity argon (99.9997%) gas and for reactive sputtering, we add a high purity oxygen (99.994%) gas in the deposition chamber. Presently, gas flow and pressure are controlled using gas regulators and a combination of toggle and needle valves. This provides reasonable control of gas flow and partial pressures in the low pressure operation settings. For operations at pressures above 2.5 mtorr, the control is rather poor and one needs to frequently adjust the chamber pressure during deposition. (a very difficult task when the sputtering gas is made up of 2 or more gases with specific desired partial pressures.) Better control of gas flow and partial pressure may be achieved using computer controlled mass-flow controllers. A mechanical shutter is used to protect the substrate during pre-sputtering. This step is important as it helps remove any surface contamination on the target, getter reactive gases such as $\boldsymbol{O_2}$, $\boldsymbol{H_2O}$, and $\boldsymbol{N_2}$ from the chamber, as well as coat other reactive elements from previous depositions that are on the side wall of the chamber. The deposition starts when the shutter is removed and continues until the shutter is inserted back or the power supply is turned off. During film deposition, the film thickness is monitored using a quartz crystal monitor (QCM500). The thickness of the deposited film is determined indirectly by measuring the changes in the resonant frequency of the quartz crystal oscillator as material is being deposited. Input parameters needed for film thickness determination include film density, tooling factor, and acoustical impedance also known as the Z-

ratio. The tooling factor accounts for geometric effects while the Z-ratio compensates for the acoustic impedance mismatch between the crystal and the deposited material. For the work reported in this thesis, we had the crystal monitor as close as possible to the substrate and the input parameters are given in the table 6.3 below.

Target material	Density(g/cc)	Z-ratio	Tooling factor
$Si\boldsymbol{O_2}$	2.20	1.070	1.0
$Si_{\boldsymbol{3}}\boldsymbol{N_4}$	3.44	8.83*	1.0

Table 6.3: Input parameters used to monitor film thickness during sputtering deposition of gate insulators.* Default value for $\boldsymbol{Si_3N_4}$. We could not find the value of Z-ratio for $\boldsymbol{Si_3N_4}$ in the literature.

Comparison between thicknesses given by the crystal monitor and other insulator thickness measurement techniques (ellipsometry, surface profilometry, and SEM) showed that the deposited film was consistently about 3 times thicker than the value displayed on QCM500.

6.3.3 Details of deposition procedure for $\boldsymbol{SiO_2}$ and $\boldsymbol{SiN_xO_y}$

The use of sputtering deposition for gate insulator deposition on InSb is difficult as one must keep the substrate temperature low, and minimize sputtering deposition induced physical damage, while preserving good film uniformity and high resistivity. Understanding the film formation process during sputtering helps in optimizing the process.

The atoms ejected from the target material suffer collisions with ambient gases between the electrodes and finally land on the substrate surface. These adatoms then diffuse on the surface until they form nuclei of critical size. Once stable nuclei are formed, they grow to islands by capturing more adatoms. The islands merge to form films. High surface mobility and / or optimum incident ions energy are crucial

for smooth, continuous films formation. Surface mobility can be adjusted via the substrate temperature while incident ion energy can be adjusted using substrate bias or chamber pressure.

Following the zone model introduced by Movchan and Demchishin [63], films deposited at low substrate temperature are characteristic of zone 1. Zone 1 films are mostly amorphous, highly porous with low mass density. This zone should be avoided for gate insulator purposes. At intermediate substrate temperatures, sputtered films are likely to be smooth or mirror like, and have very small grains. These films fall into the T zone, the Holy Grail for film deposition by sputtering. At higher temperatures, grain sizes increase, leading either to zone 2 with tall narrow columnar grains or zone 3 with large 3-D grains. Films under these conditions have moderately rough surfaces and appear milky or hazy. Because boundaries between zones vary from material to material, and the control of substrate heating during plasma deposition is difficult, the deposition conditions must be properly optimized for any application.

Another key parameter to keep in check is the stress level in deposited films. Too much stress can cause the film to peel off. In a clean deposition environment, stress is believed to originate mostly from the thermal expansion coefficient mismatch between the substrate and the film. In general, the stress level depends on substrate temperature, deposition rate, film thickness and the background ambient. Post deposition annealing can be used to relieve the stress. No attempt was made to investigate stress level in sputtered deposited films reported in this study. For the most part, we have relied on a visual inspection of the films, looking for any hazy appearance, peel off or breakage.

We made use of wafer cooling, substrate-to-target distance separation, deposition pressure, and RF power to find the optimal condition for deposition of high quality gate insulator on InSb. To minimize sputtering induced damage on the semiconductor, we kept the substrate-to-target as large as allowable in our system (5.5 in).

SiO_2 deposition

Motivated by its well-understood properties from the silicon technology, and its large band gap (8 eV), $\boldsymbol{SiO_2}$ was an easy pick as additional gate insulator on InSb. Deposition in 100% argon plasma gave a very low success rate. We suspected that the deposited films might be conductive because of oxygen deficiency. If that were the case, switching to reactive sputtering where oxygen is added to the processing gas would help compensate for any large differential sputtering yield between oxygen and silicon in the sputtering target. 10/90 $\boldsymbol{O_2}$/Ar plasma became the standard processing gas. Typically, after pumping the system to the base pressure of $\sim \mathbf{10^{-6}}$ torr, pure Argon is added to the chamber to raise the pressure to $\mathbf{10^{-2}}$ torr. After striking the plasma (power between 15 and 60 W), the pressure is lowered to the Ar partial pressure needed for the deposition and the power increased slowly to the operation power. Oxygen is then added to the chamber so to get the total deposition pressure. Few minutes after the plasma is stable enough (pre-sputtering), the crystal monitor is reset to zero, the mechanical shutter removed, and the deposition proceeds. At the desired thickness on the crystal monitor, the mechanical shutter is moved in front of the sample, and the power turned off. Figures 6.9 and 6.10 indicate how the RF power affects the deposition rate (measured from the crystal monitor thickness) and the self-bias on the substrate. The deposition rate and substrate self-bias increase with increasing RF power. A higher RF power results in more ionization of the processing gas, and the high ion density in the plasma leads to higher sputtering rate of the target material.

The use of reactive sputtering did not boost the success rate of our gating procedure using $\boldsymbol{SiO_2}$ target as most of the gates still leaked. Finding an alternative material to $\boldsymbol{SiO_2}$ became a priority and we set our sights on silicon oxynitride ($\boldsymbol{SiN_xO_y}$).

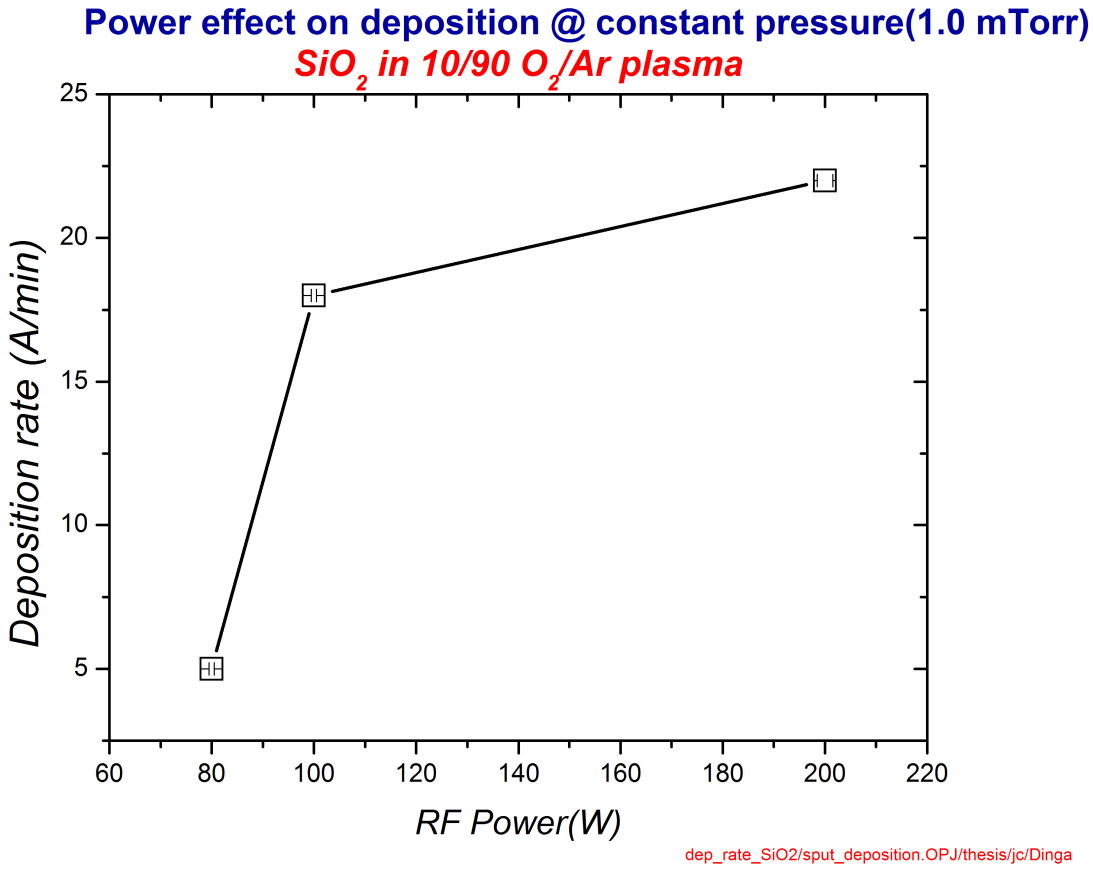

Figure 6.9: RF power effect on deposition rate of $\boldsymbol{SiO_2}$ in 10/90 $\boldsymbol{O_2}$/Ar plasma at 1.0 mtorr. The deposition rate increases with RF power.

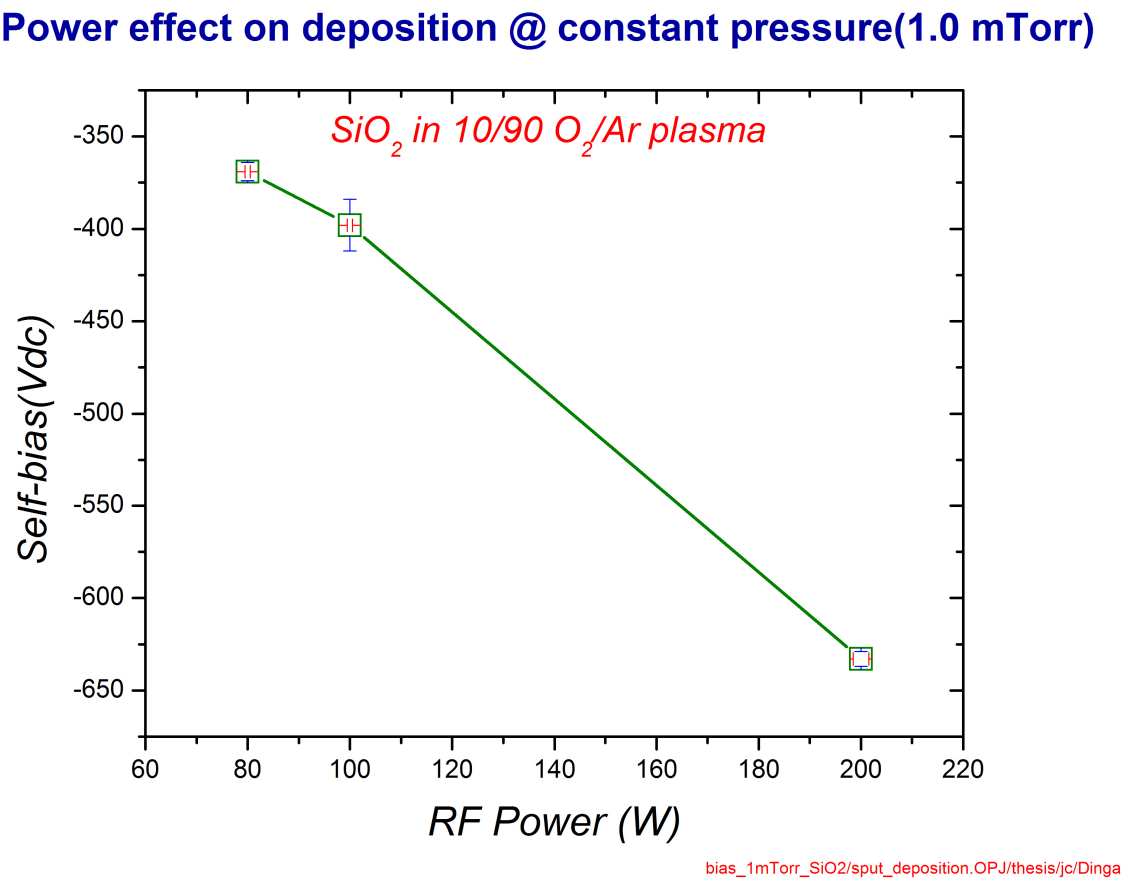

Figure 6.10: RF power effect on substrate self-bias during deposition of $\boldsymbol{SiO_2}$ in 10/90 $\boldsymbol{O_2}$/Ar plasma at 1.0 mtorr. The absolute value of the self-bias voltage increases with increasing RF power.

$\boldsymbol{SiN_xO_y}$ deposition

$\boldsymbol{SiO_2}$ is an excellent barrier to electrons but is a less effective barrier to alkali ion migration. As a result, it might not be the optimal material for low band gap III-V semiconductors for which the group V element is very volatile and could easily diffuse out of the gate insulator unless care is taken to keep the temperature relatively low during deposition. Unlike $\boldsymbol{SiO_2}$, silicon nitride ($\boldsymbol{Si_3N_4}$) is an excellent barrier to alkali ion migration but less effective as electron barrier (Eg $\sim$ 5.1 eV). Furthermore $\boldsymbol{Si_3N_4}$ tends to have a high level of built-in stress that may lead to peeling, breakage

of the film, or damage to the underlying semiconductor. Silicon oxynitride grown in an optimum setting can offer the advantages of both $\boldsymbol{SiO_2}$ and $\boldsymbol{Si_3N_4}$, thus becoming a much effective gate insulator.

The deposition of $\boldsymbol{SiN_xO_y}$ proceeds like that of reactive deposition of $\boldsymbol{SiO_2}$ with the following exception. Oxygen is added to the chamber only after a thin layer (3-5 nm) of $\boldsymbol{Si_3N_4}$ has been deposited. The purpose of this thin layer is to have a nitrogen-rich layer at the interface between the AO and the oxynitride, so to prevent any out-diffusion of any mobile alkali ion from the underlying material to the growing oxynitride. The oxygen content of the plasma is kept low so to form a nitrogen-rich oxynitride.

Figure 6.11 shows the effect of oxygen content in the plasma on the deposition rate at a fixed deposition pressure and power. While the self-bias (see table 6.4) is nearly insensitive to the oxygen content, the deposition rate increases substantially with only about **10%** oxygen in the processing gas. Figure 6.12 shows the effect of deposition pressure on the deposition rate and self-bias when the plasma is maintained at a constant RF power of 200 W. Though we have enough statistics (see table 6.5) only at 2 pressures (1.0 and 3.0 mTorr), there is a clear indication of an increase of deposition rate with decreasing pressure. This observation is consistent with a reduction of the mean free path for sputtered molecules with increasing pressure.

At a fixed RF power, the self-bias is nearly independent of the deposition pressure for pressures larger than 2.0 mTorr. Interestingly enough, large variations in self-bias

%Oxygen	Number of depositions	Dep. rate($\mathring{\boldsymbol{A}}$/min)	Self-bias(V)
0	3	6.7 $\pm$0.3	-318.7 $\pm$15.6
10	1	10	-332
20	1	9.8	-314

Table 6.4: Effect of oxygen content on deposition conditions for $\boldsymbol{SiN_xO_y}$ in an $\boldsymbol{O_2}$ / Ar plasma at a constant total pressure of 1.0 mtorr and RF power of 100 W.

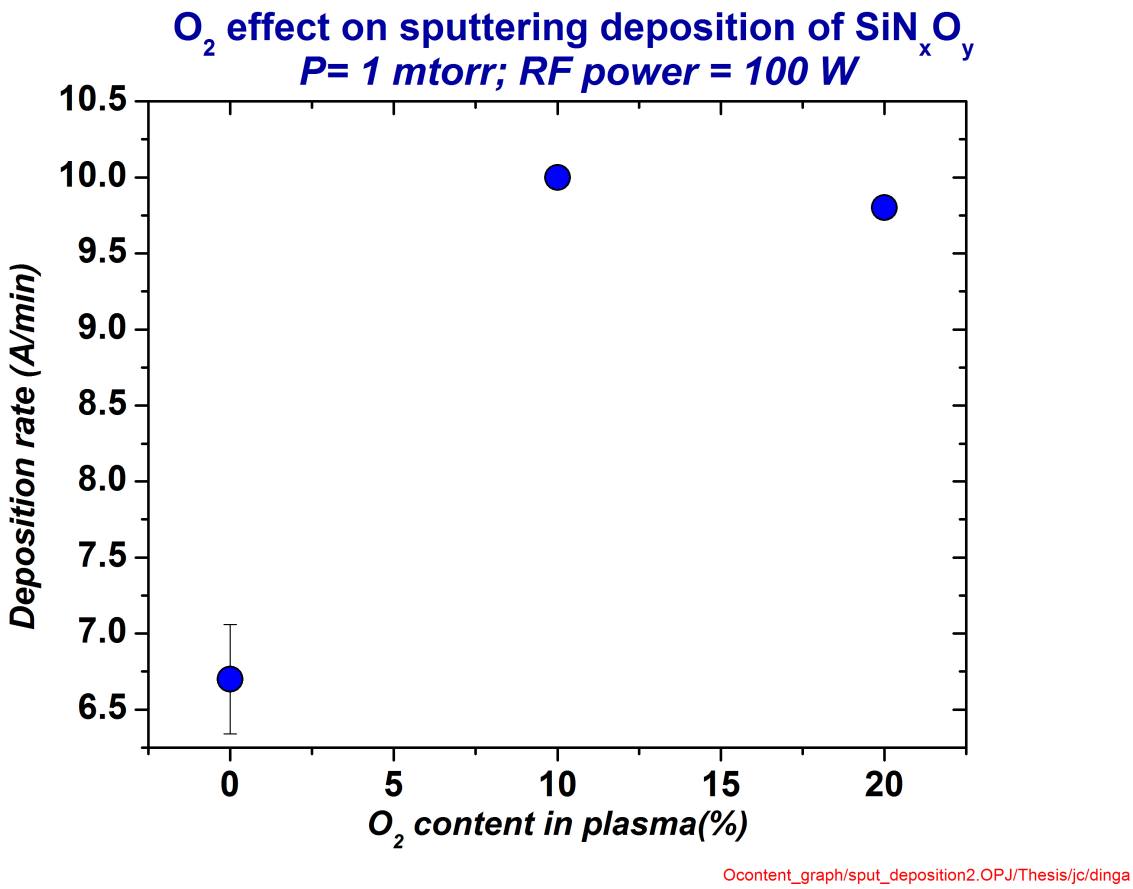

Figure 6.11: Effect of oxygen on deposition rate of $\boldsymbol{SiN_xO_y}$. The total pressure was kept constant at 1.0 mTorr and the RF power at 100 W. Note the rise in deposition rate with addition of only **10%** oxygen in the processing gas.

are observed in the pressure range between 1.0 and 2.0 mTorr, the very same pressure range where hazy films were observed. (See table 6.5)

From here, the deposition conditions were chosen so as to give high quality sputtered films with reasonable deposition rate and high yield. The deposition pressure chosen was 3.0 mtorr in 10/90 $\boldsymbol{O_2}$/Ar with the RF plasma excitation power at 200 W.

P_T(mtorr)	Number of dep.	Dep.rate($\mathring{A}$/min)	Self-bias(V)	Comments
10**	1	3.4	-532	Smooth film,100%
5**	1	10	-520	Smooth film,100%
3*	15	17.2±0.9	-494.9±3.2	Smooth films,100%
2	2	18.3±1.6	-422±10.5	Hazy films
1.5	1	25	-496	Hazy film,75%
1	45	27.0±0.9	-424.5±10.5	Hazy films
0.8	1	25	-498±0.25	Smooth film,25%

Table 6.5: Effect of total pressure ($\boldsymbol{P_T}$) on deposition conditions and film quality for $\boldsymbol{SiN_xO_y}$ in a 10/90 $\boldsymbol{O_2}$ / Ar plasma at a constant power of 200 W. ** indicates that the pressure was very difficult to control and * means pressure needed to be adjusted occasionally.The yield when known, is given in the comments.

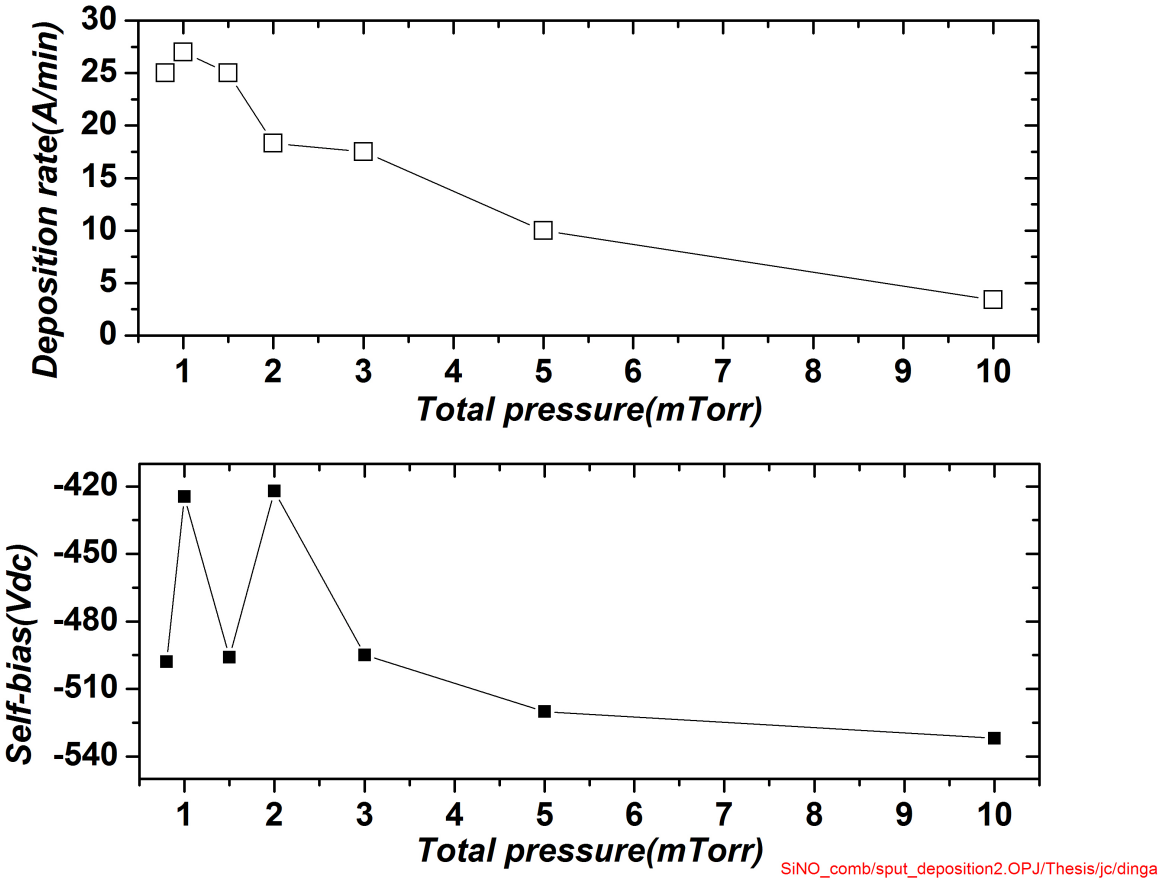

Figure 6.12: Effect of total pressure on deposition rate and self bias for SiN_xO_y in a 10/90 O_2 / Ar plasma at a constant power of 200 W.

6.4 Metal evaporation

6.4.1 Introduction

Since the early days of semiconductor technologies, metal layers were deposited by evaporation. Despite its poor step coverage, metal evaporation is attractive in metal-insulator-semiconductor (MIS) technology because of the relatively small deposition induced damage on the underlying material, the ease to form stacks of different materials with multiple source systems, and the possibility to pattern wafers without etching, using liftoff.

The evaporation consists in heating the material to be deposited past its melting point until it gives off vapor made of atoms. In a high vacuum, those atoms travel nearly in straight lines across the chamber and land on the surface of the sample. For typical thermal evaporation, the material to be evaporated is loaded in a crucible made out of a refractory material. The crucible is heated by running current through it. As the temperature is raised, the material in the crucible goes through solid, liquid, and gas phases. Once molten, the high vapor pressure of the source material ensures a high deposition rate. The deposition rate $\boldsymbol{R_d}$ obeys the cosine distribution law, which reinforces the idea that on the deposited area, the deposition rate decreases as the surface is tilted from the orientation facing the source. The deposition rate is given by:

$$\boldsymbol{R_d = \frac{R_{evap}}{\pi \rho r^2} cos(\theta_k) cos(\theta_i)} \tag{6.14}$$

Where $\boldsymbol{R_{evap}}$ is the evaporation rate of the source material in g/sec, $\boldsymbol{\rho}$ is its mass density in g/$\boldsymbol{cm^3}$, r is the distance in cm from the source to the deposited area,$\boldsymbol{\theta_k}$ is the angle between the incident flux and the normal to the deposition area, and $\boldsymbol{\theta_i}$ the orientation of the surface of the source material to the area being deposited (see figure 6.13).

From Langmuir-Knudsen theory, the evaporation rate of the source material is

given by:

$$\boldsymbol{R_{evap} = 5.83x10^{-2}\sqrt{\frac{M}{T}}P_eA_s} \tag{6.15}$$

Where $\boldsymbol{A_s}$ is the area of the source in $\boldsymbol{cm^2}$, $\boldsymbol{P_e}$ the equilibrium vapor pressure in torr of the source material at the deposition temperature, M the molecular mass of the material in g, and T the deposition temperature in K. Using equations (6.14) and (6.15), the deposition rate in cm/sec is simply

$$\boldsymbol{R_d = 5.83x10^{-2}\sqrt{\frac{M}{\rho^2}}\frac{P_e}{\sqrt{T}}\frac{A_s}{\pi r^2}cos(\theta_k)cos(\theta_i)} \tag{6.16}$$

The expression is written in a way to emphasize the dependence of the deposition rate on the source material, the deposition temperature and the geometry of the deposition chamber.

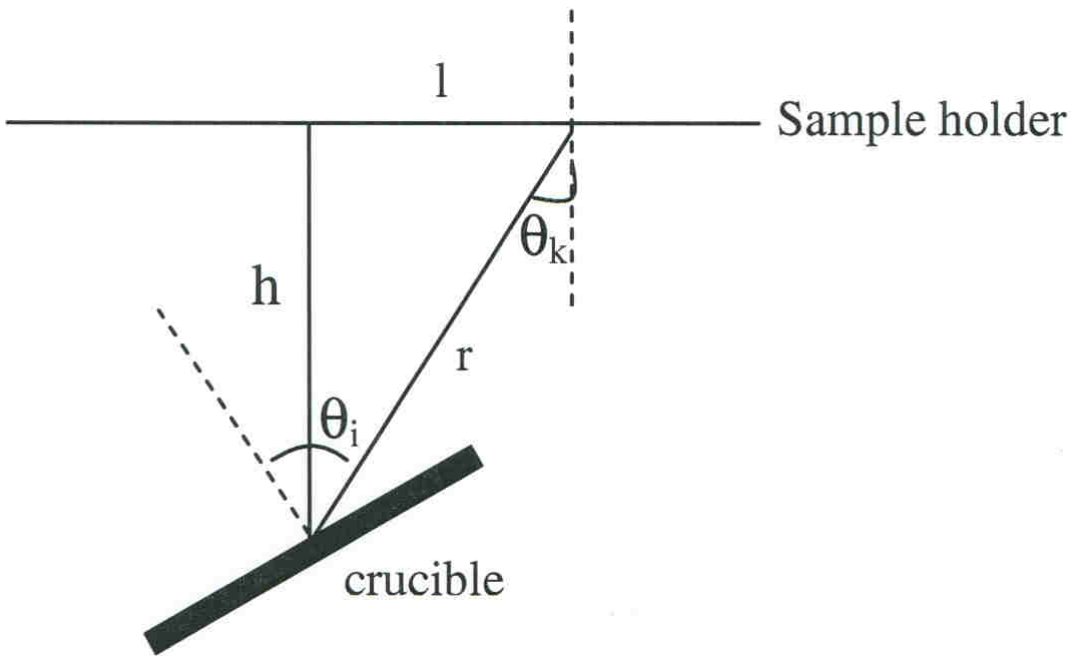

Figure 6.13: Schematic of the deposition geometry during evaporation.

For good uniformity it is recommended to have the sample facing the source straight down and to operate at a moderate deposition rate. Large deposition rates

are obtained by operating at high current or high crucible temperature. Under these conditions, the evaporation material may condense into droplets, which upon adhesion on the wafer can cause substantial damage or lead to very poor surface morphology. At very low deposition rate, residual elements in the deposition chamber may become incorporated in a substantial amount in the deposited film.

6.4.2 System used

The thermal evaporator used is an Edwards vacuum coating unit, model E306A, capable of sequential evaporation from two sources without breaking the vacuum. This is accomplished by switching the current from one crucible to the other using a mechanical switch box. Just as for sputtering, the thickness of the deposited film is measured with a quartz crystal monitor. Because of the integration time of the crystal monitor, it is nearly impossible to use the system for deposition of very thin multicomponent films with good thickness control. For our work, this is not a concern, as our process does not require stringent control of the thickness of various layers. Of concern though is a possible contamination of the films during the slow deposition or more likely during the switch between sources. To minimize contamination during the switch from chromium to gold, one must make sure that the time between the stop of chromium evaporation and the start of gold deposition is as short as possible. To achieve the high vacuum needed for contamination free evaporation, the system is evacuated to at least $\mathbf{10^{-5}}$ torr with a diffusion pump after being pumped out with a mechanical pump to about $\mathbf{10^{-2}}$ torr.

6.4.3 Details of the evaporation

Aluminum evaporation

Aluminum sources are typically high purity aluminum foils folded and loaded in a 5-coil tungsten basket (Part number B12B-.040W from R.D. Mathis Company). The

material is out-gassed at low current for few minutes (5-10 minutes). To avoid balling up of the material in the basket, the current must be increased slowly till the source is molten. The deposition starts once the mechanical shutter is removed and stops when either the shutter is brought in front of the sample or the current is turned off. The basket once coated with aluminum tends to break easily, so it should not be reused more than twice.

Chromium / gold deposition

A chromium plated tungsten rod (Part number CRW-1 from R.D. Mathis Company) is loaded at one crucible location while the other has 99.9% pure gold (Au) blobs in a thin tungsten boat (Part number ME5-.005W from R.D. Mathis Company). To minimize the delay time during the switch to Au, the gold is prepared first. With the mechanical shutter still in front of the sample and the current directed at the Au containing crucible, gold is made molten and allowed to cool. Then the current is switched to the chromium rod. Cr is out-gassed and desorbed of the greenish native oxide that easily grows on it, using a low current just high enough to cause it to glow red ($\sim$ 40-50 Amps) for about 10 minutes. Cr evaporation then proceeds after raising the current to about 70 Amps and removing the shutter. At about 10-20 nm on the crystal monitor, the current is rapidly brought to zero, the current switched to the gold containing boat and increased to about 70 Amps. The input parameters are then changed from Cr to Au and the crystal monitor reading reset. During these operations, some Au is being deposited and should be added to the final thickness read on the crystal monitor. There is no way of knowing precisely how much Au is being deposited. Fortunately, this is of no importance for our process. Typically, we deposit as much Au as available in the boat. For a good coverage of the metal gate area defined either by photolithography or by shadow mask, we found that a minimum of 120 nm of Au, read on the crystal monitor, is necessary.

With every step in the gating process (anodization, sputtering, and evaporation)

being understood, full MIS devices can be fabricated and tested. By tuning various parameters at different steps, we sought the optimal procedure that provided high yield and high quality devices as characterized by capacitance voltage measurements.

6.5 Full gating procedure and test structures

The gating scheme once designed was first tested on calibration samples: bulk InSb (3-5 μm) grown on GaAs (001) semi insulating substrate, in order to save good quantum wells for our transport experiments. The semi insulating nature of the substrate forced us to use a front contact scheme to avoid the need for huge voltage biases.

The procedure that consistently gave gated structures with good yield is described in appendix 3. Note that the procedure can be altered to include some annealing steps as suggested earlier or some liftoff depending on the complexity of the device structure.

Test samples (see figures 6.14 and 6.15) are metal-insulator-semiconductor (MIS) on calibration samples with circular metal gates (Al or Cr/Au) of about 0.8 mm diameter, deposited via shadow masks to define test capacitors.

To characterize the gate insulators, we performed capacitance-voltage (CV) measurements using an HP 4284A LCR-meter and a home built sample holder which allowed us to have the sample in thermal contact either with liquid nitrogen (77 K) or liquid helium (4.2 K) during measurement. The extremely small energy gap of InSb (0.17 eV at 300 K) and its large intrinsic carrier concentration ($\sim \mathbf{10^{16}}\ \boldsymbol{cm^{-3}}$) prevent meaningful CV measurement at room temperature.

For most of the data, the AC probe voltage was 5 mV and the frequency ranged from 20 Hz to 1 MHz. High frequency data ($\geq$ 100 kHz) were subsequently used for density profiling the semiconductor. Under the depletion approximation, it is shown

that the depletion width (depth in the semiconductor) is given by:

$$\boldsymbol{w = \epsilon_{InSb}\epsilon_0 A(\frac{1}{C} - \frac{1}{C_{ins}})} \tag{6.17}$$

Where A is the gate area, C the measured capacitance, $\boldsymbol{C_{ins}}$ the insulator capacitance *i.e.*, the capacitance at accumulation.

The carrier concentration at a given depth is:

$$\boldsymbol{n_s(w) = \frac{-2}{q\epsilon_{InSb}\epsilon_0 A^2 \frac{d(\frac{1}{C^2})}{dV}}} \tag{6.18}$$

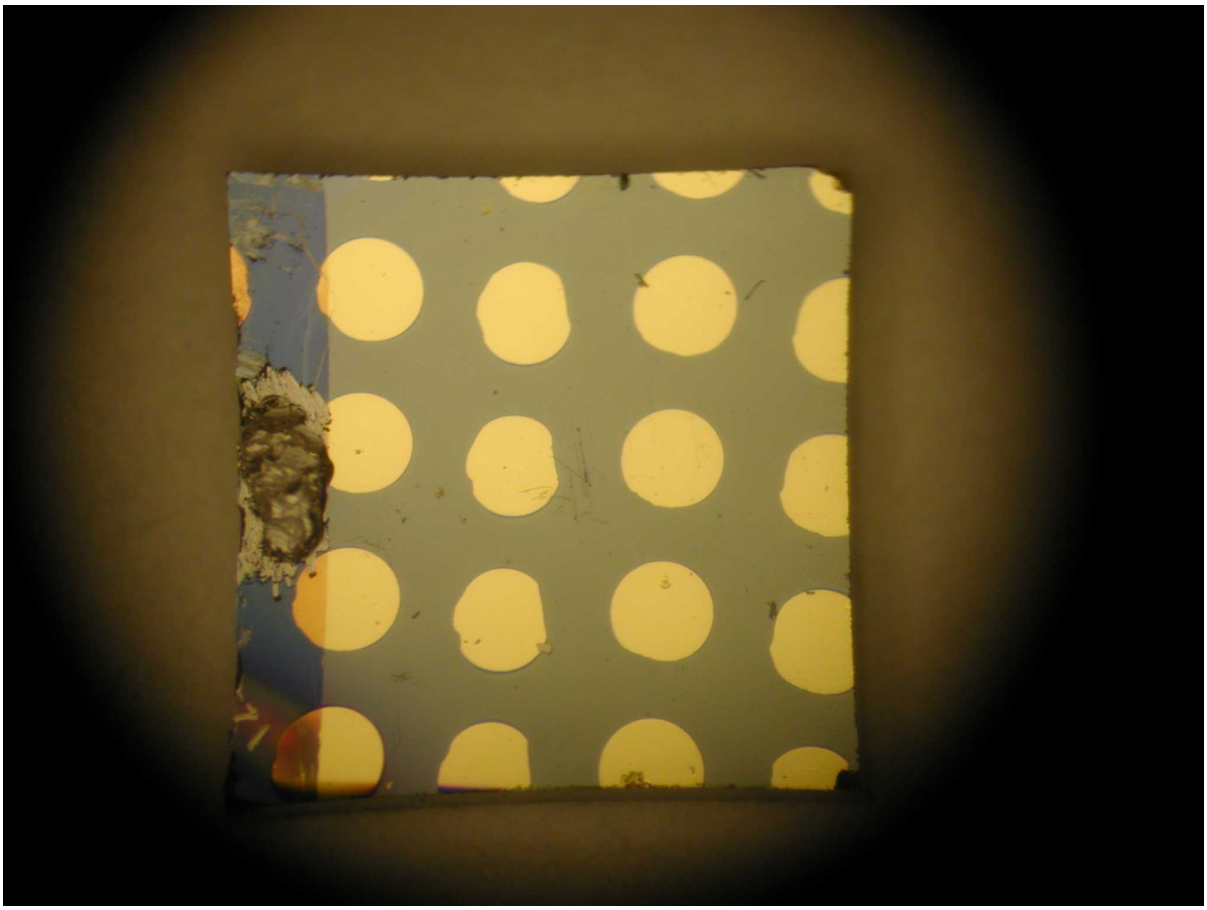

Figure 6.14: Top view optical microscope image of a typical test sample. The dots are Cr/Au metal gates evaporated through a shadow mask, and the lump on the left, is an indium contact to the semiconductor.

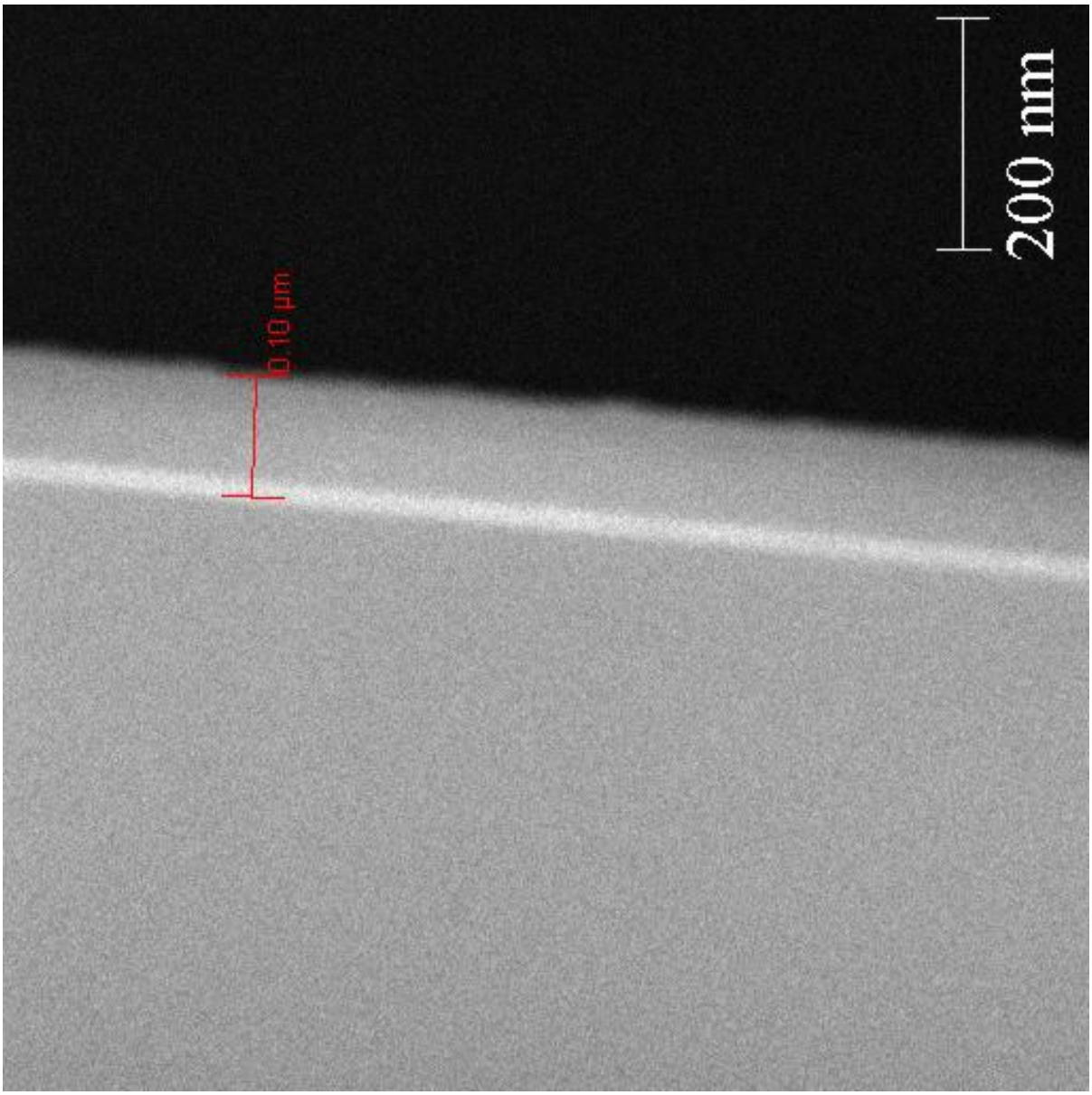

Figure 6.15: Cross sectional scanning electron microscopy image of a typical test sample showing the interface regions between InSb and AO, and AO and $\boldsymbol{SiN_xO_y}$.

6.6 Optimization and CV results

Our goal at this step is to find the optimal procedure and the right parameter to use at each step in order to improve the quality and the yield of the gated structure. We anticipated that most of the problems are related to the interface between the semiconductor and the anodic oxide and focused mostly on this.

6.6.1 Effect of the pH of the electrolyte

The nature of the chemical process during anodization as described earlier, indicates that the kinetics of the reaction can be affected by the pH of the electrolyte. Since large interface states in anodic oxides were traced back to elemental Sb at the interface [64], any modification introduced in the chemical process that would reduce their formation could lead to better oxide. The use of electrolytes with higher pH should cause the reversible reaction leading to oxide formation to be preferentially oriented toward oxide formation thus reducing elemental Sb. As shown on figure 6.16, the sample with the highest pH (pH=9) has the steepest CV curve at depletion with well-developed accumulation and inversion within the voltage range considered. The sample with the lowest pH (5.5) has the most stretched curve indicating a larger density of interface states.

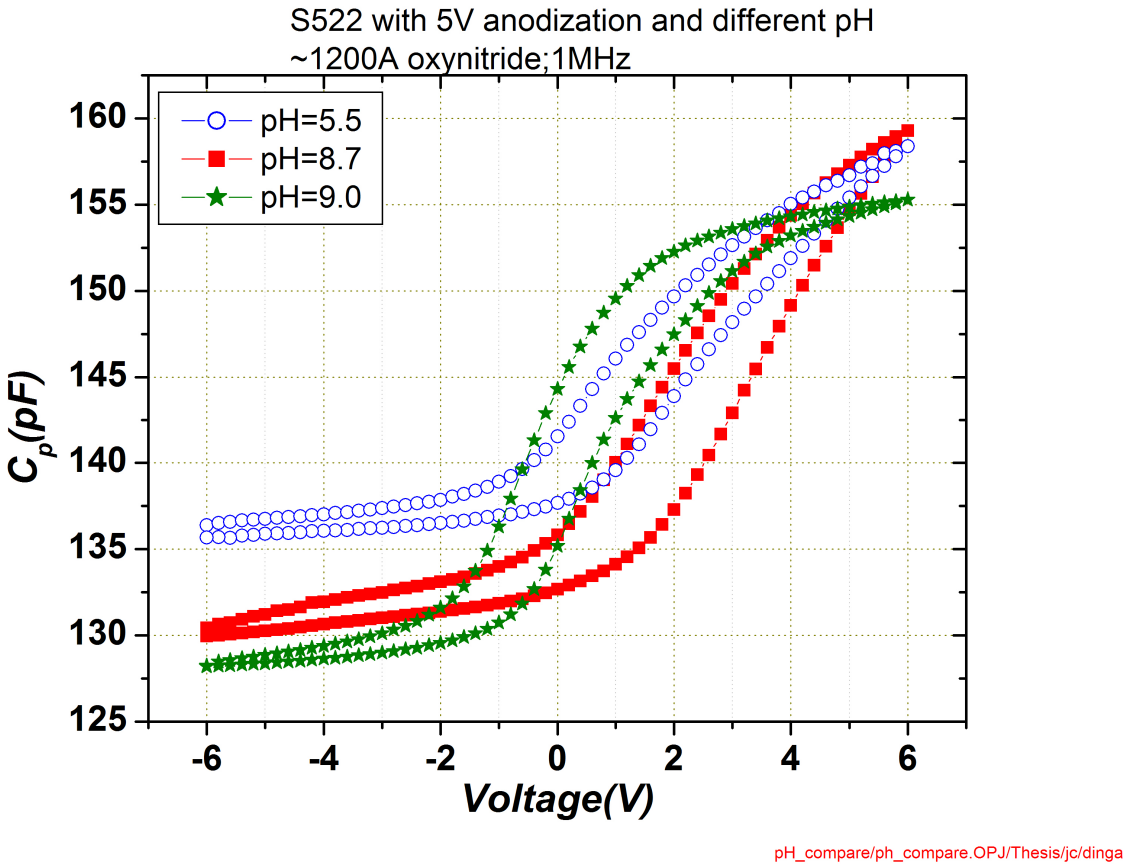

Figure 6.16: High frequency (1 MHz) capacitance-voltage graphs for 3 samples from same wafer processed under similar conditions (5V anodization for 1 minutes, and $\sim$ 120 nm $\boldsymbol{SiN_xO_y}$) except their electrolytes (AGW) have different pH values. Data taken at 77 K.

6.6.2 Anodic voltage effect

From the understanding of the anodization and the sputtering deposition processes described earlier, it is apparent that there might be an AO thickness threshold above which very small damage induced by the sputtering deposition, occurs at the semiconductor/AO interface. Substantial damage at that interface may result in the creation of unwanted interface states that ultimately cause the screening of the semiconductor. The correlation between the AO thickness and the anodization voltage results in a

threshold voltage for anodization for the gating purpose. Successful depletion of the semiconductor will occur only when the sample is anodized at that voltage or higher. Our study confirmed this idea. With anodization voltages below 4.0 V, the yield was poor and the gate would not allow the depletion of the semiconductor. Good gating effect was observed only when the sample was anodized at 4.0 V or higher (see table 6.6).

Anod.Voltage(V)	Sample	Yield on test structure	Good gating properties
0	S522-S5	2/9	No
3	S522-S7	7/8	No
4	S523-a	3/6	Yes
5	S522-S9	12/12	Yes
7	S522-S3	10/10	Yes

Table 6.6: Summary of anodization voltage effect on gate insulator performance. All the samples were processed under similar conditions (same electrolyte (AGW); same anodization time (1 minute), and same oxynitride thickness ($\sim$1150 $\mathring{\boldsymbol{A}}$).

An anodization voltage of at least 4.0 V is necessary to properly gate InSb. In picking a voltage value, one should bear in mind that very thick AOs tend to be porous, and be aware of the possibility of the oxidizing front getting into the quantum well if the well is very shallow.

6.6.3 Annealing effect

Incorporation of water molecules in anodic oxides tends to be the rule rather than the exception. Their presence is suspected to be responsible for the low dielectric strength of anodic oxides and their electrical instability. Annealing anodic oxides at appropriate temperatures to remove incorporated water (densification) is routinely used to improve the reliability of anodic oxides [55]. Proper annealing of sputtered deposited

films helps relieve built-in stress in those films hence enhance their properties [55]. Figure 6.17 shows CV data of samples processed under similar conditions except for an additional annealing step. The post-metalization anneal and post-sputtering anneal seem not to affect much the quality of the gate insulator. This was expected since with the AO buried under the silicon oxy-nitride, the anneal is less likely to eliminate water molecules trapped in the anodic oxide. The dips at 4 V and 8 V are reproducible features observed exclusively at liquid helium temperature on calibration samples. They are more likely related to the locations of specific defect-levels in these samples. A full understanding of their origin requires further investigation, but this was not critical to our work. The CV data on figure 6.17 indicate on the other hand, a substantial shift of the flatband voltage towards more negative gate voltages and an increase in the hysteresis loop when the sample is annealed in the forming gas, right after anodization. The shift is an indication of incorporation of positive charges either in the oxide or at the interface with the semiconductor after the thermal treatment. These charges then act as traps thus the increase in the hysteresis loop. The density profiles of these samples (see figure 6.18) clearly indicate a bump, indicative of charge accumulation, close to the semiconductor surface for the sample annealed right after anodization. It is possible that the deterioration of the gate after post-anodization anneal is due to our annealing in a reducing atmosphere. It would be interesting to determine if an anneal in an oxidizing atmosphere or in vacuum would improve the gate oxide.

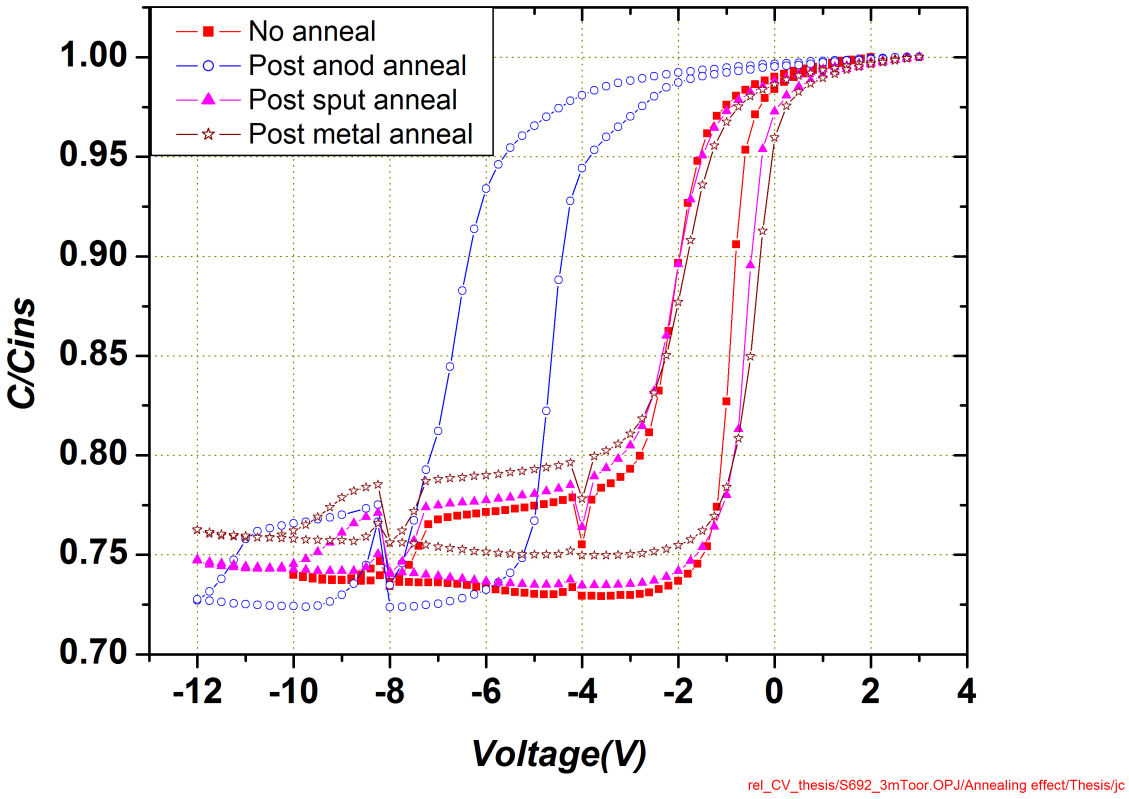

Figure 6.17: High frequency (100 kHz) CV data of samples from same wafer (S692) processed under similar conditions except for an additional annealing step inserted at different stage during processing. The samples were annealed in forming gas at **250°**C for 5 minutes. The oxynitride layer ($\sim$800 $\mathring{\boldsymbol{A}}$) was deposited at once on all samples in 10/90 $\boldsymbol{O_2}$/Ar plasma at a total pressure of 3.0 mtorr and an RF power of 200 W. Data taken at 4.2 K.

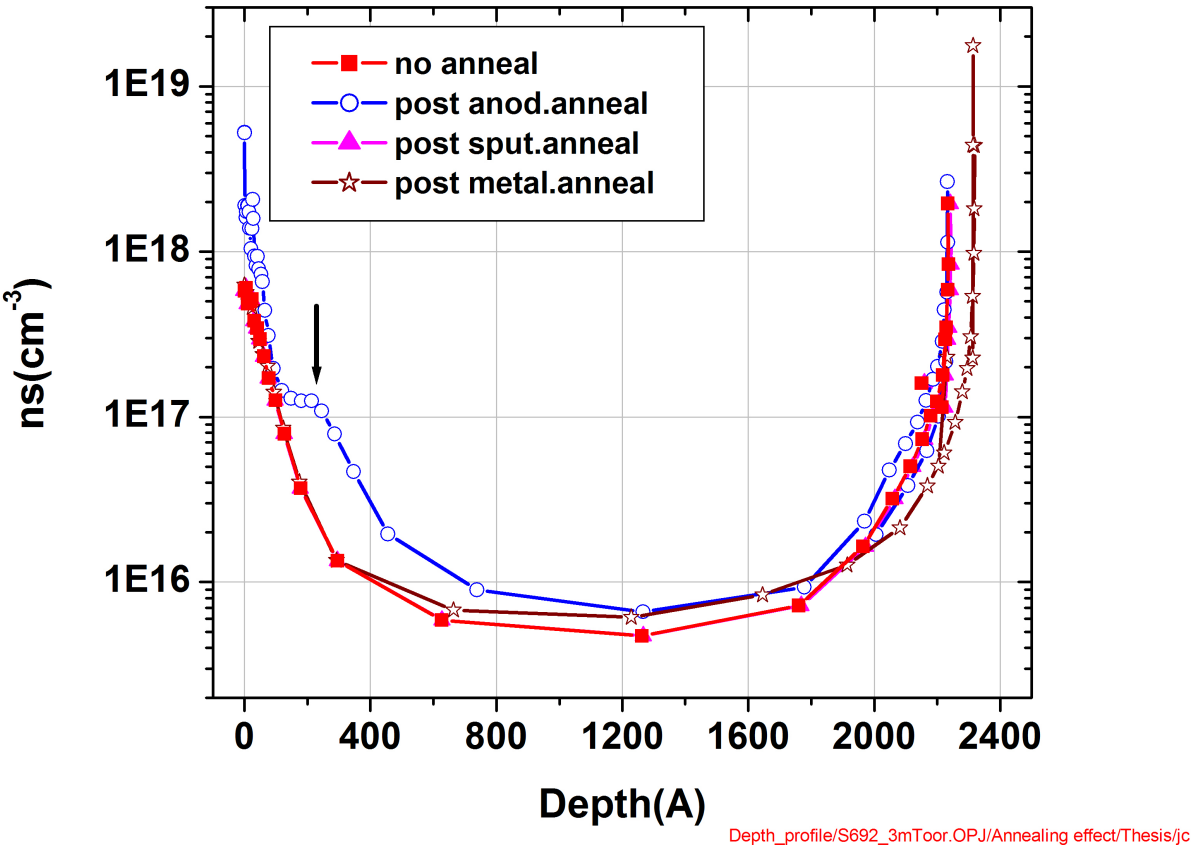

Figure 6.18: Density profile from the down sweep trace of data shown in figure 6.17. The arrow indicates the location of charge accumulation following annealing after anodization.

6.6.4 Fluorine effect

Addition of a few drops of fluoride from 40% NH_4F in high pH electrolyte leads to a faster initial decay of current during anodization (see figure 6.19) without significant increase in the final oxide thickness. From the integrated area under the I-t curves, the fluorinated electrolyte should lead to more than **15%** increase in the AO growth rate. The fact that the AO thicknesses from fluorinated and non-fluorinated electrolytes are not very different despite an obvious faster initial growth from the former, suggests that there might be a stronger oxide etch in fluorinated electrolytes.

Figures 6.20 and 6.21 show for comparison, CV data for samples processed under same conditions except for the anodization step where they were anodized separately in different electrolytes. Structures with fluorinated AO showed a significantly improved gate insulator quality as evidenced by smaller hysteresis loops, steeper CV slopes in depletion and flatband voltages closer to the theoretical value of 0.3 V [65] (See table 6.7). A smaller hysteresis loop indicates a reduction of slow interface states and mobile charges in the oxide and / or semiconductor. A steeper CV slope in depletion corresponds to smaller interface state densities, and a small shift in flatband voltage indicates reduced charges trapped in the oxide. Figure 6.22 shows the effect of Fluorine content in the electrolyte during anodization, on the overall properties of the gate dielectric stack. Fluorine content of less than **3%** is enough for optimum results. Note that at **2.7%** fluorine content, the accumulation capacitance has dropped considerably and the hysteresis loop seems to become larger. Our data suggest that the optimum fluorine content might be between 1 and **2.5%**. The use of halogens to improve gate insulator properties is very common in silicon technology. Addition of small amount of chlorine [66], or fluorine [67] in the process gas during thermal oxide growth leads to faster growth rates [68] and more importantly, oxides with improved dielectric strength [69], radiation hardness [70]; lower interface states densities [71], and reduced oxidation induced stacking faults [72]. It is believed that during oxidation of silicon, the halogens are concentrated at the Si-$\boldsymbol{SiO_2}$ interface where

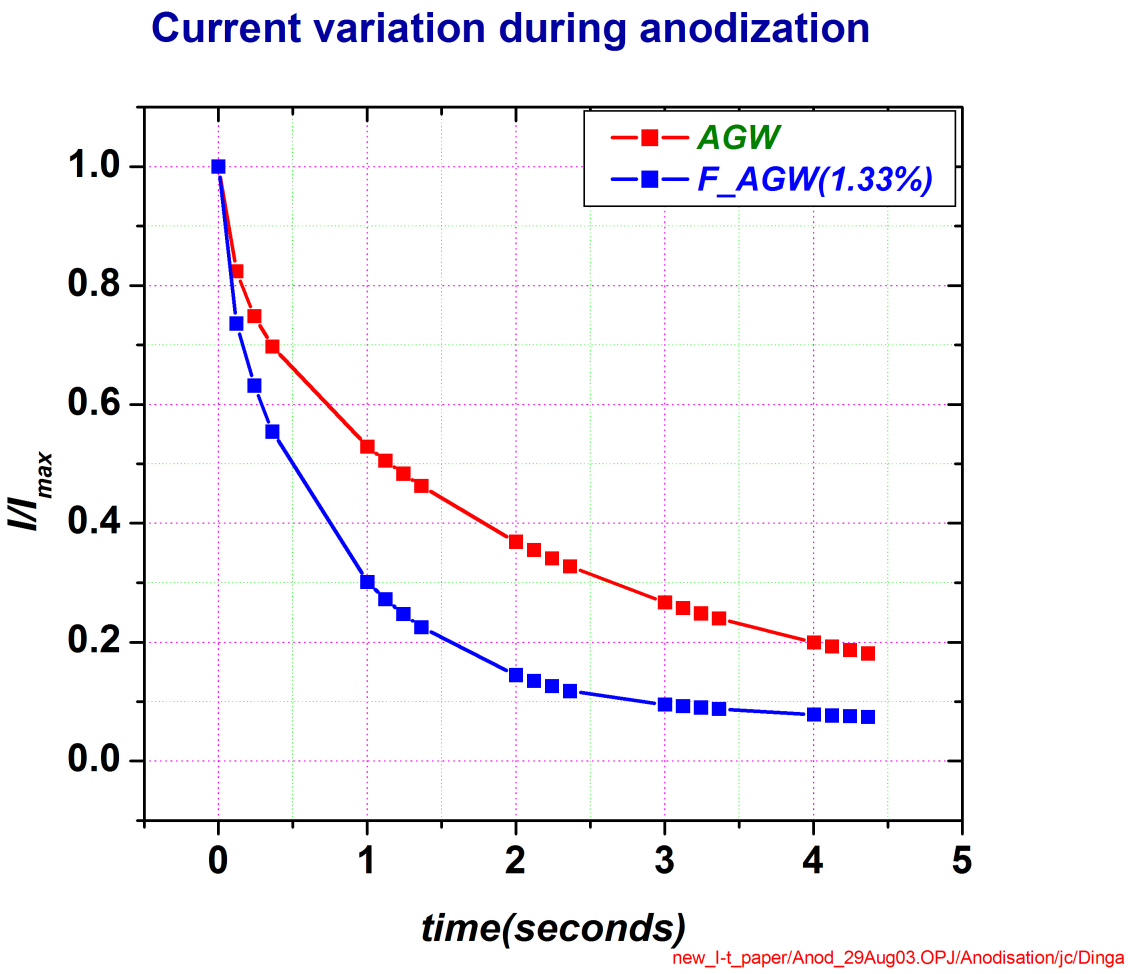

Figure 6.19: Time evolution of anodic current in various electrolytes. For better comparison, the current was normalized to the initial current so to remove any sample specific effect on the current. Note the faster decay of the current when 1.33% fluorine (from 40% NH_4F) is added to the electrolyte. The samples were anodized at 5 V for 5 seconds.

they interact with mobile impurities in the growing oxide and / or in the semiconductor and remove them by converting them into their halogenides [73]. It is likely that similar effect occurs during halogenic anodization. The initial fast growth of the oxide might be coming from the fluoride, lowering the activation energy for oxide nucleation and / or the diffusion of the semiconductor cations in the growing oxide.

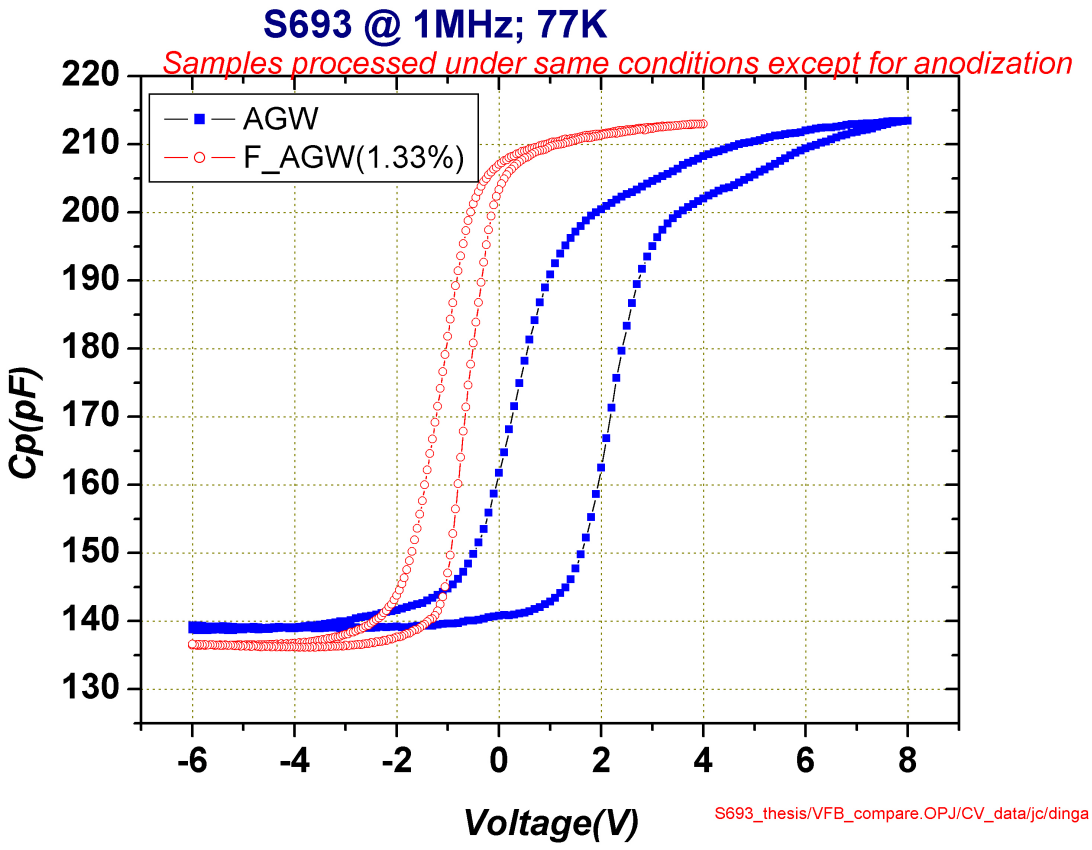

Figure 6.20: High frequency (1 MHz) CV data showing the improvement of the gate insulator by addition of a few percent (1.33% vol) of NH_4F in the electrolyte. The samples are from the same wafer (S693) and were processed under same conditions (5V anodization for 1 minute with a subsequent deposition of about 80 nm of $\boldsymbol{SiN_xO_y}$). Data taken at 77 K.

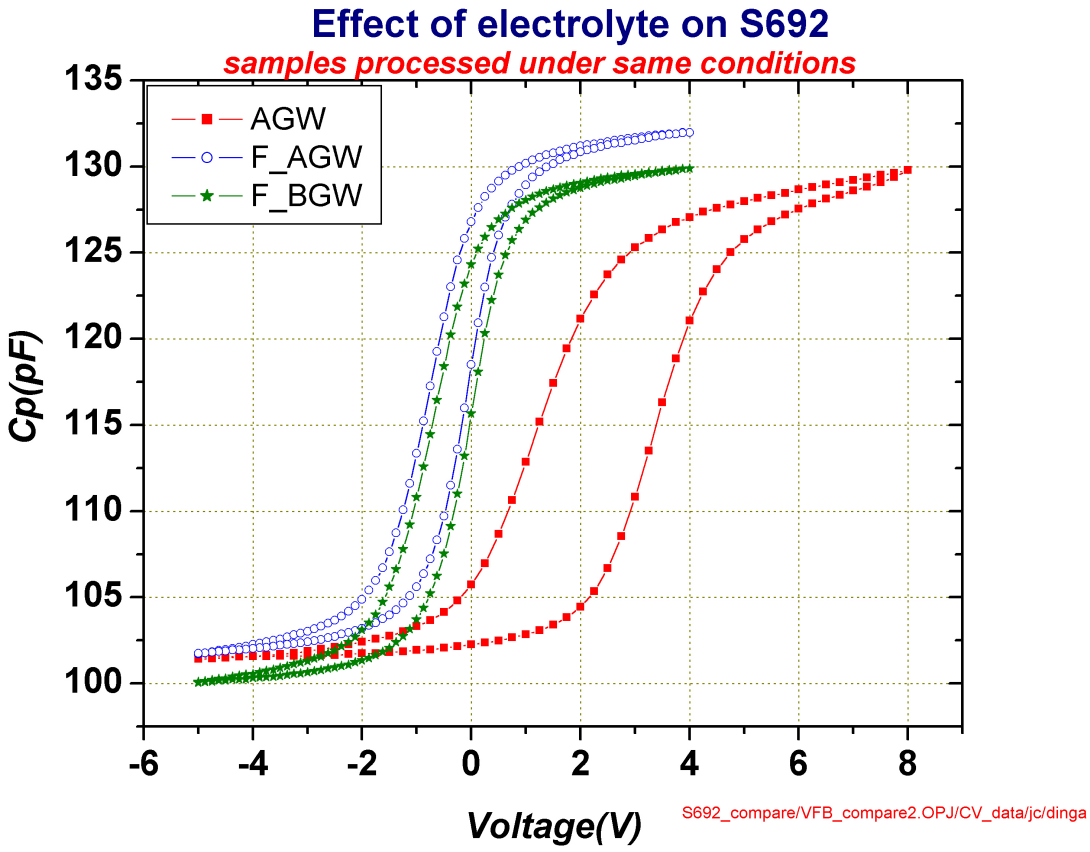

Figure 6.21: High frequency (1 MHz) capacitance-voltage graphs for 3 samples from same wafer processed under same conditions (5V anodization for 1 minutes, and about 85 nm of $\boldsymbol{SiN_xO_y}$) except their electrolytes are different. The fluorinated electrolytes contained 0.33% vol. NH_4F. Data taken at 77 K.

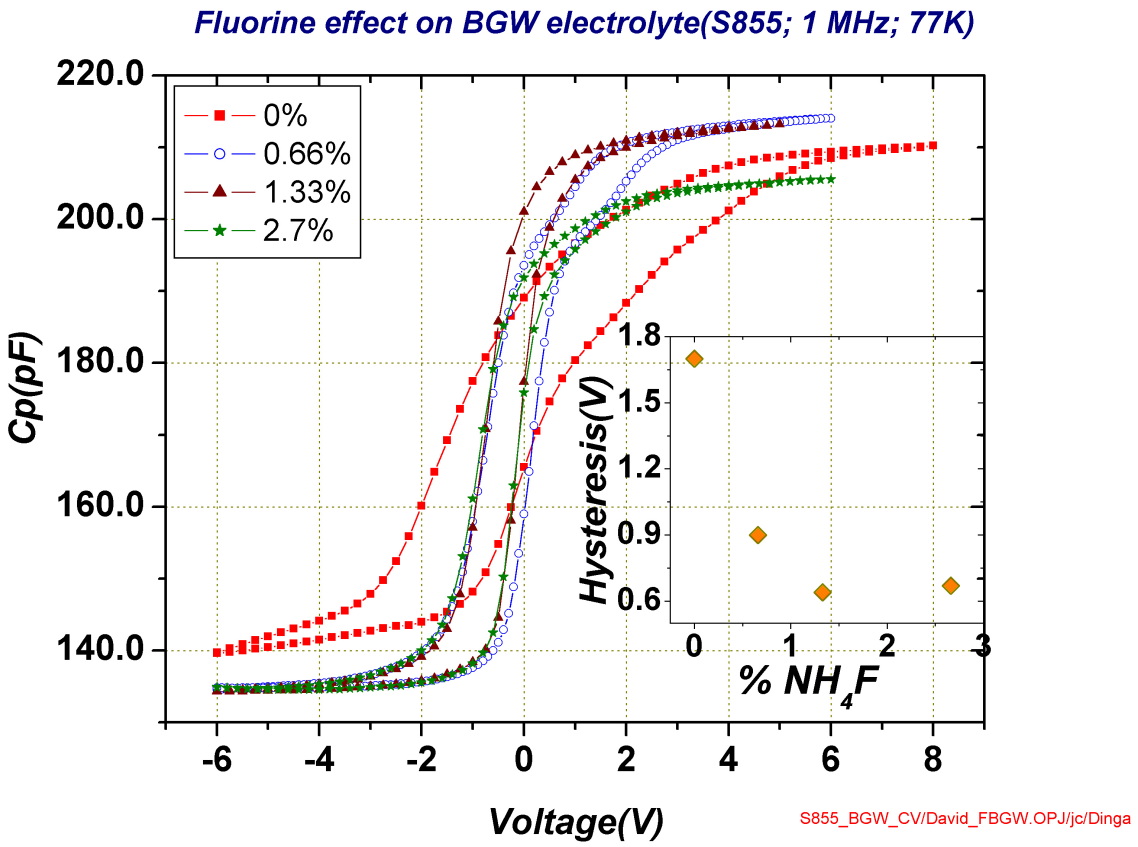

Figure 6.22: High frequency (1 MHz) capacitance-voltage data showing the effect of fluoride addition on the quality of the gate insulator. The samples are from same wafer (S855) and were processed under similar conditions (5V anodization for 1 minutes and about 80 nm of $\boldsymbol{SiN_xOy}$). The inset shows the evolution of the hysteresis loop as a function of volume percentage of $\boldsymbol{NH_4F}$ in the electrolyte. Data taken at 77 K.

Sample	Electrolyte	Hysteresis at V_{FB}	Up sweep V_{FB}
S692	AGW	2.1 V	1.6 V
S693	AGW	1.8 V	0.7 V
S855	BGW	1.7 V	-1.3 V
S692	FAGW(0.66%)	0.6 V	-0.4 V
S693	FAGW(1.33%)	0.5 V	-0.8 V
S692	FBGW(0.66%)	0.6 V	-0.3 V
S855	FBGW(0.66%)	0.9 V	-0.5 V
S855	FBGW(1.33%)	0.6 V	-0.5 V
S855	FBGW(2.66%)	0.7 V	-0.6 V

Table 6.7: Summary of the effect of addition of few volume percent of NH_4F in electrolyte on the overall quality of the gate insulator. The hysteresis loops are measured around flat band voltage.

6.7 Conclusion

Fluorinated AOs combined with sputtered deposited SiN_xO_y result in a good quality gate insulator for device applications on InSb. The procedure developed here competes with best CVD deposited insulator on this material and yet there is still room for improvement. We believe that inclusion of a strategically placed annealing step and a better understanding of the fluorine effect on the dielectric stack can yield reliable and hysteresis-free MIS structures. Better still, might be the use of less damaging deposition techniques such as Atomic Layer Deposition (ALD) for the deposition of the oxynitride on the optimized AO.

Chapter 7

Conclusions

The work presented in this thesis showed the steady steps made towards improving the processing technology of InSb and understanding the nature of interactions in InSb quantum wells. The gating process developed has the potential upon further optimizations; to open the way to reliable room temperature gate controlled devices in this extremely high electron mobility material in spite of its low energy bangap. The observation of Ising quantum Hall ferromagnetism at low filling factors in samples with density above a threshold value of 1.3x$\mathbf{10^{11}}$ $\boldsymbol{cm^{-2}}$ regardless of measured Hall mobilities, added to the onset of QHF at smaller tilt angles with increasing densities, point to disorder (either from defects such as dislocations or long range interactions from remote ionized impurities) being the major limiting factor to electron mobility in the samples used. Suggestions have also being made as to how to further improve the gating process and the understanding of our results on quantum Hall ferromagnetism.

Bibliography

[1] N. W. Ashcroft and N. D. Mermin, Solid State Physics, W. B. Saunders Co. (1976), p.683.

[2] D.P. Young et al., Nature **397**, 412 (1999).

[3] M. Venkatesan, C. B. Fitzgerald, and J.M.D. Coey, Nature **430**, 630 (2004).

[4] R. Monnier and B. Delley, Phys. Rev. Lett. **87**, 157204 (2001).

[5] I.S. Elfimov, S. Yunoki, and G.A. Sawatzky, Phys. Rev. Lett. **89**, 216403 (2002).

[6] M.E. Zhitomirsky, T.M. Rice, and V.I. Anisimov, Nature **402**, 251 (1999).

[7] K.v. Klitzing, G. Dorda, and M. Pepper, Phys. Rev. Lett. **45**, 494 (1980)

[8] D.C. Tsui, H.L. Stormer, and A.C. Gossard, Phys. Rev. Lett. **48**, 1559 (1982)

[9] S. Ilani, J. Martin, E. Teitelbaum, J. H. Smet, D. Mahalu, V. Umansky, and A. Yacobi, Nature **427**, 328 (2004) and reference therein.

[10] S. Das Sarma and A. Pinczuk, Perspectives in Quantum Hall Effects, Wiley, New-York, (1997).

[11] E.P. De Poortere, E. Tutuc, S. J. Papadakis, and M. Shayegan, Science **290**, 11546 (2000); K. Muraki, T. Saku, and Y. Hirayama, Phys. Rev. Lett. **87**, 196801 (2001); J. Jaroszynski, T. Anderarczyk, G. Karczewski, J. Wrobel, T. Wojtowicz, E. papis, E. Kaminska, A. Piotrowska, D. Popovic, and T. Dietl, Phys. Rev.

Lett. **89**, 266802 (2002); J. H. Smet, R. A. deutschmann, W. Wegscheider, G. Abstreiter, and K. V. Klitzing, Phys. Rev. Lett. **86**, 2412 (2001); J. Eom, H. Cho, W. Kang, K. L. Campman, A. C. Gossard, M. Bichler, and W. Wegscheider, Science **289**, 2320 (2000).

[12] G. F. Giuliani and J.J. Quinn, Phys. Rev. B **31**, 6228 (1985); S. Yarlagadda, Phys. Rev. B **44**, 13101 (1991); K. Yang, K. Moon, L. Zheng, A.H. MacDonald, S.M. Girvin, D. Yoshioka, and S. C. Zhang, Phys. Rev. Lett. **72**, 732 (1994); T. Jungwirth, S.P. Shukla, L. Smrcka, M. Shayegan, and A.H. MacDonald, Phys. Rev. Lett. **81**, 2328 (1998).

[13] T. Jungwirth and A.H. MacDonald, Phys. Rev. B **63**, 035305 (2001).

[14] J. Eom, H. Cho, W. Kang, K. L. Campman, A. C. Gossard, M. Bichler, and W. Wegscheider, Science **289**, 2320 (2000).

[15] K. Muraki, T. Saku, and Y. Hirayama, Phys. Rev. Lett. **87**, 196801 (2001).

[16] E.P. De Poortere, E. Tutuc, S. J. Papadakis, and M. Shayegan, Science **290**, 11546 (2000).

[17] J.P. Heremans, Mater. Res. Soc. Symp. Proc. **475**, 63 (1997); J. Heremans, D.L. Partin, C.M. Thrush, and L. Green, Semicond. Sci. Technol. **8**, S424 (1993); J. Heremans, J. Phys. D **26**, 1149 (1993).

[18] T. Ashley, A.B. Dean, C.T. Elliot, G.J. Pryce, A.D. Johnson, and H. Willis, Appl. Phys. Lett. **66**, 481 (1995).

[19] E.Burstein, G.S. Picus, and H.A. Gebbie, Phys. Rev. **103**, 825 (1956).

[20] W.E. Spicer, T. Kendelewicz, N. Newman, K.K. Chin, and I. Lindau, Surface Science **168**, 240 (1986).

[21] G.A. Khodaparast, R.C. Meyer, X.H. Zhang, T.D. Kasturiarachi, R.E. Doezema, S.J. Chung, N. Goel, and M.B. Santos, Physica E **20**, 386 (2004); G.A. Khodaparast, R.E. Doezema, S.J. Chung, K.J. Goldammer, and M.B. Santos, Phys. Rev. B **70**, 155322 (2004).

[22] N. Goel, S.J. Chung, M.B. Santos, K. Suzuki, S. Miyashita, and Y. Hirayama, Physica E **20**, 251 (2004).

[23] From Ioffe Institute database at www.ioffe.rssi.ru.

[24] M. Reine, R. L. Aggarwal, and B. Lax, Phys. Rev. B **5**, 3033 (1972).

[25] N. Goel Ph.D thesis, University of Oklahoma, 2004.

[26] S.J. Chung, K.J. Goldammer, S.C. Lindstrom, M.B. Johnson, and M.B. Santos, J. Vac. Sci. Technol. B. **17**, 1151 (1999).

[27] K. Hirakawa, H. Sakaki, and J. Yoshino, Appl. Phys. Lett. **45**, 253 (1984).

[28] T. D. Mishima, J.C. Kaey, N. Goel, M. A. Ball, S.J. Chung, M.B. Johnson, and M.B. Santos, J. Cryst. Growth **251**, 551 (2003) and reference therein.

[29] N.R. Cooper and J.T. Chalker, Phys. Rev. B **48**, 4530 (1993).

[30] W.K. Liu, Xuemei Zhang, Weiluan Ma, J. Winesett, and M.B. Santos, J. Vac. Sci. Technol. B. **14**, 2339 (1996).

[31] Hong Chen, J.J. Heremans, J.A. Peters, N. Goel, S.J. Chung, and M.B. Santos, Appl. Phys. Lett. **84**, 5380 (2004).

[32] G. F. Giuliani and J.J. Quinn, Phys. Rev. B **31**, 6228 (1985).

[33] S. Yarlagadda, Phys. Rev. B **44**, 13101 (1991).

[34] S. Koch, R.J. Haug, K.v. Klitzing, and M. Razeghi, Phys. Rev. B **47**, 4048 (1993).

[35] S. Brosig, K. Ensslin, A.G. Jansen, C. Nguyen, B. Brar, m. Thomas, and H. Kroemer, Phys. Rev. B **61**, 13045 (2000).

[36] J. Jaroszynski, T. Anderarczyk, G. Karczewski, J. Wrobel, T. Wojtowicz, E. papis, E. Kaminska, A. Piotrowska, D. Popovic, and T. Dietl, Phys. Rev. Lett. **89**, 266802 (2002).

[37] K. Muraki, T. Saku, and Y. Hirayama, Phys. Rev. Lett. **87**, 196801 (2001); G.M. Gusev, A.A. Quivy, T.E. Lamas, J.R. Leite, O. Estibals, J.C. Portal, Phys. Rev. B **67**, 155313 (2003).

[38] T. Jungwirth and A.H. MacDonald, Phys. Rev. Lett. **87**, 216801 (2001).

[39] Nguyen van Lien, Sov. Phys. Semicond. **18**, 207 (1984).

[40] G.M. Gusev, A.A. Quivy, T.E. Lamas, J.R. Leite, O. Estibals, J.C. Portal, Phys. Rev. B **67**, 155313 (2003).

[41] N. Kumada, D. Terasawa, M. Morino, K. Tagashira, A. Sawada, Z.F. Ezawa, K. Muraki, Y. Hirayama, and T. Saku, Phys. Rev. B **69**, 155319 (2004); S. Kraus, O. Stern, J.G.S. Lok, W. Dietsche, K. V. Klitzing, M. Bichler, D. Schuh, and W. Wegscheider, Phys. Rev. Lett. **89**, 266801 (2002).

[42] U. Zeitler, H.W. Schumacher, A.G.M. Jansen, and R. J. Haug, Phys. Rev. Lett. **86**, 866 (2001).

[43] W. Pan, R.R. Du, H.L. Stormer, D.C. Tsui, L.N. Pfeiffer, K.W. Baldwin, and K.W. West, Phys. Rev. Lett. **83**, 820 (1999).

[44] M.M. Fogler, A.A. Koulakov, and B.I. Shklovskii Phys. Rev. B **54**, 1853 (1996).

[45] R. Moessner and J.T. Chalker, Phys. Rev. B **54**, 5006 (1996).

[46] S. Brosig, K. Ensslin, A.G. Jansen, C. Nguyen, B. Brar, M. Thomas, and H. Kroemer, Phys. Rev. B **61**, 13045 (2000); S.J. Papadakis, E.P. De Poortere, and M. Shayegan, Phys. Rev. B **59**, R12743 (1999).

[47] W.K. Liu, Xuemei Zhang, Weiluan Ma, J. Winesett, and M.B. Santos, J. Vac. Sci. Technol. B. **14**, 2339 (1996); S.J. Chung, K.J. Goldammer, S.C. Lindstrom, M.B. Johnson, and M.B. Santos, J. Vac. Sci. Technol. B. **17**, 1151 (1999).

[48] J.D. Langan and C.R. Viswanathan, J. Vac. Sci. Technol. **16**, 1474 (1979); M. Okamura and M. Minakata, J. Appl. Phys. **57**, 2060 (1985); Y. Avigal, J. Bregman, and Y. Shapira, J. Appl. Phys. **63**, 430 (1988).

[49] J.D. Langan and C.R. Viswanathan, J. Vac. Sci. Technol. **16**, 1474 (1979).

[50] S.S. Kim, D.J. Stephens, and G. Lucovsky, J. Vac. Sci. Technol. A **8**, 2039 (1990); S. Hasegawa, M. Matuura, and Y. Kurata, Appl. Phys. Lett. **57**, 2211 (1990).

[51] R.P. Vasquez and F. Grunthaner, J.Appl. Phys. **52**, 3509 (1981); Y. Avigal, J. Bregman, and Y. Shapira, J. Appl. Phys. **63**, 430 (1988).

[52] C.C. Chang, B. Schwartz, and S.P. Murarka, J. Electrochem. Soc. **124**, 922 (1977); P.A. Breeze and H.L. Hartnagel, Thin Solid Films **56**, 51 (1979).

[53] H. Hasegawa and H.L. Hartnagel, J. Electrochem. Soc., **123**, 713 (1976); P.A. Breeze and H.L. Hartnagel, Thin Solid Films **56**, 51 (1979).

[54] H. Hasegawa and H.L. Hartnagel, J. Electrochem. Soc., 123, 713 (1976).

[55] S. K. Ghandhi, VLSI Fabrication Principles, Silicon and Gallium Arsenide, 2nd Edition, John Wiley **&** Sons, Inc. New York (1994).

[56] K. Siegbahn, C. Nordling, A. Fahlman, R. Nordberg, K. Hamrin, J. Hedman, G. Johansson, T. Bergmark, S.E. Karlsson, I. Lindgren, and B. Lindgren, Nova Acta Regiae Soc. Sci. Upsaliensis, Ser IV, Vol. **20** (1967).

[57] R.P. Vasquez and F.J. Grunthaner, J. Appl. Phys. **52**, 3509 (1981); Z.H. Lu, M.J. Graham, D.T. Jiang, and K.H. Tan, Appl. Phys. Lett. **63**, 2941 (1993); V.M. Mikushkin, S.E. Sysoev, and Y.S. Gordeev, Physics of Solid State **46**, 1830 (2004).

[58] C.D. Wagner and A. Joshi, J. Elect. Spect. and Rel. Phenomena **47**, 283 (1988).

[59] D. Briggs and M.P. Seah, Practical Surface Analysis by Auger and X-Ray Photoelectron Spectroscopy, John Wiley & Sons (1983).

[60] W.K. Liu, W.T. Yuen, and R.A. Stradling, J. Vac. Sci. Technol. B **13**, 1539 (1995).

[61] P.A. Breeze and H.L. Hartnagel, Thin Solid Films **56**, 51 (1979).

[62] W.R. Grove, Philos. Trans. Faraday Soc., 87 (1852).

[63] B.A. Movchan and A.V. Demchishin, Phys. Met. Metallogr. **28**, 83 (1969).

[64] T. Nakagawa, K. Ohta, and N. Koshizuka, Jpn. J. Appl. Phys. **19**, L339 (1980); Y. Shapira, J. Bregman, and Z. Calahorra, Appl. Phys. Lett. **47**, 495 (1985).

[65] V.S. Fomenko, Handbook of Thermionic Properties, Plenum Press Data Division, New York (1966).

[66] Young-Bae Park and Shi-Woo Rhee, Appl. Phys. Lett. **66**, 3477 (1995).

[67] P.J. Ireland, O. Jamjoum, L.L. Kazmerski, R.K. Ahrenkiel, P.E. Russel, W. Stanchina, and J.F. Wager, J. Vac. Sci. Technol. A **1**, 653 (1983); T.P. Ma, J. Vac. Sci. Technol. A **10**, 705 (1992).

[68] K. Hirabayashi and J. Iwamura, J. Electrochem. Soc. 120, 1595 (1973); T.P. Ma, J. Vac. Sci. Technol. A **10**, 705 (1992).

[69] T.P. Ma, J. Vac. Sci. Technol. A **10**, 705 (1992); Young-Bae Park and Shi-Woo Rhee, Appl. Phys. Lett. **66**, 3477 (1995).

[70] T.P. Ma, J. Vac. Sci. Technol.A **10**, 705 (1992).

[71] C.M. Osburn, J. Electrochem. Soc. **121**, 809 (1974); T.P. Ma, J. Vac. Sci. Technol. A **10**, 705 (1992); Young-Bae Park and Shi-Woo Rhee, Appl. Phys. Lett. **66**, 3477 (1995).

[72] H. Shiraki, Jpn. J. Appl. Phys. **15**, 83 (1976); T.P. Ma, J. Vac. Sci. Technol. A **10**, 705 (1992).

[73] D.R. Young and C.R. Osburn, J. Electrochem. Soc. **120**, 1578 (1973); T.P. Ma, J. Vac. Sci. Technol. A **10**, 705 (1992); Young-Bae Park and Shi-Woo Rhee, Appl. Phys. Lett. **66**, 3477 (1995).

[74] See chapter 1 p.10 in Perspective in Quantum Hall Effects by S. Das Sarma, John Wiley & Sons, New York (1997).

[75] H.P. Wei, D.C. Tsui, M.A. Paalanen, and A.M.M. Pruisken, Phys. Rev. Lett. **61**, 1294 (1988); H.P. Wei, S.Y. Lin, D.C. Tsui, and A.M.M. Pruisken, Phys. Rev. B **45**, 3926 (1992); S. Koch, R.J. Haug, K.von Klitzing, and K. Ploog, Phys. Rev. B **46**, 1596(1992).

[76] T.Ando and Y. Uemura, J.Phys. Soc. Jpn **36**, 959 (1974).

Appendix A

Anodization Procedure

The following steps were commonly used during anodization of InSb:

- Cleave sample leaving an extra 1 mm on one end. This end will be used to clip the sample so that the contact area between the tungsten clip and the sample stays above the electrolyte during anodization.
- Clean sample in organic solvent; acetone/methanol followed by blow-dry with N_2 gas.
- Clean dedicated beakers for InSb anodization and the cathode (Pt foil).
- Prepare electrolyte: use very clean beakers and/or pipettes, and pay attention to the mixing ratio of the components.
- Set the anodization voltage and the stop watch to the desired anodization conditions. Instruments for monitoring I and V should be initially set so to read the rest voltage and the current flowing in the electrochemical cell before bias.
- Mount sample to the home built sample holder and attached it as the anode then insert the cathode in the electrochemical cell.
- Lower the sample into the electrolyte and wait for the system to reach equilibrium.

- After recording the rest voltage and current, set the meters to higher settings so to record I and V during anodization.
- Start anodization by turning on the voltage source and starting the stop-watch.
- At the desired time, turn off the voltage source, remove the sample from the electrolyte and let it drop in DI water where it is kept until ready for $\boldsymbol{SiN_xO_y}$ deposition.

Once anodized, the sample should be transferred to the sputtering chamber as fast as possible to prevent possible surface contamination.

Appendix B

SiN_xO_y Sputtering Deposition Procedure

1. **Get the vacuum chamber ready.**

   - Clean up target assembly (TA). Use scotch brite to brush the top cover of the TA. The best technique to do this is to use clamping scissors to hold the scotch brite and spin the top cover in the lathe. Ultrasonic clean all the parts (top cover, screws, inner cover etc) in organic solvents: acetone then methanol. Blow dry with $\boldsymbol{N_2}$ gas.
   - Mount source + target assembly and sample. Mount sample making sure that it is flat on sample holder and centered above the source. Also make sure that source-sample distance is appropriate (ask if you don't know). Close vacuum chamber by bringing bell jar down. Close shutter and enter target source parameters in the crystal monitor display panel.

2. **Get low vacuum with mechanical pump.** Close vent toggle valve. Close Foreline and open roughing valve. Wait for pressure to drop to $\sim$4.3x$\mathbf{10^{-2}}$ torr.

3. **Get high vacuum with the Turbo molecular pump.** At 4.3x$\mathbf{10^{-2}}$ torr, close roughing valve and open Foreline. Open Turbo gate valve. Turn on ion

gauge (IG1) Wait for pressure to drop to 2.5x$\mathbf{10^{-6}}$ torr.

4. **Strike the plasma.** At 2.5x$\mathbf{10^{-6}}$ torr, turn off ion gauge (IG1). Open Argon toggle and needle valves to bring pressure up to 1.0x$\mathbf{10^{-2}}$ torr. Turn on RF-600 and ATX-600 (follow instructions on sputterer). Adjust (if needed) the Argon pressure to $\sim$1.0x$\mathbf{10^{-2}}$ torr. (The pressure always creeps up after being set initially). Slowly ramp up the power till plasma is on and keep ramping up to 60W. Lower the pressure to 2.7x$\mathbf{10^{-3}}$ torr and wait for the pressure to be stable (takes about 2 minutes).

5. **Get the system to the operating power.** After pressure is stable at 2.7x$\mathbf{10^{-3}}$ torr; 60 W Increase power to 100 W by steps of 10 W with a small pause ($\sim$30 seconds) between steps to let the electronics reach equilibrium. (Typically, wait for "Tuner OK" to be displayed on RF-600 panel. Stop 2 minutes at 2.7x$\mathbf{10^{-3}}$ torr; 100W. Increase the power to 150 W by steps of 10 W as before. Get the system to be stable at 2.7x$\mathbf{10^{-3}}$ torr, 150W (takes about 2 min). Increase power to 200 W by steps of 10 W as before. Get the system to be stable at 2.7x$\mathbf{10^{-3}}$ torr; 200W.

6. **Deposit $\boldsymbol{SiN_xO_y}$ film.** Open the shutter on the crystal monitor and initialize the reading of the film thickness by pressing "shutter" twice. Open the mechanical shutter to start the deposition. At $\sim$ **10**$\mathbf{\mathring{A}}$(on crystal monitor), bleed Oxygen in the plasma to bring the total pressure to 3.0 mTorr. Monitor the deposition by filling the deposition sheet.

7. **Close down the sputterer.** At the desired thickness, stop the sputtering deposition and shut down the system following the procedure posted on the sputterer.

Appendix C

Full Processing Sequence For InSb Quantum Wells

The following procedure was found to give gated structures with good yield:

1. **Cleave sample** to the desired size.

2. **Clean sample** using sequentially TCE (trichloroethylene) / acetone / methanol. Specifically, at this step, the sample is kept in a plastic beaker (to prevent sample breakage) and ultrasonically cleaned for 5 minutes in each solvent. It is finally dried by blowing it with nitrogen gas.

3. **Pattern the sample** to the desired shape (if needed) by photolithography and wet etching.

4. **Form ohmic contacts.** Indium is either evaporated or deposited using a dedicated soldering iron on desired locations on the sample. The metallic material is then driven in the semiconductor by a thermal anneal at $\mathbf{220^oC}$-$\mathbf{250^oC}$ for 5 minutes in forming gas(20% $\boldsymbol{H_2}$; 80% $\boldsymbol{N_2}$).

5. **Anodize the sample.** The contacts can be protected with photoresist. If they are not, their top surface will be oxidized and should be scratched prior to bonding.

6. **Deposit additional insulator** ($\boldsymbol{SiO_2}$ or $\boldsymbol{SiN_xO_y}$) by magnetron sputtering.

7. **Deposit top metal gate** by thermal evaporation.

8. **Mount sample to a header** using rubber cement, colloidal silver paste (from Ted Pella; cat. No. 16032) or silver epoxy (from Epoxy Technology; EPOTEK 417) for more permanent mounting.

9. **Wire sample to the header** using fine Au wire (1 mil, 99.99%) and indium.

Appendix D

Resistance Peak Simulation

The understanding of the quantum Hall effect (QHE) is that when the chemical potential (Fermi level) resides in the localized states away from the Landau level (LL) centers ($\boldsymbol{E_C^N}$), the T= 0K values of $\boldsymbol{\sigma_{xx}}$ and $\boldsymbol{\sigma_{xy}}$ are given by:

$$\boldsymbol{\sigma_{xx} = 0} \tag{D.1}$$

$$\boldsymbol{\sigma_{xy} = \frac{\nu e^2}{h}} \tag{D.2}$$

where $\boldsymbol{\nu}$ is the filling factor. As the Fermi level ($\boldsymbol{E_F}$) passes through the LL center, there is at T=0K an insulator-metal-insulator transition, the system being metallic precisely at the LL center. The values of $\boldsymbol{\sigma_{xx}}$ and $\boldsymbol{\sigma_{xy}}$ are given by:

$$\boldsymbol{\sigma_{xx} = 0 \qquad at E_F \neq E_C^N} \tag{D.3}$$

$$\boldsymbol{\sigma_{xy} = \frac{\nu e^2}{h}, \qquad E_F < E_C^N - \delta} \tag{D.4}$$

$$\boldsymbol{\sigma_{xy} = \frac{(\nu + 1) e^2}{h}, \qquad E_F > E_C^N + \delta} \tag{D.5}$$

$\boldsymbol{\delta}$ is infinitely small. By analogy to other two dimensional quantum phase transitions (e.g. superconductor-insulator), it is conjectured [10] that in the extended state ($\boldsymbol{E_F}$= $\boldsymbol{E_C^N}$) the values of $\boldsymbol{\sigma_{xx}}$ and $\boldsymbol{\sigma_{xy}}$ are universal at T= 0 K.

$$\boldsymbol{\sigma_{xx} = \frac{e^2}{h}} \tag{D.6}$$

$$\boldsymbol{\sigma_{xy} = (\nu + 1/2)\frac{e^2}{h}} \tag{D.7}$$

Using the relation between conductivity and resistivity in 2D, we can write the resistivities at T=0K when $\boldsymbol{E_F = E_C^N}$ as:

$$\boldsymbol{\rho_{xx} = \frac{1/2}{(\nu + 1/2)^2 + (1/2)^2}\frac{h}{e^2}} \tag{D.8}$$

$$\boldsymbol{\rho_{xy} = \frac{\nu + 1/2}{(\nu + 1/2)^2 + (1/2)^2}\frac{h}{e^2}} \tag{D.9}$$

From temperature studies, it has been found [**?**] that at finite temperature T, the longitudinal resistivity peaks at half filling factors, in units of $\frac{h}{e^2}$, vary as:

$$\boldsymbol{\rho_{xx} = \frac{1/2}{(\nu + 1/2)^2 + (1/2)^2}exp(-\beta T)} \tag{D.10}$$

We used gaussians, broadened as much as the gaussian broadened LL to represent the resistivity profile in the vicinity of half filling fractions

$$\boldsymbol{\rho_{xx} = \frac{1/2}{(\nu + 1/2)^2 + (1/2)^2}exp(-\beta T)exp[-1/2(\frac{\nu - \nu_0}{\Gamma})^2]} \tag{D.11}$$

where the broadening is given by [75]:

$$\boldsymbol{\Gamma = \Gamma_0 T^{\kappa}} \tag{D.12}$$

$\boldsymbol{\kappa}$ is the universal temperature exponent taken as $\boldsymbol{\kappa}$=0.4 [10] for spin-split levels. $\boldsymbol{\Gamma_0}$ is defined as [76]:

$$\boldsymbol{\Gamma_0 = \alpha\sqrt{B_{\perp}}} \tag{D.13}$$

where $\boldsymbol{\alpha}$ is a constant (0.045 in our simulation) and $\boldsymbol{B_{\perp}}$ the perpendicular component of the applied magnetic field.

To simulate the metallic behavior of the resistance peak at $\boldsymbol{\nu}$=2 and its $\frac{1}{\sqrt{T}}$ activated behavior, we used the following expression for the resistivity profile:

$$\boldsymbol{\rho_{xx} = \frac{1/2}{(\nu + 1/2)^2 + (1/2)^2}exp(-\sqrt{\frac{T_0}{T}})exp[-1/2(\frac{\nu - \nu_0}{\Gamma})^2]} \tag{D.14}$$

$\boldsymbol{T_0}$ is the characteristic temperature.

Together, the magnetoresistance data with resistance maximum at $\boldsymbol{\nu}$ =1.5, 2, and 2.5 is simulated using the following expression:

$$\boldsymbol{\rho_{xx} = A_1(\nu,T)exp[-1/2(\frac{\nu-1.5}{\Gamma})^2] + A_p(\nu,T)exp[-1/2(\frac{\nu-2}{\Gamma})^2] + A_1(\nu,T)exp[-1/2(\frac{\nu-2.5}{\Gamma})^2]} \quad \text{(D.15)}$$

where

$$\boldsymbol{A_1(\nu,T) = \frac{1/2}{(\nu+1/2)^2+(1/2)^2}exp(-\beta T)} \quad \text{(D.16)}$$

With $\boldsymbol{\beta}$=1/16 in our simulation.

$$\boldsymbol{A_p(\nu,T) = \frac{1/2}{(\nu+1/2)^2+(1/2)^2}exp(-\sqrt{\frac{T_0}{T}})} \quad \text{(D.17)}$$

$\boldsymbol{T_0}$ =1.25 K in our simulation. To get the field dependence, we used the following relations:

$$\boldsymbol{B_\perp = \frac{4.1375 n_s}{\nu}} \quad \text{(D.18)}$$

$\boldsymbol{n_s}$ is the carrier density in units of $\boldsymbol{10^{11}\ cm^{-2}}$.

$$\boldsymbol{B = \frac{B_\perp}{cos(\theta)}} \quad \text{(D.19)}$$

And $\boldsymbol{\theta}$ is the tilt angle.